N°d’ordre NNT : 2017LYSEC50

THESE de DOCTORAT DE L’UNIVERSITE DE LYON
opérée au sein de l’Ecole centrale de Lyon

Ecole Doctorale N° 162
Mécanique, Energétique, Génie civil, Acoustique

Spécialité de doctorat :
Mécanique des fluides

Soutenue publiquement le 23 Novembre 2017, par :
JIANG Lei

Dynamics of Densimetric Plumes and Fire Plumes in Ventilated Tunnels

---

Jury

Richard Perkins	Professeur	Ecole Centrale de Lyon, LMFA	Directeur de thèse
Matheiu Creyssels	MdC	Ecole Centrale de Lyon, LMFA	Co-directeur de thèse
Pietro Salizzoni	MdC HdR	Ecole Centrale de Lyon, LMFA	Co-directeur de thèse
Elisabeth Blanchard	Ing. Dr.	RATP	Examinateur
Vittorio Verda	Professeur	Politecnico di Torino	Rapporteur
Jean-Pierre Garo	Professeur	Institut Pprime Poitiers	Rapporteur

Abstract

This thesis investigates experimentally, theoretically and numerically the critical ventilation velocity in longitudinal ventilated tunnels in case of a fire. The critical velocity is defined as the minimum ventilation velocity that confines the front of the backlayer of harmful buoyant gases downwind of the source of emission.

The fire is first modeled by a release of light gas in ambient air. In the experiments, the light fluid is an air/helium mixture. A simple mathematical model, based on the classical plume study, is formulated to interpret the variations of the critical velocity as a function of the source conditions (momentum and buoyancy fluxes and geometry). A good agreement is observed between the experimental results and the theoretical predictions for both the momentum-driven and buoyancy-driven releases. In addition, the non-Boussinesq effects, i.e. related to large differences between the densities of the buoyant plume and the ambient fluid, could be suitably modeled.

Subsequently, the difference between a buoyant plume and a fire is studied, by combining experiments and numerical simulations. The reason for the appearance of the so-called ‘super-critical’ velocity, a ventilation velocity that becomes independent of the heat release rate when it becomes large, is discussed. It is shown that small fires can be reliably modeled as buoyant densimetric plumes released at ground level. The dynamics induced by larger fires require instead the modeling of large flames and hence a volumetric source of heat and buoyancy within the tunnel. In the simulation of fires, when the heat release rate is increased, the volume of combustion also increases, but the critical velocity remains nearly constant, which validates the appearance of the ‘super-critical’ velocity.

The effect of tunnel inclination on the critical velocity is then studied. The influence of slope (defined as negative when the entrance of fresh air is at a lower elevation than the source) on the movement of smoke is mainly related to the role of the component of buoyancy along the tunnel axis. A positive slope helps the formation of the backlayer, while a negative slope helps reaching the critical condition. However, this effect depends on the source condition. Our experiments and numerical simulations on densimetric plumes suggest that the dynamical condition at the source affects the critical velocity of a buoyant plume: when the buoyant plume is momentum-driven, the influence of slope is small; when the buoyant plume is buoyancy-driven, the influence of slope is large. This behavior can be well described by a theoretical model based on the previous model of the critical velocity in a horizontal tunnel. These results have been extended to the case of fires by conducting numerical simulations and there is again a good agreement between the observed results and the theoretical model. In particular, the ratio of the critical velocities obtained for an inclined and an horizontal tunnel is independent of the power of the fire.

Finally, the effect of vehicular blockage on the critical velocity is studied experimentally and numerically. The vehicles are modeled by blocks of different sizes placed upstream of the buoyancy or fire source. It is shown that only the block close to the source affects the critical velocity, whereas the effect of other blocks of the same size located further upstream is negligible. As the fire-blockage distance becomes larger, the critical velocity changes and becomes close to the value in an empty tunnel. The relative position between the blocks and the fire source has large influence on the critical velocity. When the blocks are placed at the center laterally, the ventilation flow cannot reach the fire plume directly, a larger critical velocity is needed compared with that in a corresponding empty tunnel. On the other hand, when the blocks are placed at the sides laterally, the ventilation flow can directly impact the fire plume and a smaller critical velocity is needed, with a reduction ratio similar to the blockage ratio. It is also found that the changing of critical velocity ratio (ratio between the case with blocks and that in an empty tunnel) is mainly affected by the blocks, whereas the effect of the source condition (buoyant plume, small or large fire) is small.

Keywords: Critical velocity, Buoyant plume, Fire, Tunnel, Inclination, Block

Abstract in French

Cette thèse a pour objectif la caractérisation de la vitesse de ventilation critique dans un tunnel ventilé longitudinalement lorsque survient un incendie. La vitesse critique est définie comme la vitesse de ventilation minimale pour laquelle l'ensemble des fumées nocives est repoussé à l'aval de l'incendie. Les méthodes utilisées sont théoriques, expérimentales et numériques.

Dans une première approche, l'incendie est modélisé par un rejet de fluide plus léger que l'air ambiant. Dans les expériences, il s'agit soit de l'air chaud, soit d'un mélange d'air et d'hélium ce qui permet d'étudier les effets dits non-Boussinesq, c'est à dire induits par une large différence de densité entre le rejet flottant et l'air ambiant. Une modélisation théorique simple est également donnée afin d'expliquer les variations de la vitesse de ventilation critique en fonction des conditions à la source du rejet (flux de flottabilité et géométrie). Un bon accord est observé entre les résultats expérimentaux et le modèle théorique aussi bien pour les rejets dits forcés (jets) que pour les rejets dits flottants (panaches).

Des simulations numériques ont été également menées afin de fournir une comparaison quantitative des vitesses critiques obtenues dans le cas d'un incendie modélisé par un panache et le cas d'un feu. L'apparition d'une vitesse dite 'super-critique' observée dans la littérature dans le cas de feux a été étudiée. L'effet sur la vitesse critique d'un feu de puissance faible peut très largement être modélisé par l'effet d'un rejet de fluide léger au sol. En revanche, un feu de forte puissance nécessite une modélisation des flammes et donc de puissance thermique produite en volume dans une partie non négligeable du tunnel. La présence de flammes représente donc une source distribuée de flux de flottabilité au dessus et en aval du lieu d'injection des gaz de combustion. En conséquence, dans cette situation, le foyer ne peut être modélisé par une simple condition aux limites au sol du tunnel.

L'effet sur la vitesse critique d'une éventuelle inclinaison ou pente du tunnel a été également étudié. Une inclinaison du tunnel dans le sens de la ventilation induit une diminution de la vitesse critique par rapport à un tunnel horizontal alors que pour une inclinaison en sens contraire la vitesse critique est augmentée. Cependant, cet effet dépend des conditions à la source du rejet. Pour les rejets flottants, l'effet de la pente du tunnel est important tandis que la vitesse critique devient de moins en moins dépendante de la pente au fur et à mesure que le rejet devient forcé. Le modèle théorique développé pour un rejet dans un tunnel horizontal a été adapté au cas avec pente et un bon accord a de nouveau été établi entre les résultats expérimentaux et le modèle théorique. Enfin, pour un feu, les simulations numériques ont montré que la pente influence très peu la vitesse critique.

Dans une dernière partie, l'effet de la présence de véhicules dans le tunnel a été investigué aussi bien expérimentalement qu'avec l'outil numérique. Les véhicules sont modélisés par des blocs parallélépipédiques de différentes tailles placés en amont de la source de flottabilité ou le feu. Il a été montré que seul le bloc proche de la source modifiait la valeur de la vitesse de ventilation critique alors que les blocs plus éloignés avaient une influence négligeable. De même, la vitesse critique obtenue en présence de blocs se rapproche très rapidement de celle obtenue pour un tunnel sans véhicule lorsque la distance entre la source et le bloc le plus proche augmente. Le paramètre qui influence le plus la vitesse critique est la position relative du bloc et de la source. Lorsque le bloc protège directement la source en étant placé à son côté aussi bien longitudinalement que latéralement, l'air frais de la ventilation n'impacte pas directement le rejet et la vitesse critique est augmentée par rapport à la situation sans bloc. En revanche, lorsque le bloc est placé un peu plus loin latéralement tout en étant proche longitudinalement, l'air frais peut impacter directement le rejet et la vitesse critique est alors observée plus faible que celle obtenue sans bloc. La diminution de la vitesse critique est alors semblable en pourcentage à la diminution de section du tunnel induite par la présence du bloc, elle est attribuée au fait que le bloc induit une augmentation de la vitesse locale de ventilation favorisant donc la poussée du panache en aval. Au contraire, quand le bloc protège la source, la vitesse locale de ventilation est nulle au niveau de la source et elle est augmentée plus loin aux endroits où le panache est moins présent, ce qui induit cette fois-ci une augmentation de la vitesse critique.

Keywords: Vitesse critique, Panache flottant, Feux, Tunnel, Inclinaison, Obstacles

Table of contents

List of figures ix

List of tables xi

Nomenclature xiii

1 Introduction 1

1.1 Tunnel fire hazards 1
1.2 Ventilation strategies 2
  1.2.1 Longitudinal ventilation 2
  1.2.2 Transverse ventilation 3
1.3 Investigation methods 4
  1.3.1 Large-scale tests 4
  1.3.2 Small-scale tests 5
  1.3.3 Numerical simulations 6
1.4 Overview of the study 6
  1.4.1 Objectives 6
  1.4.2 Plan of the work 7

2 Methods 9

2.1 Theoretical methods 9
2.2 Experimental methods 10
  2.2.1 Isothermal experiments 11
  2.2.2 Thermal experiments 13
  2.2.3 Tests of the sources 15
2.3 Numerical methods 16

3 The control of light gas releases in ventilated tunnels 21

3.1 Introduction 22

3.2 Theory 22
3.2.1 Analytical solution 27
3.2.2 Asymptotic behaviours 28
3.3 Experiments 30
3.4 Results 32
3.5 Conclusions 37

4 Critical velocity in ventilated tunnels in the case of fire plumes and densimetric plumes 41
4.1 Introduction 42
4.1.1 Background 42
4.1.2 Literature review 44
4.1.3 Open questions 46
4.2 Materials and methods 48
4.2.1 Experiments with buoyant plumes 48
4.2.2 A model for fire plumes 50
4.2.3 Numerical simulations 52
4.3 Results 54
4.3.1 Densimetric plumes: experiments and numerical simulations 54
4.3.2 Comparison between densimetric plumes and fire plumes 56
4.3.3 The role of radiation 58
4.4 Conclusion 61

5 Effect of inclination on critical ventilation velocity 65
5.1 Introduction 66
5.2 Theory 69
5.3 Experimental and numerical methods 71
5.3.1 Experiment 71
5.3.2 Numerical simulations 72
5.4 Results 75
5.4.1 Experimental and analytical results of air/helium releases 75
5.4.2 Numerical results of hot-air plume and propane 76
5.5 Conclusions 78

6 Effect of blockage on critical ventilation velocity in tunnels 79
6.1 Introduction 80
6.2 Experiments 82

6.3 Numerical simulations 85
6.4 Results 86
  6.4.1 Experimental results 86
  6.4.2 Comparison with numerical results 88
6.5 Conclusions 91

7 Conclusions and Perspectives 93

Appendix A Introduction of the numerical simulation 97
A.1 Introduction 97
  A.1.1 Navier-Stokes equations at low-Mach number 97
  A.1.2 Poisson equation on the pressure 100
  A.1.3 Turbulence modeling 101
  A.1.4 Simulation software: Fire Dynamics Simulator 106

References 111

List of figures

1.1 Fire-induced smoke longitudinal control (Vauquelin, 2008). 3

1.2 Fire-induced smoke transverse control (Vauquelin, 2008). 3

2.1 Sketch of the plume, adapted from Michaux and Vauquelin (2008). 10

2.2 Experimental installation at LMFA. 11

2.3 Photos of the sources: isothermal circular source, isothermal planar 2D source and thermal circular source. 11

2.4 Schematic of the experimental set-up for the isothermal model. 12

2.5 Experimental set-up to determine the relationship between the velocity measured by the hot wire anemometer and the flow rate measured by the flow meter 12

2.6 Relationship between the flow rate and the velocity measured by the hot wire anemometer. 13

2.7 Critical ventilation condition in the isothermal experiment (circular source, $\Gamma_i = 0.015$, D_i=25 mm). 13

2.8 Schematic of the experimental set-up for the thermal model. 14

2.9 Temperature at the tunnel ceiling as a function of the distance from the source in the thermal model; the experimental conditions are T_i = 280 °C, w_i =1.17 m/s, V = 0.205 m/s, Γ_i = 1. 14

2.10 Schematic of the sources tests, the three sources shown in Fig. 2.3 are connected to the outlet of the fan, a pitot tube is put at the outlet of the source to measure the velocity profile. 15

2.11 Circular and planar source used in the isothermal experiment, photos are shown in Fig. 2.3. 15

2.12 Velocity profile of the isothermal circular source: (a) $D_i = 100$ mm, (b) $D_i =$ 75 mm, (c) $D_i = 25$ mm, (d) non-dimensional velocity profile at $D_i = 100$, 75, 50, 35, 25 mm. 16

2.13 Velocity profile of the isothermal planar source at the z (width) direction measured at x=0: (a) $L_p = 40$ mm, (b) $L_p = 20$ mm, (c) $L_p = 10$ mm, (d) non-dimensional velocity profile. 17

2.14 Velocity profile of the isothermal planar source at the x (length) direction measured at z=-177, -7, 173 mm: (a) $L_p = 40$ mm, (b) $L_p = 20$ mm, (c) $L_p =$ 10 mm, (d) non-dimensional velocity profile. 18

2.15 Non-dimensional velocity profile of the thermal (w_i=1.6 m/s) and isothermal (w_i=1.2 m/s) circular source at D_i=100 mm. 18

2.16 Longitudinal profiles of the mean and of the standard deviation of the temperature along the tunnel ceiling for the five girds tested (See Table 2.1). . . 20

2.17 A FDS simulation case with propane fire (Q= 0.57 kW, V=0.33 m/s). 20

3.1 Flow visualisations of the buoyant release submitted to a critical ventilation velocity (from right to left): (a) forced release $\Gamma_i < 1$, circular source, (b)lazy release $\Gamma_i > 1$, circular source, (c) forced release, line source, (d) lazy release, line source. 23

3.2 Sketch of the bent-over plume released from a circular source in the ventilated tunnel and of the impingement region (in grey) at the tunnel ceiling. 25

3.3 Schematic of the experimental set-up. 30

3.4 a) $\frac{V_c}{w_i}$ and b) $V_c\left(\frac{W}{B_i}\right)^{\frac{1}{3}}$, as a function of Γ_i for the planar source. 33

3.5 Non-dimensional critical velocity as a function of plume Richardson number Γ_i for a fixed density ratio $\rho_i/\rho_0 = 0.7$. Comparison between experimental data (symbols) obtained for different aspect ratios and analytical solution (Eq. 3.9) (lines). 34

3.6 Non-dimensional critical velocity as a function of plume density ratio ρ_i/ρ_0 for different Γ_i. Comparison between experimental data (symbols) obtained for different aspect ratios and analytical solution Eq. (3.9) (lines). 34

3.7 a) $V_c\left(\frac{H}{B_i}\right)^{\frac{1}{3}}$ and b) $V_c\left(\frac{W}{B_i}\right)^{\frac{1}{3}}$, as a function of Γ_i. Also shown in a) is the critical Froude number $\widehat{\mathrm{Fr}}_c = 0.98$ obtained from (3.19) (dashed horizontal line) and analytical solution (Eq. 3.9) (lines). 37

4.1 Sketch of smoke movements and heat transfers during a fire occurring in a ventilated tunnel. 44

4.2 Overview of literature data on the non-dimensional critical velocity as a function of the non-dimensional heat release rate. 46

4.3 Schematic of the experimental set-up for (a) the 'isothermal model' and (b) the 'thermal model'. 49
4.4 Tunnel geometry of numerical model. 53
4.5 Longitudinal profiles of the mean and of the standard deviation of the temperature along the tunnel ceiling for the five girds tested (See Table 2). . . . 54
4.6 Non-dimensional critical velocity V_c/w_i as a function of the plume Richardson number Γ_i. (a) experimental results comparison between our results (hollow points) and data from Le Clanche et al. (2014) (solid points); (b) comparison between experimental and numerical results. 55
4.7 Non-dimensional critical velocity as a function of Γ_i for ΔT_i equal to (a) 1400 K and (b) 2000 K. 59
4.8 Comparison of critical velocity between numerical simulation and experiment in Wu and Bakar (2000), Γ_i is obtained assumeing a temperature rise $\Delta T_i = 1400$ K (assuming heat losses by radiation equal to 30 % of the HRR). Temperature field and fire of a, b, c, d are shown in Fig. 4.9. 59
4.9 FDS simulations of propane fires. Spatial distribution of temperature and flames ($x-z$ plane at $y = W/2$) for different HRR: 1.0, 3.3, 7.5 and 30 kW. 60
4.10 Influence of radiation on critical velocity, (a) critical velocity at different HRR and (b) radiative fraction. 60
4.11 Longitudinal temperature profiles at the ceiling level of HRR at 1000 W (V=0.35 m/s) and 23000 W (V=0.70 m/s). 62
4.12 Longitudinal velocity profiles at the ceiling level of HRR at 1000 W (V=0.35 m/s) and 23000 W (V=0.70 m/s). 63
4.13 Temperature field of HRR at 1000 W (V=0.35 m/s) and 23000 W (V=0.70 m/s). 63
4.14 Velocity field of HRR at 1000 W (V=0.35 m/s) and 23000 W (V=0.70 m/s). 64

5.1 Critical velocity ratio V_c/V_{c0} as a function of tunnel slope. 67
5.2 Sketch of the plume released in an inclined ventilated tunnel and of its impingement at the tunnel ceiling. 70
5.3 Numerical solution of the ratio $\rho_H {w_H}^2/\rho_{H0} {w_{H0}}^2$ at 5° and 10°. Computations are performed with: $D_i = 0.1$ m, density ratio $\rho_i/\rho_0 = 0.7$. 71
5.4 Schematic of the experimental set-up. 71
5.5 Non-dimensional critical velocity as function of Γ_i, in case of buoyant fluid releases: comparison between the experimental and numerical results . . . 74
5.6 Temperature field of propane at 0.57 kw (V=0.33 m/s) and 15.0 kw (V=0.55 m/s) at -8.7%, 0 and 8.7%. 75

5.7 Dependence of V_c/w_i and of the critical velocity ratio V_c/V_{c0} as a function of the slope, comparison between experimental results and analytical solution of the model Eq. (5.9). 76
5.8 Dependence of the critical Froude number Fr_c and of the critical velocity ratio V_c/V_{c0} as a function of the slope in case of buoyant plumes. Comparison between experimental and numerical results (D_i=0.1 m). 77
5.9 Dependence of the critical Froude number Fr_c and of the critical velocity ratio V_c/V_{c0} as a function of the slope in case of propane fires. Comparison between experimental results on buoyant plumes and numerical results on propane fires (D_i=0.1 m), the solution provided by Eq. (5.10) is also plotted. 77

6.1 Tunnel fire with vehicle blockages upstream in the longitudinal ventilation, adapted from Vauquelin (2008). 80
6.2 Schematic of the experimental set-up. 83
6.3 The block locations in the experiment. Three different sizes of blocks (block1 $\psi = 0.15$, block2 $\psi = 0.19$, and block3 $\psi = 0.43$) were used. In configuration A, one block was placed at the center; in configuration B, one array of blocks were placed at the center; in configuration C, two arrays of blocks were placed at the side. 84
6.4 Effect of the fire-blockage distance for configuration A (one block at the center); comparing experiments with Eq. (6.2) by Tang et al. (2013). 86
6.5 Effect of the fire-blockage distance for one block (configuration A) and an array of blocks (configuration B) placed at the centre upstream the source. . 87
6.6 Effect of the fire-blockage distance for two arrays of blocks placed at the sides upstream the source (configuration C). 87
6.7 Non dimensional critical velocity V_c/V_{c0} as a function of 1-ψ. Data from the experimental results ($L = 0$) and from Rojas Alva et al. (2017). Solid line is from Eq. (6.1) and dot line is from Eq. (6.2) (putting $L = 0$) 88
6.8 Comparison between the experimental results and the numerical simulation of hot-air plume in case of the blocks located at the centre (configuration B) (a) and at the sides (configuration C) (b) of the tunnel. 89
6.9 Temperature and velocity fields of the hot-air plume in configuration B (blocks at the center) and configuration C (blocks at the side) for block1 (ψ=15%) at the condition $L/\overline{H} = 0.4$. The ventilation velocity is 0.26 m/s. . 90
6.10 Vertical velocity profiles of the longitudinal velocity at 0.05 m upstream the source (the same condition as Fig. 6.9). 90

6.11 Comparison between experimental results and numerical simulation of the propane fire (large fire at 7.5 kW and small fire at 0.25 kW) in case of blocks located at the centre (configuration B) (a) and the sides (configuration C) (b) of the tunnel. 91

6.12 Temperature and velocity fields of the large fire (7.5 kW) in configuration B (blocks at the center) and configuration C (blocks at the side) for block1 (ψ=15%) at the condition $L/\overline{H} = 0.4$. The ventilation velocity is 0.55 m/s. . 92

List of tables

2.1 Details of the meshes adopted in the grid sensitivity study. 20

4.1 Enthalpy of combustion for fossil fuels and relative temperature rise predicted by the model (neglecting radiative heat losses). 51

4.2 Details of the meshes adopted in the grid sensitivity study. 54

4.3 Plume parameters for propane and pool fire for using the model presented in Sect. 4.2.2, assuming heat losses by radiation equal to the 30% of the HRR ($\Delta T = T_i - T_0 = 1400$ K) and no heat losses ($\Delta T = T_i - T_0 = 2000$ K). . . . 57

5.1 Tunnel geometry of reduced scale tests in previous study. 68

5.2 Test conditions for tunnel inclined from -5° to +5°. 72

Nomenclature

Roman Symbols

$\dot{m}$	Mass flow rate
$\overline{H}$	Tunnel hydraulic diameter
$\widehat{\mathrm{Fr}}_c$	Modified critical Froude number provided by the model
A	Tunnel cross-sectional area
b	Radius of the plume
B_i	Buoyancy flux at the source
C	Constant
C_k	Constant
c_p	Specific heat capacity
C_x	Drag coefficient
D^*	Characteristic fire diameter
e	Tunnel wall thickness
Fr_c	Critical Froude number
Fr_W	Critical Froude number defined by the tunnel width
g	Gravitational acceleration
H	Height of the tunnel
k	Constant

L	Fire-blockage distance
l	Backlayering length
M	Molar mass
n	Scaling factor
Q	Heat release rate
q	Volume flow rate
Q^*	Non-dimensional heat release rate
R	universal gas constant
Re	Reynolds number
Ri_c	Critical Richardson number
s	Tunnel slope in percentage
T	Temperature
u	Plume velocity at the longitudinal direction
V	Ventilation velocity
V_c^*	Non-dimensional critical ventilation velocity
W	Width of the tunnel
w	Vertical velocity of the plume

Greek Symbols

α	Plume entrainment coefficient
α_0	A reference value for the ‘top-hat’ entrainment coefficient for a pure plume
β	Modified plume radius
η	Density deficit
$\varGamma$	Plume Richardson number
γ	Head loss coefficient

λ	Tunnel wall thermal conductivity
ψ	Tunnel blockage ratio
ρ	Density
θ	Tunnel slope in degree
φ	Constant
$\widetilde{\eta}$	Modified density deficit
$\widetilde{\varGamma}$	Modified plume Richardson number

Subscripts

$\square_0$	Property at the ambient condition
$\square_c$	Property of ventilation at the critical condition
$\square_F$	Parameter for the forced plume
$\square_H$	Property of plume at the ceiling
$\square_i$	Property of plume at the source
$\square_L$	Parameter for the lazy plume
$\square_P$	Parameter for the planar 2D source

Acronyms / Abbreviations

CFD	Computational Fluid Dynamics
FDS	Fire Dynamics Simulator
HRR	Heat release rate
LES	Large Eddy Simulation
RANS	Reynolds Averaged Navier-Stokes

Chapter 1

Introduction

1.1 Tunnel fire hazards

Compared with the fires in open spaces, the tunnel fires are characterised by three main features. Firstly, tunnel is a long confined space in which the heat released by combustion cannot be removed easily. The temperature can raise quickly and may reach 1000 °C in the fire region. This high temperature imposes serious threat both to the people and to the structure of the tunnel. Secondly, due to the combustion of the combustible vehicle materials, toxic gases may be released. Because of the lack of the oxygen, the combustion is often incomplete, and a large amount of smoke may be then produced. The toxic smoke causes low visibility as well as chocks. The third is the difficulty in the firefighting. When the fire starts, fire fighters need to locate the fire source and enter the tunnel. However, The low visibility and the presence of abandoned vehicles in the road make it hard for the fire fighters to get close to the source.

Several severe fire disasters in tunnels have been reported so far. Examples are the fires in Mont Blanc in 1999 causing 38 deaths (Vuilleumier et al., 2002), Tauern in 1999 causing 12 deaths (Leitner, 2001), St. Gotthard in 2001 causing 11 deaths, Daegu in 2003 causing 198 deaths (Hong, 2004), and Viamala Tunnel in 2006 causing 9 deaths.

In Europe, the case of the Mont Blanc tunnel has attracted extensive attention. The Mont Blanc Tunnel is a tunnel connecting France and Italy. The tunnel is 11.6 km in length, 8.6 m in width, and 4.35 m in height. The passageway is not horizontal, but in a slightly inverted "V", which assists ventilation. The tunnel is run by France and Italy together. In 1999 a Belgian transport truck carrying flour and margarine caught fire in the tunnel. Despite immediate rescue operations, 38 people died and the tunnel remained closed for three years after the fire. In the accident when the truck driver stopped the vehicle in the middle of the tunnel and failed to fight the fire, the fire alarm was triggered and further entering of cars were stopped, but there were still many vehicles left in the tunnel. Within minutes, two fire trucks from France responded to the unfolding disaster, but due to the smokes and the presence of abandoned vehicles, the fire engines were unable to proceed. The fire burned for 53 hours and the temperature within the tunnel reached 1000 °C. Due to weather conditions, the airflow through the tunnel was from the Italian side to the French side. Authorities compounded the effect by pumping in further fresh air from the Italian side, feeding the fire and forcing poisonous black smoke through the length of the tunnel. Only vehicles below the fire on the French side of the tunnel were trapped, while cars on the Italian side of the fire were mostly unaffected. There were 27 deaths in vehicles, and 10 more died trying to escape.

As this example shows, due to the high traffic and the difficulty in escaping, the losses in tunnel fires are usually large. Proper operation systems in response to the fire need therefore to be developed.

1.2 Ventilation strategies

Tunnel ventilation systems are usually installed to remove the heat and contaminant produced by vehicles in the normal operation. The ventilation systems can be divided into two main categories: natural ventilation and mechanical ventilation systems. For very short tunnels or tunnels with large shafts, natural ventilation is usually enough. For long tunnels, mechanical ventilation systems are usually needed. Mechanical ventilation systems provide a more controllable way of removing hazards from tunnels and are not dependent on environmental conditions. Although originally designed to cope with the contaminant produced by vehicles, the role of mechanical ventilation in case of fires have received attention, due to a large number of tunnel fire accidents that occurred in the last decades. The mechanical ventilation systems used in tunnels include two typologies: longitudinal ventilation and transverse ventilation.

1.2.1 Longitudinal ventilation

In case of a fire, a longitudinal ventilation system (Fig. 1.1) is designed to produce a longitudinal flow to create a smoke-free path upstream of the fire, while vehicles downstream of the fire are exposed to smoke. The system is suitable for one-way tunnels and the evacuation is supposed to be conducted upstream. Users placed downstream the fire are supposed to escape out of the tunnel by driving their vehicles. Two most important parameters in this system are the critical velocity and the backlayering length. The critical velocity is the minimum ventilation velocity that prevents the smoke from flowing upstream the source; the

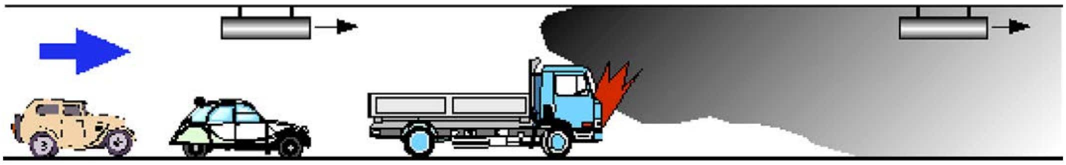

Fig. 1.1 Fire-induced smoke longitudinal control (Vauquelin, 2008).

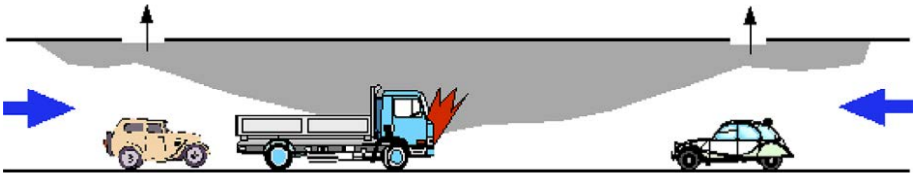

Fig. 1.2 Fire-induced smoke transverse control (Vauquelin, 2008).

backlayering length is the length of the smoke backlayering upstream of the fire when the ventilation velocity is lower than the critical velocity. The relationship between these two parameters and the fire heat release rate is a classical topic in the fire safety engineering.

Longitudinal ventilation systems have been widely adopted since they provide a very cheap solution. These systems present, however, some shortcomings. Firstly, this system is only suitable for a one-way tunnel. Secondly, the extra air added by the ventilation feeds the combustion. Thirdly, the ventilation velocity is constant all over the tunnel even if the fire is localized at one place, which implies a large energy consumption.

1.2.2 Transverse ventilation

A transverse ventilation system (Fig. 1.2) is required for bi-directional long tunnels and highly recommended for frequently congested one-directional long tunnels. This system allows the smoke flows (plume flows) arising from a fire to be directly exhausted using extraction vents in the vicinity of the fire, so that people could be evacuated in both tunnel directions. In case of a fire, the location of the fire is first determined by the fire detection system and then the extraction vent or vents nearby the fire site are opened to extract smoke flows. The important parameters in this system are the ventilation system efficiency (VSE) and the ventilation system output (VSO). VSE is the ratio between the flow rate of smoke extracted and the smoke flow rate; VSO is the ratio between the flow rate of smoke extracted and the extraction flow rate. An extraction ventilation system must be powerful enough to create longitudinal flows from both sides to confine the smoke between the vents and the fire source.

1.3 Investigation methods

The ideal method is to conduct large-scale tests in real tunnels, but this method is costly and certain parameters (e.g. tunnel geometry) cannot be easily modified for research purposes. The main experimental approach in the tunnel fire study is conducting small-scale tests, i.e. setting fires in tunnels whose sizes are proportionally reduced compared to real tunnels. In small-scale tests, the fire smokes can also be modeled by densimetric flows (salt water or low density gases), which provides a safer way of doing such investigations. Due to its development, computational fluid dynamics (CFD) attracts an increasing attention. Among the software developed specifically for the fire modeling, Fire Dynamics Simulator (developed by NIST) and FireFOAM (based on OpenFOAM) are probably the most widely used ones by the fire engineering community.

1.3.1 Large-scale tests

Large-scale testing is generally costly, as they are time consuming, and logistically complicated to perform. However, they can provide valuable information to verify the results obtained with other methods. Here is a brief introduction of a few recent large-scale fire tests.

The EUREKA EU499 (1992) test program was performed in an abandoned tunnel named Repparfjord Tunnel in northern Norway. The tunnel was 2.3 km long with a slope less than 1 %, 5.3–7.0 m wide and 4.8-5.5 m high. Twenty one large-scale tests were performed, with real vehicles, as well as wood cribs and heptane pool fires. The program was intended to provide information on the fire behavior of different type of fuels, possibilities of escape and rescue, fire extinguishing and the effect of the fire on the tunnel structure.

The Buxton (1993) test program was carried out in a 2.56 m high, 366 m long colliery arch-shaped tunnel with a cross-section of 5.4 m^2. Kerosene pool fires with heat release rate 0.3-20 MW were investigated. Twelve experiments were conducted in an unobstructed tunnel and eight experiments were conducted with a scale model train. The program was to investigate the interaction between the longitudinal ventilation and the smoke backlayer and to provide validation data for CFD simulations.

The Memorial (1995) test program was performed in a two-lane, 853 m long and 8.8 m wide road tunnel with a changing cross-section. The tunnel has a 3.2 % upgrade from south to north portal. The program consisted of 98 tests conducted in different ventilation systems. Transverse, semi-transverse and longitudinal ventilation systems were all investigated. Results obtained with different fire source sizes and different ventilation velocities were recorded.

The Shimizu (2001) test program was performed in a three-lane No. 3 Shimizu tunnel on the New Toumei expressway in Japan. The tunnel was 1119 m long with a slope of 2 % down from west to east, the tunnel width was 16.5 m, the height was 8.5 m, the cross-section was a semicircle. The program was designed to provide fire information in a large cross-section. Fire behavior regarding combustion rate, formation of smoke layer, interaction of longitudinal flow on the smoke distribution, behavior of Fixed Fire Fighting Systems (FFFS) on the smoke layer, and risk for fire spread were investigated.

The Runhamar (2003) test program was performed in a two-way-asphalted road tunnel. The tunnel was 1600 m long, 6 m high and 9 m wide, with a slope varying between 0.5–1 %. The tunnel was a blasted rock-tunnel with a cross-section varying between 47 and 50 m^2. The program investigated fires on HGV-trailers (Heavy Goods Vehicle) with different cargo materials, influence of the heat release rate and of the gas temperature on the airflow were studied.

1.3.2 Small-scale tests

The physical scaling has been widely used in the fire safety engineering community. Small-scale experiments allow the experimental conditions to be controlled by the researchers and parametric studies to be carried out in a more economic way (than large-scale tests). The most common scaling technique used in the fire community is the ‘Froude scaling’. The Froude number is a non-dimensional parameter, defined as the ratio of inertial forces to buoyancy forces. In the Froude scaling, the Froude number is preserved while the Reynolds number is kept sufficiently high to ensure a fully turbulent flow. The fire source could be modeled by propane fires (Oka and Atkinson (1995), Wu and Bakar (2000), Li et al. (2010)) or pool fires (Ko et al. (2010), Weng et al. (2015)).

Adopting the Froude scaling, parameters obtained in the experiment have a relationship with the full-scale case. In the tunnel fire study, the non-dimensional heat release rate (Q^*) and critical velocity (V^*) are usually defined as: $Q^* = \dfrac{Q}{\rho_0 c_p T_0 g^{1/2} H^{5/2}}$, $V_c^* = \dfrac{V_c}{\sqrt{gH}}$ (Oka and Atkinson, 1995), where ρ_0 and T_0 are the reference ambient air density and temperature, respectively, c_p is the heat capacity, H is the tunnel height and g is the gravitational acceleration. Assuming that the geometry scale is n, then the heat release Q rescales as $n^{5/2}$ and the velocity $V_c \propto n^{1/2}$.

Another physical scaling technique is the analog scaling, that uses two fluids of different densities to model smoke movement in a fire scenario. The two fluids can be for example helium and air (Vauquelin, 2008), or water and salt water, or even fine hydrogen bubbles and water (Li et al., 2003). This method simulates the fire smoke using a density difference, rather than a temperature difference, and the Froude number is preserved. The analog scaling requires a determination of fluid density based on a reference gas temperature in a specific fire. This is not easy, since gas temperature changes significantly with position in many fire scenarios. Moreover, this method cannot model the heat loss at the tunnel walls. Nevertheless, it provides a simple way to study the flow dynamics, since it allows the density and the flow rate at the source to be accurately controlled.

1.3.3 Numerical simulations

With the development of powerful computers and numerical techniques, CFD has attracted an increasing attention in the fire engineering community. CFD codes solve Navier–Stokes equations in a discretized domain, and permit a fine resolution of the problem in space and time for all the parameters of interest.

The Navier–Stokes equations can be numerically solved without any turbulence model using Direct Numerical Simulation (DNS). However the computational costs of this approach are very high, which is not suitable for the engineering application. Depending on the approach used to model turbulent transfers, numerical simulations are usually divided in two groups: Reynolds-Averaged Navier–Stokes (RANS) simulations and Large Eddy Simulations (LES). A RANS model solves the time averaged equations introducing two (or more) equations to model the Reynolds stresses. LES method directly simulates the dynamics of larger eddies, while small eddies are filtered and their influence is taken into account through subgrid models. LES is time-dependent and three-dimensional, and is able to capture unsteady turbulent fire phenomena, but requires greater computational resources than RANS methods.

1.4 Overview of the study

1.4.1 Objectives

This work aims in shedding light on aspects concerning the dynamics of the buoyant releases in ventilated tunnels which are still not clarified. Specifically, we focus on the study of the critical velocity in longitudinal ventilated tunnels. The main objectives of the current study are:

- Propose an analytical solution of the critical velocity of buoyant plume in a ventilated tunnel based on the classical plume equations.

- Discuss the appearance of the so-called ‘super-critical’ velocity, a ventilation velocity that becomes independent of the heat release rate when it becomes large.
- Study the effect of tunnel inclination on the critical velocity; propose an analytical solution.
- Study the effect of vehicular blockage on the critical velocity.

1.4.2 Plan of the work

The results of the present research work are presented in the form of research papers in four different chapters. Note that this way of structuring the manuscript inevitably involves some repetitions of basic concepts, especially concerning the experimental apparatus and the numerical set-up, which will be initially presented in Chapter 2.

In Chapter 3 we explore theoretically and experimentally the dependency of the critical velocity on the dynamical condition of the source and on the geometry parameters characterizing the source and the tunnel section. To that purpose we focus on densimetric plumes produced by steady and controlled releases of light gases in a ventilated horizontal tunnel. the critical velocity of forced and lazy releases is investigated and the non-Boussinesq effects (the effect due to large differences between the densities of the buoyant plume and the ambient fluid) are discussed. Asymptotic solutions of the model are presented. They allow predicting the dependence of the critical velocity on the main governing parameters in a simple form.

In Chapter 4, 5, 6 we subsequently investigate more realistic conditions involving the presence of a fire, the inclination of the tunnel and the presence of obstacles within the tunnel.

Chapter 4 focuses on the critical velocity in longitudinally ventilated tunnels and on its dependence on the power of the fire source. Here we discuss the reasons for the appearance of the ‘super-critical’ velocity: the independence of the critical velocity on heat release rate when this becomes large for large fires. The roles of the diffusive heat fluxes at the tunnel walls, the radiative fluxes and the presence of large flames are also investigated.

Chapter 5 is dedicated to study the effect of tunnel inclination on the critical velocity. The influence of the dynamical conditions at the source is studied for both densimetric plumes and propane fires. A theoretical model based on the horizontal case in Chapter 3 is presented to discuss the effect of the dynamical condition at the source on the critical velocity.

Chapter 6 focuses on the effect of vehicular blocks on the critical velocity. The tunnel blockage ratio, fire-blockage distance and the relative position of the block and the fire source are studied.

Chapter 7 offers some conclusions and perspectives.

In the Appendix, we present a brief introduction of the numerical tool Fire Dynamics Simulator.

Note that in the fire safety literature, there are generally two different definitions of critical ventilation velocity Grant et al. (1998). According to the first definition, the critical velocity is the minimum velocity that prevents the formation of backflow once that the buoyant releases impinge on the ceiling. In the second definition, which is more frequent: the critical velocity is determined as the minimum velocity that prevents the backlayer flow to move upstream of the source. It is worth-noting that in this work we will use both definitions. In Chapter 3, in order to formulate a simple theoretical model based on a integral ‘top-hat’ plume, we will use the first definition, since this will allow us to avoid modeling the backlayer flow at the ceiling. In the remaining part of the work; i.e. Chapter 4, 5, 6, we will instead use the second definition, a choice which is made by the need of comparing our experimental results to literature results. Note also that the values of the two critical velocities determined based on these definitions are, according to our results, of the same order of the experimental uncertainty, i.e. ±10%, in case of a circular source. There are instead relevant differences between the two definitions in case of planar 2D sources, occupying the whole tunnel section, as well as in the case of large fire plumes, in which the extent of flame is of the same order of the ceiling.

Chapter 2

Methods

This study combines theoretical, experimental and numerical methods.

2.1 Theoretical methods

The localized release of a fluid whose density ρ_i is lower than that of the ambient fluid ρ_0 induce dynamical effects which are significantly affected by the role of the buoyancy $\frac{\rho_i - \rho_0}{\rho_0} g$ (g is the gravitational acceleration). These releases have been extensively studied in the literature, since the pioneering work by Morton et al. (1956), who proposed a single integrated model of a rising plume, induced by a localized injection of a buoyancy flux, refereed to here as B_i. The plume equations given by Morton et al. (1956) are:

$$\begin{cases} \frac{\mathrm{d}}{\mathrm{d}y}(\rho w b^2) = 2\rho_0 u_e b, & \text{(2.1a)} \\ \frac{\mathrm{d}}{\mathrm{d}y}(\rho w^2 b^2) = (\rho_0 - \rho) g b^2, & \text{(2.1b)} \\ \frac{\mathrm{d}}{\mathrm{d}y}\left[(\rho_0 - \rho) w b^2\right] = 0, & \text{(2.1c)} \end{cases}$$

where b is the characteristic plume radius, w is its vertical velocity, ρ is the plume density, ρ_0 is the ambient fluid density and $u_e = \alpha w$ is the entrainment velocity, α is the entrainment coefficient. The entrainment coefficient α is here assumed to be of the form $\alpha = \alpha_0 (\rho/\rho_0)^{1/2}$ as is customary when dealing with non-Boussinesq releases (Rooney and Linden, 1996; Van Den Bremer and Hunt, 2010), where $\alpha_0 = 0.127$ is a reference value for the 'top-hat' entrainment coefficient for a pure plume. A sketch of the plume adapted from Michaux and Vauquelin (2008) is shown in Fig. 2.1. Plume parameters b, ρ, w are dependent on y, the vertical distance above the source. To solve the equations (2.1a-2.1c), the plume Richardson number is introduced, defined as $\Gamma = \frac{5}{8\alpha_0}\frac{\eta g b}{w^2}$, with $\eta = \frac{\rho_0 - \rho}{\rho_0}$. The plume Richardson number Γ allows for a classification of buoyant releases in momentum-driven forced plumes ($\Gamma < 1$), and buoyancy-driven pure ($\Gamma = 1$) and lazy ($\Gamma > 1$) plumes (Hunt and Kaye, 2005).

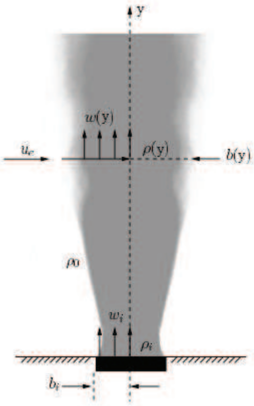

Fig. 2.1 Sketch of the plume, adapted from Michaux and Vauquelin (2008).

In this study we adopt a simple model of buoyant plume in a ventilated tunnel based on the plume equations (2.1). The effect of the tunnel ventilation will be taken into account by a drag force exerted by the crossflow on the plume:

$$\frac{\mathrm{d}}{\mathrm{d}y}(\rho u w b^2) = C_x\sqrt{\rho\rho_0}(V-u)^2 b/\pi \tag{2.2}$$

where u is the longitudinal velocity, V is the ventilation velocity, and C_x is a drag coefficient. The critical condition can then be computed by assuming the momentum balance between the longitudinal ventilation and the flow after impingement on the ceiling. This model is explained in detail in Chapter 3.

2.2 Experimental methods

The experiments were performed in a small-scale longitudinal ventilated tunnel at LMFA, Ecole Centrale de Lyon. A photo of the tunnel is shown in Fig. 2.2. The tunnel is 9 m in length and 0.36 m in width. The height could be adjusted at 0.185 m or 0.36 m. Two different experimental set-ups were designed: the isothermal model and the thermal model. The basic structures of the two models are the same, except that different source is used. The photos of the sources are shown in Fig. 2.3, the tests of which are presented in 2.2.3. Most tests were performed in the isothermal model, except for a few cases in Chapter 4, in which the effect of heat losses on the critical velocity is discussed.

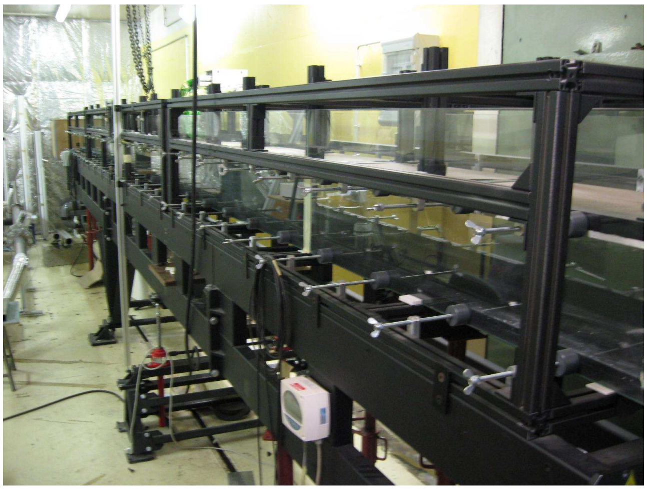

Fig. 2.2 Experimental installation at LMFA.

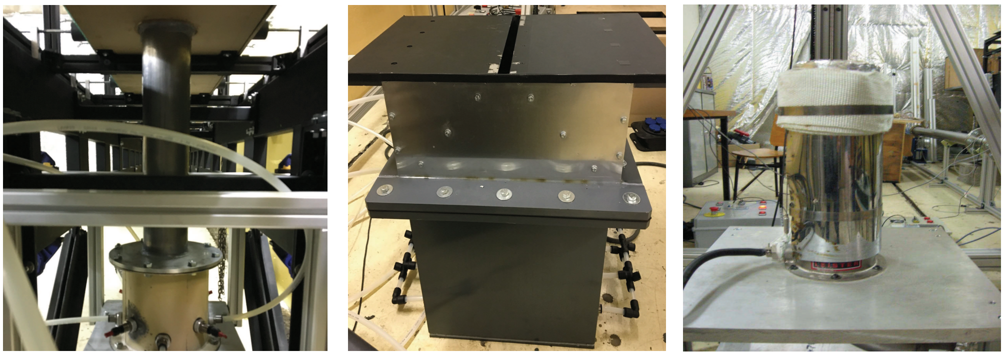

Fig. 2.3 Photos of the sources: isothermal circular source, isothermal planar 2D source and thermal circular source.

2.2.1 Isothermal experiments

In the isothermal experiments (Fig. 2.4), the tunnel height is fixed at 0.185 m in most tests, except for a few cases in Chapter 3, where some tests are conducted at a tunnel height of 0.36 m. The diameter of the circular source is varied at 100, 75, 50, 35, 25 mm. The length and width of the planar source are 40×360 mm, 20×360 mm, and 10×360 mm. In Chapter 3 both the circular source and the two-dimensional planar source are used, while in the other chapters only the circular source is used. The buoyant plume is modeled by the air/helium mixture, the flow rates of which are controlled and measured independently. The flow rates of air and helium for a certain plume with density ρ_i and flow rate q_i at the source are:

$$\begin{cases} q_{air} = q_i \dfrac{\rho_i - \rho_{He}}{\rho_0 - \rho_{He}}, \\ q_{He} = q_i - q_{air}. \end{cases} \tag{2.3}$$

The density of the buoyant plume can be adjusted by changing the mixing ratio. The average velocity at the source w_i could be computed as: $q_i = w_i A_i$, where A_i is area of the source (circular or planar). To visualize the flow, a tiny fraction of nebulised oil is added into the mixture, and a lens is installed at the inlet of the tunnel.

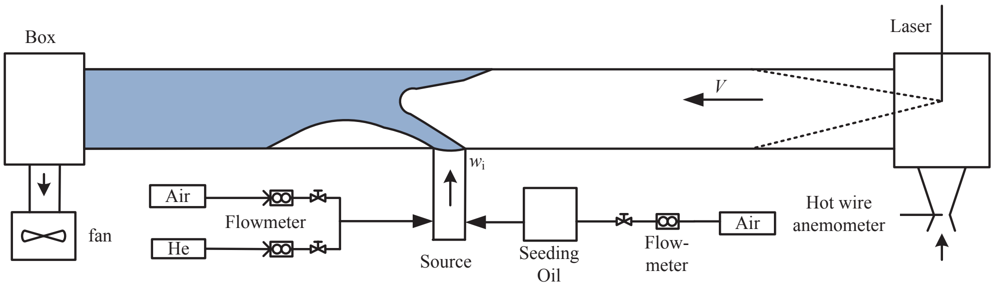

Fig. 2.4 Schematic of the experimental set-up for the isothermal model.

The ventilation is provided by an extracting fan connected to a box placed at the tunnel outlet. The ventilation velocity V is measured by a hot wire anemometer placed within a Venturi tube at the inlet. The reason for not putting directly the hot wire anemometer at the tunnel center is that the anemometer is not designed to measure a small velocity. Instead, the anemometer is placed within a Venturi tube to measure the flow rate of the ventilation flow. The relationship between the velocity measured by the anemometer and the flow rate is obtained by tests done in another experimental set-up, shown in Fig. 2.5. A fan is put after the flow meter to create a ventilation flow. A Venturi tube with the hot-wire anemometer is installed at the entrance before the flow meter. Note that the fan should not be put between the Venturi tube and the flow meter, to ensure that the flow rate measured by the anemometer is the same as the flow rate measured by the flow meter, since there might be a leakage at the fan. Fig. 2.6 shows the relationship between the velocity measured by the hot wire anemometer and the flow rate measured by the flow meter. A linear fit was conducted and a correlation was obtained:

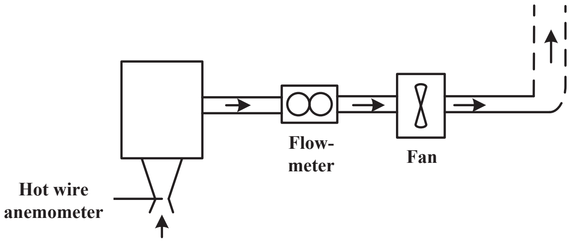

Fig. 2.5 Experimental set-up to determine the relationship between the velocity measured by the hot wire anemometer and the flow rate measured by the flow meter .

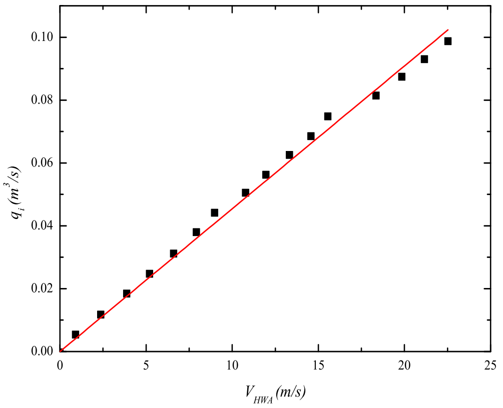

Fig. 2.6 Relationship between the flow rate and the velocity measured by the hot wire anemometer.

$$q_i = 0.0045V_{HWA} \tag{2.4}$$

where q_i is the flow rate (m^3/s) and V_{HWA} (m/s) is the velocity measured by the hot wire anemometer. Finally the ventilation velocity is obtained as: $V = \frac{q_i}{A} = \frac{0.0045V_{HWA}}{A}$, A is the tunnel cross-sectional area.

The critical condition is defined by flow visualization, adjusting the power of the fan to set the front of the backlayering flow (the smoke flow directed against the ventilation flow, see 1.2.1) at the source position. A typical critical ventilation condition is shown in Fig. 2.7.

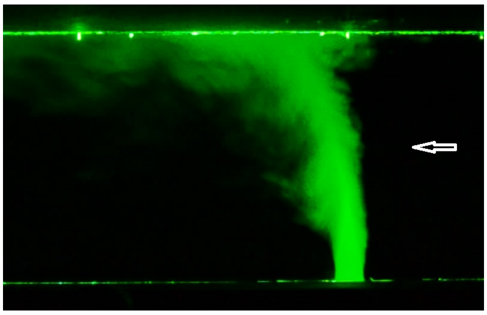

Fig. 2.7 Critical ventilation condition in the isothermal experiment (circular source, $\Gamma_i =$ 0.015, D_i=25 mm).

2.2.2 Thermal experiments

In the thermal experiments (Fig. 2.8), the tunnel height is fixed at 0.185 m and the diameter of the circular source is 100 mm. The ventilation system is the same as the isothermal model. Heat release rates between 700 W and 10 kW are produced using a fan and an electric heater, controlled and regulated in temperature by a PID controller. The backlayering length is estimated using K-type thermocouples measuring air temperature, since the temperature of the backlayer is higher than the ambient. The thermocouples are installed on the tunnel axis at the ceiling level (2 cm below the ceiling) and 2 cm apart. The critical velocity is obtained by interpolation when the backlayering length is zero.

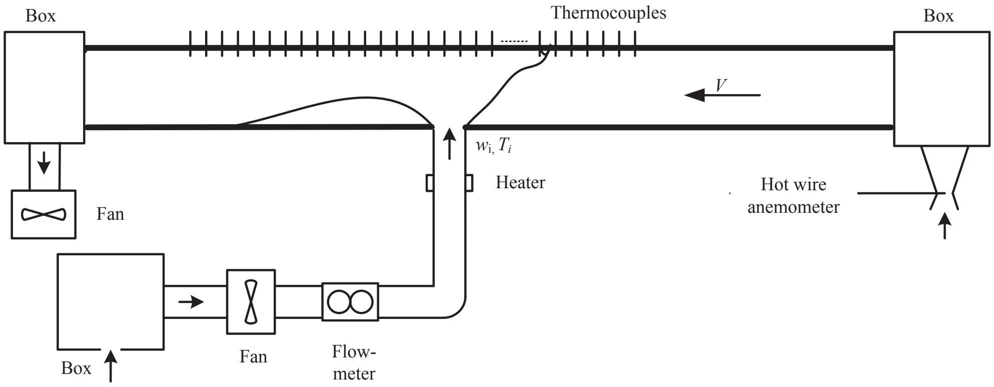

Fig. 2.8 Schematic of the experimental set-up for the thermal model.

An example of the temperature profiles at different times from the beginning to the end of one test (t = 3500 s) in the thermal experiment is shown in Fig. 2.9. Backlayering length is taken as the distance between the place we observe sudden temperature rise from the ambient and the source. A detailed description of the experimental protocol and of the measurements techniques used in the thermal experiments is provided in Salizzoni et al. (2017).

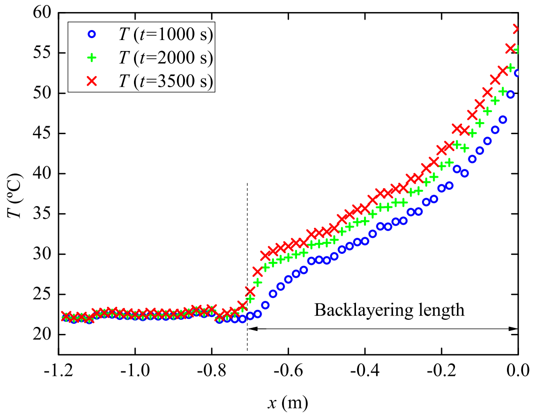

Fig. 2.9 Temperature at the tunnel ceiling as a function of the distance from the source in the thermal model; the experimental conditions are T_i = 280 °C, w_i =1.17 m/s, V = 0.205 m/s, Γ_i = 1.

2.2.3 Tests of the sources

The schematic diagram of the tests of the sources is shown in Fig. 2.10. A fan is put after the flow meter and before the source (Fig. 2.3), to create a ventilation flow. A pitot tube is put just at the outlet of the source, to measure the velocity profile.

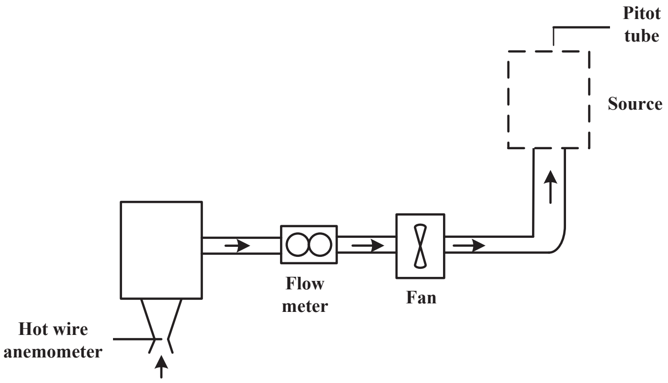

Fig. 2.10 Schematic of the sources tests, the three sources shown in Fig. 2.3 are connected to the outlet of the fan, a pitot tube is put at the outlet of the source to measure the velocity profile.

The schematic diagram of the circular and planar source used in the isothermal experiment is shown in Fig. 2.11. The diameter of the circular source D_i is varied at 100, 75, 50, 35, 25 mm. The length (L_P) and width (W_P) of the planar source are 40×360 mm, 20×360 mm, and 10×360 mm. The width of the planar source is the same as the width of the tunnel.

The velocity profile of the isothermal circular source at five diameters is shown in Fig. 2.12. The velocity is almost a constant except for the case at D_i=100 mm, when the velocity is low. The velocity profile of the isothermal planar source at z direction is shown in Fig.

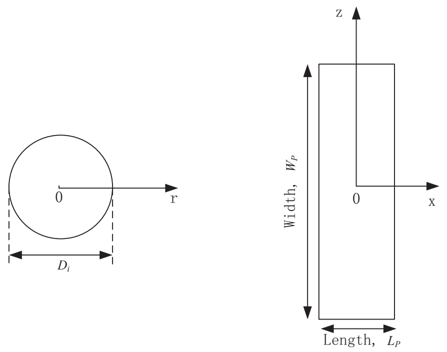

Fig. 2.11 Circular and planar source used in the isothermal experiment, photos are shown in Fig. 2.3.

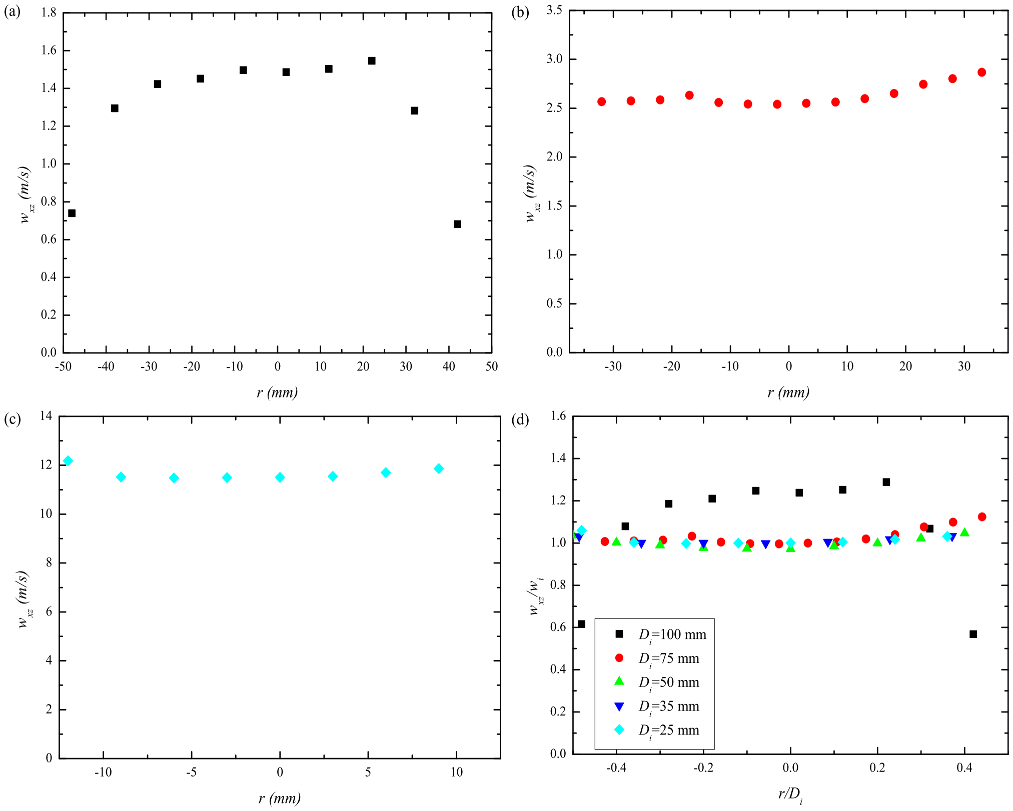

Fig. 2.12 Velocity profile of the isothermal circular source: (a) $D_i = 100$ mm, (b) $D_i = 75$ mm, (c) $D_i = 25$ mm, (d) non-dimensional velocity profile at $D_i = 100, 75, 50, 35, 25$ mm.

2.13 and at x direction is shown in Fig. 2.14. For the planar source, the velocity is close to a constant in the lateral direction of the tunnel (z). In the longitudinal direction (x), the velocity is close to a constant except in the boundary layers.

The diameter of the thermal circular source is fixed at 100 mm, the geometry is the same as the circular source in the isothermal model. The non-dimensional velocity profile is shown in Fig. 2.15. The velocity profile of the thermal and isothermal circular source is similar.

2.3 Numerical methods

The numerical simulation is carried out with an open source software FDS 6.3, with a detailed description provided in Appendix A. FDS solves the Navier-Stokes equations in LES. In the simulation, the large eddies of the flow are simulated and the smaller are modeled by a subgrid model (Deardorff's model).

There are two tunnel sizes in the numerical simulation. One tunnel is $24H$ (length) × $2H$ (width) × H (height). This tunnel is to simulate tunnel C in Wu and Bakar (2000) and is only

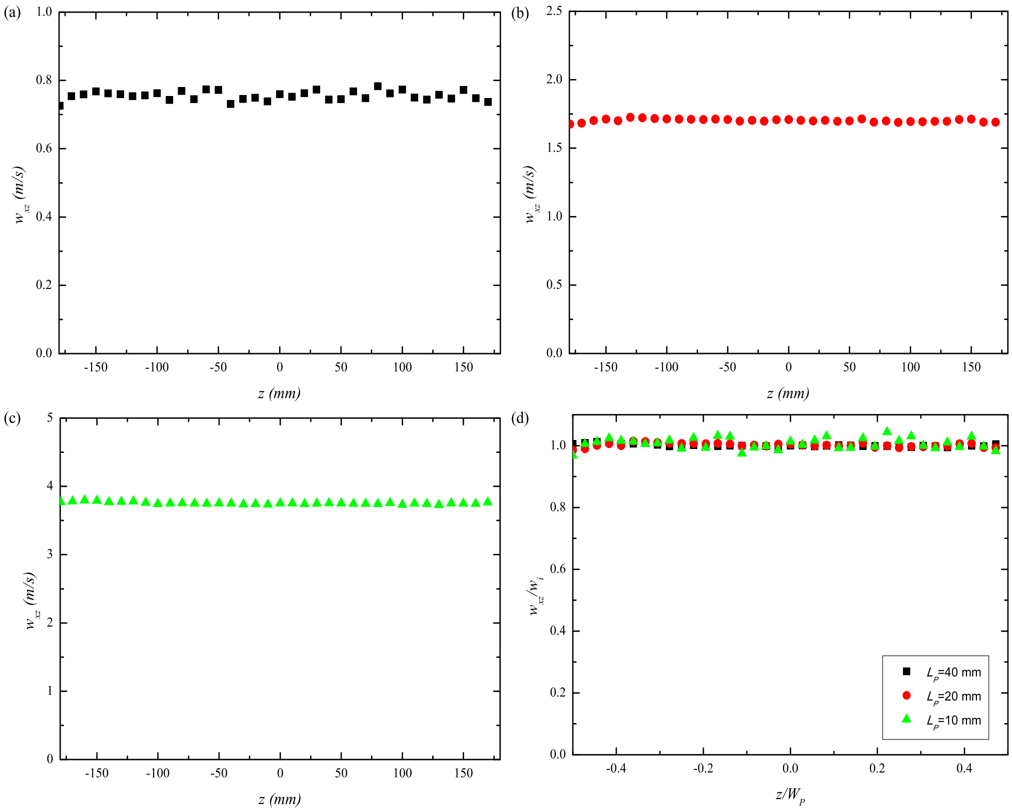

Fig. 2.13 Velocity profile of the isothermal planar source at the z (width) direction measured at x=0: (a) $L_p = 40$ mm, (b) $L_p = 20$ mm, (c) $L_p = 10$ mm, (d) non-dimensional velocity profile.

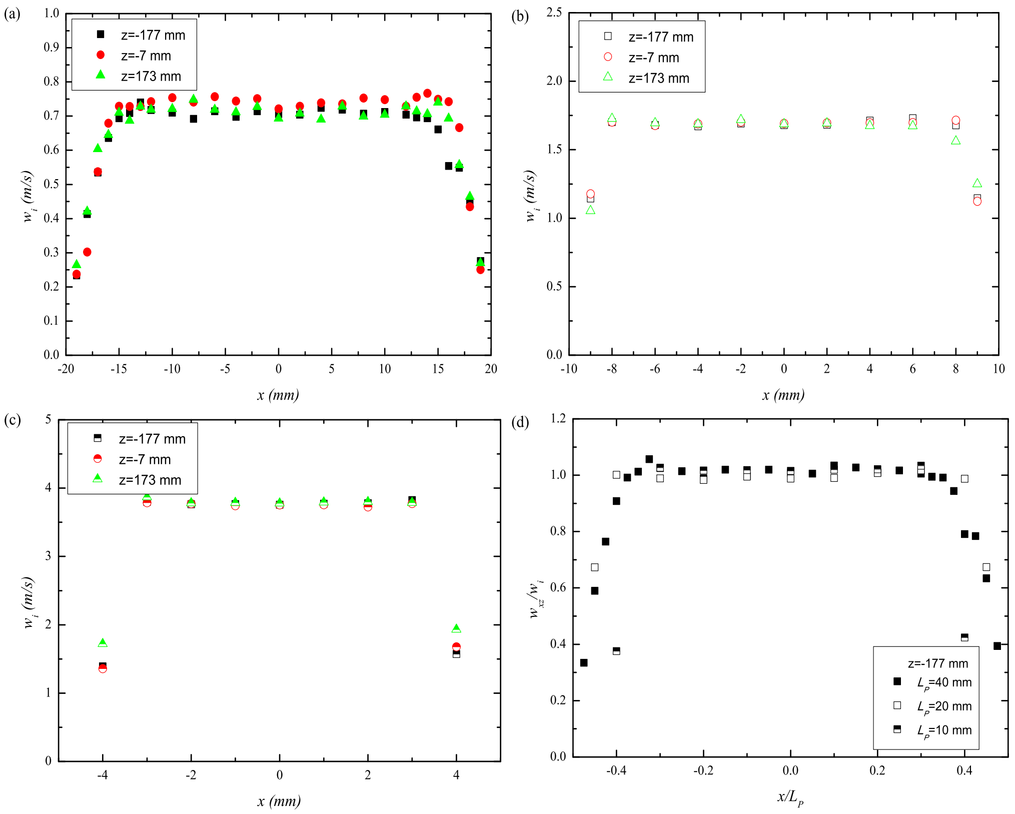

Fig. 2.14 Velocity profile of the isothermal planar source at the *x* (length) direction measured at *z*=-177, -7, 173 mm: (a) $L_p = 40$ mm, (b) $L_p = 20$ mm, (c) $L_p = 10$ mm, (d) non-dimensional velocity profile.

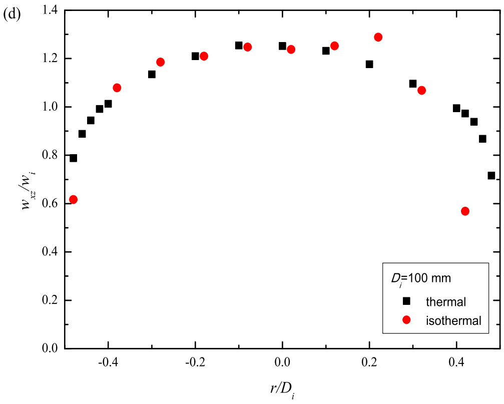

Fig. 2.15 Non-dimensional velocity profile of the thermal (w_i=1.6 m/s) and isothermal (w_i=1.2 m/s) circular source at D_i=100 mm.

used in Chapter 4. Another tunnel is $33H$ (length) $\times$ $2H$ (width) $\times$ H (height). This tunnel is to simulate the tunnel in the experiment and is used in Chapter 5 and Chapter 6. Note that the tunnel length is reduced to save computing time.

In the numerical model, the ventilation velocity was fixed at inlet and at outlet it was set 'open'. The tunnel inclination was adapted by varying gravity components in x and y direction. The circular source in the experiment was modeled by square source with the same area. The source was located 4.5 m away from inlet and at the tunnel center. The physical property of the wall was defined as 'concrete' with the wall backed up to ambient. The physical property of the vehicular block was defined as 'steel'. A set of 50 thermocouples were put 2 cm below ceiling in a region of 1.0 m (from 0.5 m upstream to 0.5 m downstream of the fire source) to measure the backlayering length. The simulation concerns both densimetric plumes and fire plumes (propane). The densimetric plumes simulations can be compared with the experimental data. The fire plumes simulations allow us to study the effect of combustion and heat transfer. Each simulation lasted 60 s. The flow required approximately 30 s to reach a steady state (statistically). Therefore the position of the backlayer flow was obtained by averaging the velocity field between 30 s and 60 s.

To get reliable results from LES simulations, fine enough grids should be considered. According to McGrattan et al. (2008) the mesh size close to the fire source has to be estimated depending on a characteristic fire diameter defined as:

$$D^* = \left(\frac{Q}{\rho_0 c_p T_0 \sqrt{g}} \right)^{\frac{2}{5}} \tag{2.5}$$

whose ratio on the grid size Δx values have to be in the range $4 \leq D^*/\Delta x \leq 16$. For a HRR of about 3 kW, D^* is approximately 0.09 m, and therefore $\Delta x \simeq 0.01$ m.

To save computing time, mesh stretching was used along the longitudinal direction, to provide finer grids near the source. The tunnel is divided into three sub-domains: the domain close to the inlet is referred to as the 'Left Domain', the domain within which is placed the heat source is the 'Middle Domain', and that close to the outlet is the 'Right Domain'. The lengths for the three domains are 4 m, 1 m and 1 m, respectively.

Before performing the numerical experiments we carried out a grid sensitivity study in a horizontal empty tunnel ($24H$ $\times$ $2H$ $\times$ H), to evaluate the dependence of our numerical solution on the resolution of the mesh. The mesh sizes are listed in Table 2.1. In this grid study we focus on longitudinal profiles of the mean and the standard deviation of the temperature registered by the thermocouples. Based on the results shown in Fig. 2.16, we adopted Grid 4 as the reference grid for our numerical study, made up of 756000 cells. Note

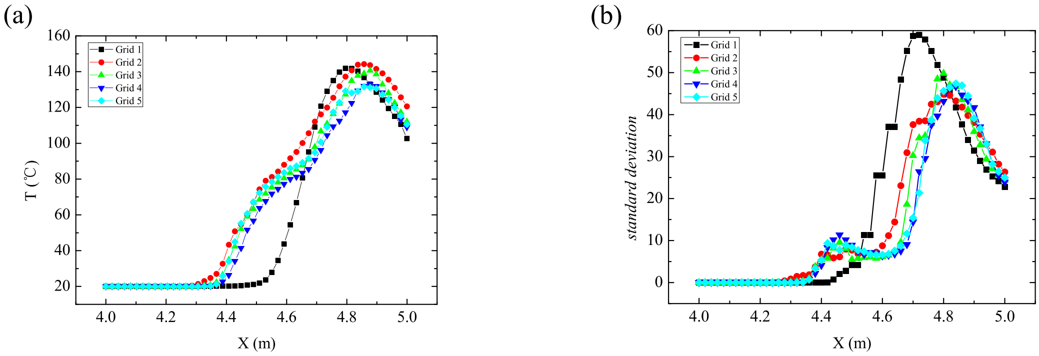

Fig. 2.16 Longitudinal profiles of the mean and of the standard deviation of the temperature along the tunnel ceiling for the five girds tested (See Table 2.1).

that Eq. (2.5) implies a higher mesh resolution for smaller fires. In the present study the smallest fire was 0.20 kW, which makes $D^*/\Delta x = 4$, i.e. within the recommended range.

Test	Number of cells X Y Z	Total cells	Cells size in the Middle domain (as a fraction of H)	Cells size in the Right and Left Domains (as a fraction of H)
Grid 1	300 25 12	90000	$0.08\times0.08\times0.08$	$0.08\times0.08\times0.08$
Grid 2	350 50 25	437500	$0.04\times0.04\times0.04$	$0.08\times0.04\times0.04$
Grid 3	378 54 27	551124	$0.036\times0.036\times0.036$	$0.072\times0.036\times0.036$
Grid 4	420 60 30	756000	$0.032\times0.032\times0.032$	$0.064\times0.032\times0.032$
Grid 5	504 72 36	1306368	$0.028\times0.028\times0.028$	$0.056\times0.028\times0.028$

Table 2.1 Details of the meshes adopted in the grid sensitivity study.

With the above numerical set-up, a typical simulation case in a horizontal empty tunnel with propane fire is shown in Fig. 2.17.

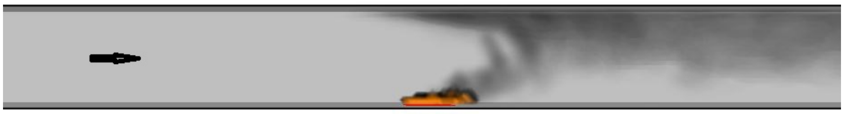

Fig. 2.17 A FDS simulation case with propane fire (Q= 0.57 kW, V=0.33 m/s).

Chapter 3

The control of light gas releases in ventilated tunnels

The release of buoyant harmful gases within enclosed spaces, such as tunnels and corridors, may engender specific industrial and transportation risks. For safety, a simple ventilation strategy of these spaces is to impose a flow, whose velocity is defined as ‘critical’, that confines the front of harmful buoyant gases downwind of the source of emission. Determining the intensity of the critical velocity as a function of the geometrical and dynamical conditions at the source is a basic fluid mechanics problem which has yet to be elucidated; this problem involves issues on the dynamics of non-Boussinesq releases, relating to large differences between the densities of the buoyant and the ambient fluid. We have investigated this problem theoretically, by means of a simple model of a top-hat plume in a crossflow, and experimentally, by means of tests in a reduced-scale ventilated tunnel. Experimental results enlighten i) the existence of two flow regimes, depending on the plume Richardson number at the source Γ_i, one for momentum-driven releases, $\Gamma_i \ll 1$ and one for buoyancy-driven releases, $\Gamma_i \gg 1$; ii) a transition between the two occurring in the range $10^{-2} < \Gamma_i < 1$, and iii) the presence of relevant non-Boussinesq effects only for momentum-driven releases. All these tendencies can be conveniently predicted by the top-hat plume model. Asymptotic solutions of the model reveal interesting behaviours in the limits $\Gamma_i \to 0$, and $\Gamma_i \to \infty$. Notably, solutions for $\Gamma_i \to 0$ helps in clarifying the effect of the source radius and are in good agreement with experimental data. For $\Gamma_i \to \infty$, highly buoyant releases are predicted to behave as point sources of pure buoyancy (independently of their radius and of the density of the emitted fluid). The model predicts also the effect of a varying radius for lazy releases, i.e. $\Gamma_i > 1$. Note however that in this flow regime the model predictions are also very close to those that could be obtained by applying simple scaling approaches for a line source of pure buoyancy. These findings support the adoption of simplified models to simulate buoyancy-driven releases in ventilated confined spaces.

3.1 Introduction

The study of the release of a buoyant fluid within a layer of ambient fluid confined vertically (Jirka and Harleman, 1979) and laterally (Barnett, 1993) is of major interest in industrial and environmental flows (Hunt, 1991). Here we investigate the dynamics of a release of buoyant fluid discharged within a tunnel (Barnett, 1993) and subjected to a forced mechanical ventilation. A peculiar aspect of these flows (see Fig. 3.1) is the appearance of a backlayer of buoyant fluid, which forms after impingement of the release at the confinement surface (or at the ground), and whose front, driven by a pressure gradient, can move forward against the ventilation (depending on its intensity). The focus is on the control of the propagation of this buoyant front by means of the forced tunnel ventilation. This issue is directly linked to industrial and transportation safety problems related to the dispersion of harmful gases in confined spaces. Examples include the leakage of high pressure natural gas from pipelines, the accidental releases of hydrogen or hydrogen sulfide, and the propagation of smoke from fires in road and rail tunnels as well as on underground escalators (Hunt, 1991). This problem has been notably addressed to assess the safety of twin-bore road tunnels (Grant et al., 1998), where the ventilation velocity, which blows all the smoke downstream, allowing the users to evacuate by the entrance, is usually referred to as the ‘critical velocity’. These practical implications are therefore related to a fundamental problem, that of defining the intensity of the ‘critical’ ventilation velocity depending on the geometrical and dynamical conditions at the source. To address this problem we use here theoretical considerations (sect. 3.2) and experimental tests (sect. 3.3). The comparison between theoretical predictions and experimental data finally allows us (sect. 3.4) to identify the role of the key control parameters in the different flow regimes, depending on the conditions imposed at the buoyant source.

3.2 Theory

To begin with, we consider a horizontal and infinitely long tunnel of height H and width W ($\sim H$) within which is placed a source of ‘pure’ (Morton et al., 1956) buoyancy (whose flux is referred here to as B_i): a point source and a line source perpendicular to the tunnel axis. Assuming negligible diffusive effects, and in the limits of the Bousinnesq approximation, the scaling laws for the critical velocity V_c as a function of the governing parameters,

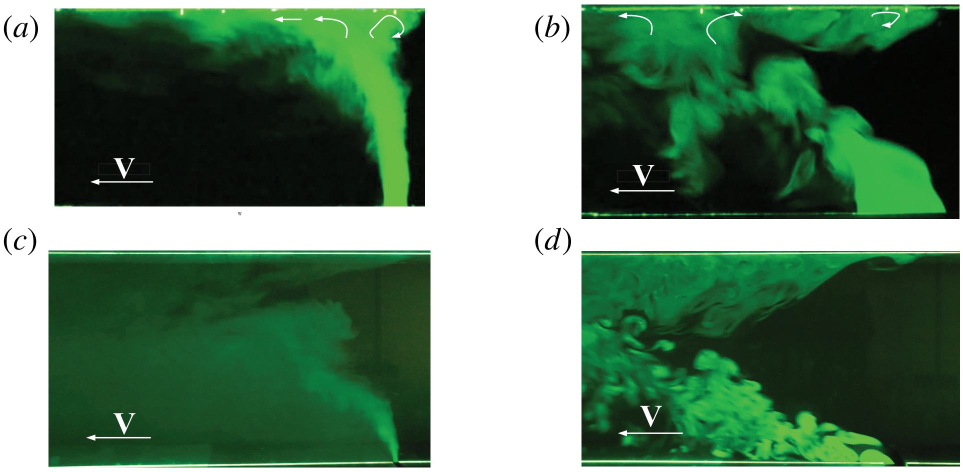

Fig. 3.1 Flow visualisations of the buoyant release submitted to a critical ventilation velocity (from right to left): (a) forced release $\Gamma_i < 1$, circular source, (b)lazy release $\Gamma_i > 1$, circular source, (c) forced release, line source, (d) lazy release, line source.

the buoyancy flux B_i and a characteristic length, can be derived from simple dimensional arguments as:

$$\begin{cases} V_c = f\left(\dfrac{B_i}{W}\right) & \rightarrow \quad V_c \propto \left(\dfrac{B_i}{W}\right)^{1/3} \text{for the line source ,} \\ V_c = f\left(B_i, H\right) & \rightarrow \quad V_c \propto \left(\dfrac{B_i}{H}\right)^{1/3} \text{for the point source.} \end{cases} \tag{3.1}$$

These scaling laws are suitable for sources whose size is much smaller than the tunnel dimensions (H and W) and in case of small density differences between the buoyant and the ambient fluid. In case these conditions do not hold, an exhaustive dimensional analysis has to take into account the size b_i of the source, and the velocity w_i and density ρ_i of the injected fluid, as well as the density of ambient fluid ρ_0 and of the tunnel dimensions. Keeping the assumption of negligible diffusive effects, the critical velocity V_c can be therefore expressed as a function of seven dimensional parameters, namely:

$$V_c = f(w_i, \rho_i, \rho_0, g, b_i, W, H), \tag{3.2}$$

where g is the module of the gravitational acceleration. According to Vashy-Buckingham theorem, the non-dimensional critical velocity is then a function of four non-dimensional parameters:

$$\frac{V_c}{w_i} = f(\Gamma_i, \frac{\rho_i}{\rho_0}, \frac{b_i}{H}, \frac{W}{H}), \tag{3.3}$$

where $\mathit{\Gamma}_i = \dfrac{A}{\alpha_0}\dfrac{\eta_i g b_i}{w_i^2}$ is the plume Richardson number, with $\eta_i = \dfrac{\rho_0 - \rho_i}{\rho_0}$, A a constant equal to $\frac{5}{8}$ for circular antisymmetric plumes and to 1 for 2D planar plumes (van den Bremer and Hunt, 2014) and $\alpha_0 = 0.127$ (a reference value for the 'top-hat' entrainment coefficient for a pure plume). This latter parameter allows for a classification of buoyant releases in momentum-driven forced plumes ($\mathit{\Gamma} < 1$), and buoyancy-driven pure ($\mathit{\Gamma} = 1$) and lazy ($\mathit{\Gamma} > 1$) plumes (Hunt and Kaye, 2005).

To develop a model that allows us to asses the explicit dependence of the non-dimensional critical velocity on the control parameters, as stated in Eq. (3.3), we take here advantage of flow visualizations (details on experimental set-up and techniques will be provided in the next section), showing the morphology of the releases issued from the circular sources and two-dimensional planar sources (whose axis is perpendicular to that of the ventilated tunnel). These preliminary results enlighten relevant differences between the these two typologies of buoyant releases. Those emitted from two-dimensional planar sources exhibit a strong interaction with the flow. The whole air flux of the ventilation flow has to be entrained within the 2D plume. In case of forced momentum-dominated releases this results in a rapid mixing of the buoyant fluid with the ambient air. In case of lazy momentum-driven releases this results instead in a plume bended to ground level, that is the progressively dispersed vertically as it moves downstream the source. In both cases we expect that this strong interaction and mixing with the ventilation flow implies little influence of the source conditions on the critical velocity, and therefore a general scaling of the critical velocity exhibiting a dependence on the buoyancy flux (per unit length) only, as it is for a line source of 'pure' buoyancy (see (3.1)). The releases emitted from the circular sources, whose size is smaller than a third of the tunnel width (i.e. $b_i \leq \frac{W}{3}$), appear instead to behave more like bent-over plume rising to the ceiling. Their centre of mass is progressively displaced downstream as the rising column rises and mixes with the ambient fluid.

Based on these observations, we represent the buoyant fluid releases from the circular source as a 'top hat' plumes, following the well-established approach initiated by Morton et al. (1956), and adopting an entrainment coefficient of the form $\alpha = \alpha_0(\rho/\rho_0)^{1/2}$ (Rooney and Linden, 1996; Van Den Bremer and Hunt, 2010), as is customary when dealing with non-Boussinesq releases. The effect of the tunnel ventilation is taken into account by a drag force exerted by the crossflow on the plume itself. The balance equations for mass, vertical momentum, density difference and horizontal momentum can be written as

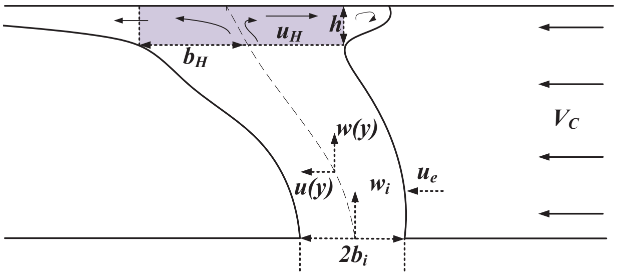

Fig. 3.2 Sketch of the bent-over plume released from a circular source in the ventilated tunnel and of the impingement region (in grey) at the tunnel ceiling.

$$\begin{cases} \dfrac{\mathrm{d}}{\mathrm{dy}}(w\beta^2) = 2\alpha_0\beta w, & \text{(3.4a)} \\ \dfrac{\mathrm{d}}{\mathrm{dy}}(w^2\beta^2) = \widetilde{\eta} g\beta^2, & \text{(3.4b)} \\ \dfrac{\mathrm{d}}{\mathrm{dy}}(\widetilde{\eta} w\beta^2) = 0, & \text{(3.4c)} \\ \dfrac{\mathrm{d}}{\mathrm{dy}}(uw\beta^2) = C_x(V-u)^2\beta/\pi, & \text{(3.4d)} \end{cases}$$

where w and u are its vertical and longitudinal velocities, respectively, V is the ventilation velocity, C_x is a drag coefficient and where $\beta = (\rho/\rho_0)^{1/2}b$ (b is the characteristic plume radius), $\widetilde{\eta} = (\rho_0 - \rho)/\rho$ (ρ is the plume density). The drag in Eq. (3.4d) is proportional to $\sqrt{\rho\rho_0}$, which expresses the weighting role of the local density on the force exerted by the ventilation flow. In the horizontal momentum balance we avoid taking into account terms related to the entrainment of ambient air within the plume, as customary in the formulations of models for buoyant plumes in crossflows (see for example (Devenish et al., 2010) and (Marro et al., 2014)). The reasons for this over-simplification of the horizontal momentum budget will be clarified further on,when discussing the modelling of the critical ventilation condition. Boundary conditions imposed at the source are $b(0) = b_i$, $w(0) = w_i$, $u(0) = 0$, and $\rho(0) = \rho_i$.

If the ventilation velocity is sufficiently low, the plume impinges in the ceiling produce a radial flow characterized by a velocity u_H and a thickness h (Fig. 3.2). A simple model of describing the impingement process is provided by Kaye and Hunt (2007), based on conservation equations on volume and momentum for the turning region:

$$\begin{cases} \pi {b_H}^2 w_H = 2\pi b_H h u_H \\ \pi {b_H}^2 {w_H}^2 = \gamma 2\pi b_H h {u_H}^2 \end{cases} \tag{3.5}$$

where γ is the head-loss coefficient (smaller than 1), a parameter that, in principle, is a function of the dynamical condition of the buoyant plume at the impingement, i.e. $\gamma = \gamma(H)$.

The critical ventilation condition can be computed by assuming that the momentum flux imposed by the ventilation flow balances the longitudinal momentum flux and the pressure force of the buoyant flow at the ceiling, immediately after impingement:

$$\rho_0 {V_c}^2 = \varphi \left[\rho_H {u_H}^2 + \frac{1}{2}(\rho_0 - \rho_H) g h \right] . \tag{3.6}$$

where the parameter φ is a constant that has to be determined experimentally. In the tunnel safety literature (Grant et al., 1998) the critical velocity is generally defined as that preventing the backlayer flow from moving upstream the source or, alternatively, as the minimal ventilation velocity preventing the formation of the backlayer flow. Note that, in accordance with the conditions imposed by (3.5) and (3.6), the latter is the one adopted here.

By solving the system (3.5) we can compute the radial flow variables as $u_H = \frac{1}{\gamma} w_H$ and $h = \frac{\gamma}{2} b_H$, so that (3.6) can be rewritten as:

$$\rho_0 {V_c}^2 = \frac{\varphi}{\gamma^2} \rho_H {w_H}^2 \left(1 + \frac{2\alpha_0 \gamma^3}{5} \frac{\rho_0}{\rho_H} \Gamma_H \right) \tag{3.7}$$

where $\Gamma_H = \dfrac{5}{8\alpha_0} \dfrac{\eta_H g b_H}{w_H^2}$ is the plume Richardson number at the impingement (i.e; at $z = H$). Assuming $\gamma \sim 1$, we obtain an estimate of the term $\frac{2\alpha_0 \gamma^3}{5} \simeq 0.05$, which implies that the pressure term is negligible compared to the momentum term in the r.h.s. of (3.7), both in case of pure and lazy plumes (for which we expect $\Gamma_H \sim 1$) and for forced plume ($\Gamma_H \ll 1$). Equation (3.7) can be approximated as:

$$\rho_0 {V_c}^2 = C^2 \rho_H {w_H}^2 \tag{3.8}$$

that in non-dimesional form gives:

$$\frac{V_c}{w_i} = C \left(\frac{\rho_H}{\rho_0} \right)^{1/2} \frac{w_H}{w_i} \tag{3.9}$$

where $C = \sqrt{\varphi/\gamma^2}$ is a parameter that depends on Γ_H, since $\gamma = \gamma(H)$. The systems of equations (3.4a)−(3.4d) and (3.5) represent a highly simplified model of the dynamics of the buoyant fluid release, of its interaction with the ventilation flow and of its impingement at the tunnel ceiling. The model does not take into account pressure gradients and turbulent fluxes, whose roles are not necessarily negligible when considering the flow developing within a few source radii (Craske and van Reeuwijk, 2015; Ezzamel et al., 2015), as is the case in the present study. Furthermore, the model (3.4a)−(3.4d), as it is conceived, is of course unable to simulate any effect of the flow induced by the side walls, and therefore the influence of the aspect ratio H/W. It is therefore worth remembering that adopting such a model is only motivated by the aim of capturing the main bulk phenomena governing the dynamics of the flow, rather than giving a detailed description of it.

3.2.1 Analytical solution

Following previous authors (Hunt and Kaye, 2005; Michaux and Vauquelin, 2008; Van Den Bremer and Hunt, 2010), we can obtain an analytical solution of the system (3.4a)−(3.4c), based on the solution of a freely propagating plume in an unstratified atmosphere, namely:

$$\begin{cases} \dfrac{\beta}{\beta_i} = \left(\dfrac{\widetilde{\Gamma}}{\widetilde{\Gamma}_i}\right)^{1/2} \left(\dfrac{1-\widetilde{\Gamma}_i}{1-\widetilde{\Gamma}}\right)^{3/10}, \\ \dfrac{w}{w_i} = \left(\dfrac{\widetilde{\Gamma}_i}{\widetilde{\Gamma}}\right)^{1/2} \left(\dfrac{1-\widetilde{\Gamma}}{1-\widetilde{\Gamma}_i}\right)^{1/10}, \\ \dfrac{\widetilde{\eta}}{\widetilde{\eta}_i} = \left(\dfrac{\widetilde{\Gamma}_i}{\widetilde{\Gamma}}\right)^{1/2} \left(\dfrac{1-\widetilde{\Gamma}}{1-\widetilde{\Gamma}_i}\right)^{1/2}, \end{cases} \tag{3.10}$$

where $\widetilde{\Gamma} = \dfrac{5g}{8\alpha_0}\dfrac{\widetilde{\eta}\beta}{w^2}$ is a modified plume Richardson number which changes with height and can be computed solving the system

$$\begin{cases} \dfrac{\mathrm{d}\widetilde{\Gamma}}{\mathrm{d}y} = \dfrac{1}{\Lambda_i}\widetilde{\Gamma}^{1/2}(1-\widetilde{\Gamma})^{13/10} \quad \text{for } \widetilde{\Gamma} < 1, \\ \dfrac{\mathrm{d}\widetilde{\Gamma}}{\mathrm{d}y} = -\dfrac{1}{\Lambda_i}\widetilde{\Gamma}^{1/2}(\widetilde{\Gamma}-1)^{13/10} \quad \text{for } \widetilde{\Gamma} > 1, \end{cases} \tag{3.11}$$

with $\Lambda_i = \frac{\beta_i}{4\alpha_0} \frac{|\widetilde{\Gamma_i} - 1|^{3/10}}{\widetilde{\Gamma_i}^{1/2}}$ is a characteristic length imposed by the conditions at the source. From (3.11) we obtain $\frac{y}{\Lambda_i} = F(\widetilde{\Gamma}) - F(\widetilde{\Gamma_i})$, where the function F is

$$F(X) = \begin{cases} 2X^{1/2} \quad \text{for } X \to 0, \\ \frac{10}{3}[(1-X)^{-3/10} - 1] \quad \text{for } X \to 1^-, \\ \frac{10}{3}(X-1)^{-3/10} \quad \text{for } X \to 1^+, \\ \frac{5}{4}X^{-4/5} \quad \text{for } X \to \infty. \end{cases} \tag{3.12}$$

Note that, based on its definition, i.e. Eq. (3.9), the critical velocity does not depend on the position of the impingement point of the plume at the ceiling. Its evaluation therefore does not require to evaluate the trajectory of the plume centreline as it rises from the source to the ceiling. This means that we can avoid taking into account the role of the horizontal momentum balance Eq. (3.4d), which was therefore presented in a over-simplified formulation. The analytical expression of the critical velocity can therefore be simply obtained, as a first approximation, by substituting relations for w_H and ρ_H, given by (3.10), into Eq. (3.9):

$$\frac{V_c}{w_i} = C \left(\frac{\widetilde{\Gamma_i}}{\widetilde{\Gamma_H}} \right)^{1/2} \left(\frac{1 - \widetilde{\Gamma_H}}{1 - \widetilde{\Gamma_i}} \right)^{1/10} \left[1 + \widetilde{\eta}_i \left(\frac{1 - \widetilde{\Gamma_H}}{1 - \widetilde{\Gamma_i}} \right)^{1/2} \left(\frac{\widetilde{\Gamma_i}}{\widetilde{\Gamma_H}} \right)^{1/2} \right]^{-1/2}, \tag{3.13}$$

with $C = C(\Gamma_H)$.

3.2.2 Asymptotic behaviours

It is instructive to investigate the solutions of the system of equations (2.6) in the limits of highly forced and lazy releases, respectively. The main findings of plume theory (Van Den Bremer and Hunt, 2010) indicate that the lower the value of Γ_i, the larger the distance needed to attain pure plume conditions, i.e. $\Gamma = 1$. Based on this, and given the relatively short distance between source and ceiling, we assume here that highly forced releases, i.e. $\widetilde{\Gamma_i} \to 0$, impinge the ceiling with an identical balance of fluxes, i.e. $\widetilde{\Gamma}(y = H) \to 0$. With this assumption, making use of (3.12), we obtain: $\widetilde{\Gamma} = \left(1 + \frac{2\alpha_0 y}{\beta_i}\right)^2 \widetilde{\Gamma_i}$. Thus, (3.4)-(3.4c) can be approximated as

$$\frac{\beta}{\beta_i} = \frac{w_i}{w} = \frac{\eta_i}{\eta} = 1 + \frac{2\alpha_0 y}{\beta_i}. \tag{3.14}$$

Using (3.14) we can have the solution for (3.9)

$$\frac{V_c}{w_i} = \frac{C_F}{1+\frac{2\alpha_0 H}{b_i}\left(\frac{\rho_0}{\rho_i}\right)^{1/2}}\left(\frac{\left(\frac{\rho_0}{\rho_i}-1\right)}{1+\frac{2\alpha_0 H}{b_i}\left(\frac{\rho_0}{\rho_i}\right)^{1/2}}+1\right)^{-1/2} \tag{3.15}$$

with $C_F = C(\mathit{\Gamma}_H \to 0)$.

In comparison to forced plumes (Van Den Bremer and Hunt, 2010), lazy plumes rapidly attain the condition of a pure plume ($\widetilde{\mathit{\Gamma}} \to 1^+$) as $\widetilde{\mathit{\Gamma}}$ decreases quickly with distance from the source (see also Fig. 3.2*b*). We therefore assume that for $\widetilde{\mathit{\Gamma}}_i > 1$, the release impinges the ceiling in the condition $\widetilde{\mathit{\Gamma}}(y=H) \to 1$. With this assumption, making use of (3.12), we obtain: $\frac{y}{\Lambda_i} = \frac{10}{3}(\widetilde{\mathit{\Gamma}}_y - 1)^{-\frac{3}{10}} - \frac{5}{4}\widetilde{\mathit{\Gamma}}_i^{-\frac{4}{3}}$, which implies that

$$(\widetilde{\mathit{\Gamma}} - 1)^{-\frac{3}{10}}\,\widetilde{\mathit{\Gamma}}_i^{-\frac{1}{5}} = \frac{6\alpha y}{5\beta_i}. \tag{3.16}$$

Thus, (3.4)-(3.4c) can be approximated as

$$\begin{cases} \beta/\beta_i = \dfrac{6\alpha y}{5\beta_i}, \\ w/w_i = \widetilde{\mathit{\Gamma}}_i^{\frac{1}{3}}\left(\dfrac{6\alpha y}{5\beta_i}\right)^{-\frac{1}{3}}, \\ \widetilde{\eta}/\widetilde{\eta}_i = \widetilde{\mathit{\Gamma}}_i^{-\frac{1}{3}}\left(\dfrac{6\alpha y}{5\beta_i}\right)^{-\frac{5}{3}}. \end{cases} \tag{3.17}$$

(3.9) then gives:

$$\frac{V_c}{w_i} = C_L\left(\frac{5}{6\alpha_0}\frac{b_i}{H}\mathit{\Gamma}_i\right)^{1/3} \tag{3.18}$$

with $C_L = C(\mathit{\Gamma}_H \to 1)$.

It is to note that, for $\mathit{\Gamma}_i \to \infty$, expressing $\mathit{\Gamma}_i$ as a function of the buoyancy flux B_i (3.20), both w_i and b_i vanish in (3.18), which therefore can be rewritten in the form of a constant critical Froude number $\widehat{\mathrm{Fr}}_c$, as:

$$\mathit{\Gamma}_i \to \infty \quad V_c\left(\frac{H}{B_i}\right)^{\frac{1}{3}} = \widehat{\mathrm{Fr}}_c \tag{3.19}$$

with $\widehat{\mathrm{Fr}}_c = \left(\frac{25}{48\pi\alpha_0^2}\right)^{\frac{1}{3}} C_L$.

Equation (3.19) expresses that, for highly lazy plumes, the dynamical similarity conditions of the flow are reduced to a one non-dimensional parameter only. In other words, the governing flow parameters in (3.2) (for negligible viscous effects and fixed tunnel geometry) could be simply rewritten as $V_c = f(B_i, H)$, and are therefore identical to those of a point source of pure buoyancy, and exhaustively represented by its flux B_i (without any need to provide information on its radius b_i and density ρ_i), as in 3.1.

In what follows we explore experimentally the dynamics of these buoyant releases by investigating the functional dependence expressed by Eq. (3.3), and discuss reasons of the agreement and disagreement of the experimental data with our theoretical predictions. Our aim is to extend and complete the analysis previously presented by Le Clanche et al. (2014), mainly focusing on buoyancy-dominated releases, and investigate Eq. (3.3) for a wide range of dynamical conditions at the source, spanning from almost pure jets ($\Gamma \ll 1$) to highly lazy plumes ($\Gamma \gg 1$). Our focus will be mainly on the role of Γ_i and on that of the density ratio ρ_i/ρ_0, the key non-dimensional parameter used to evaluate dynamical effects referred to as 'non-Boussinesq' (Ricou and Spalding, 1961; Rooney and Linden, 1996) whose influence has still not been fully elucidated. The comparison between the experimental data and our theoretical predictions (i.e. (3.13), (3.15), (3.18), (3.19)) will help evaluating the reliability of the assumptions on which the model is built and therefore provide further insight about the influence of the parameters governing the dynamics of the flow.

3.3 Experiments

Experiments were performed in a reduced-scale model (Fig. 3.3) of length $L = 8.9\,\mathrm{m}$, width $W = 0.36\,\mathrm{m}$, and variable height, $H = 0.185\,\mathrm{m}$ and $H = 0.36\,\mathrm{m}$. The side walls are made of toughened glass which permit visualisation of the flow. The releases of buoyant fluid are mixtures of air and helium, whose flow rates were controlled independently and measured by two flowmeters. Most of the experiments were performed with circular sources, placed at the centre of the tunnel. Few experiments were also performed using rectangular sources disposed transversely to the tunnel axis, therefore occupying the whole tunnel section. To visualise the flow, the buoyant mixture is seeded with nebulised oil and lit with a laser sheet emitted by a lens installed at the inlet of the tunnel. Note that the mass of oil added to seed the buoyant release is a tiny fraction of the total mass injected at the source and thus does not affect the density of the mixture. The longitudinal ventilation is imposed by a fan at the end of the tunnel. The flow rate within the tunnel is measured by means of a hot-wire anemometer placed within a Venturi tube at the inlet, providing a spatially averaged velocity over the tunnel section in the range $0.11 \leq V_c \leq 1.15\,\mathrm{m\,s^{-1}}$.

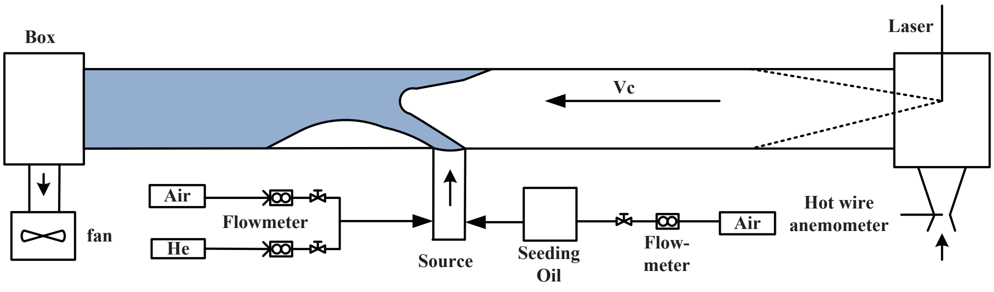

Fig. 3.3 Schematic of the experimental set-up.

The velocity at the source is instead $0.17 \leq w_i \leq 11\,\mathrm{m\,s^{-1}}$, producing a buoyancy flux at the injection (for a circular source):

$$B_i = \pi b_i^2 w_i g \eta_i \tag{3.20}$$

in the range $1 \cdot 10^{-3} \leq B_i \leq 6.3 \cdot 10^{-2}\ \mathrm{m^4\,s^{-3}}$. Experimental results were obtained by varying values of the three control parameters. In case of the circular source, the parameters spanned the ranges $0.004 < \Gamma_i < 24$, $0.25 < \rho_i/\rho_0 < 0.92$, and $0.034 \leq b_i/H \leq 0.270$ (source diameters measured 0.1, 0.075, 0.05, 0.035, 0.025 m). In case of the planar 2D source we have instead $0.6 < \Gamma_i < 13$ (note that the definition of Γ_i for a two-dimensional planar plume differs from that of a circular plume by a factor 5/8) a fixed density ratio $\rho_i/\rho_0 = 0.7$, and $0.014 \leq b_i/H \leq 0.055$ (b_i refers in this case to the source half-length).

Note that results could be produced for a limited combination of the control parameters in these ranges of values. Experimental conditions were constrained by the power of the fan used to produce the longitudinal ventilation, the measurements range of the flow meters, the availability of helium and by the Reynolds number. This latter, defined as $Re_i = \dfrac{2w_i b_i}{\nu}$ (ν is the fluid kinematic viscosity), had to be kept sufficiently high to avoid viscous effects.

Concerning the circular sources, these limitations did not allow us to produce releases with $\Gamma_i > 2$ with 'small' radii (i.e. $b_i/H < 0.15$) and highly-forced ($\Gamma_i < 1$) non-Boussinesq ($\rho_i/\rho_0 < 0.15$) releases with 'large' radii (i.e. $b_i/H > 0.3$). The Reynolds number varied in the range $700 < Re_i < 11100$. Note that Re_i generally decreased with increasing Γ_i, with $2500 < Re_i < 11000$ for $\Gamma_i < 0.5$, $1000 < Re_i < 6000$ for $0.5 < \Gamma_i < 1$ and $700 < Re_i < 2000$ for $\Gamma_i > 1$. In the case of the planar 2D source, we could mainly produce pure and lazy releases, i.e. with $\Gamma_i \geq 1$. The slightly forced releases, i.e. in the range $0.1 \leq \Gamma_i \leq 1$, were produced for the smallest source size ($b_i/H = 0.014$), only. All (pure and lazy) releases exceeded the critical value $Re_{cr} = 600$, indicated by Arya and Jr. Lape (1990) as a threshold ensuring negligible viscous effects on buoyant releases in a crossflow.

The experimental evaluation of the critical velocity by means of flow visualisations is somehow simple, since it solely requires, once the source conditions are fixed, an adjustment to the fan power to assess the position of the backlayer front at the up-wind border of the source. This protocol inevitably involves a number of experimental uncertainties in determining the position of the front. To estimate these uncertainties we performed 20 independent iterations of the same experiment, for a reduced number of experimental conditions. For each of these conditions, the uncertainty was then quantified as half of the difference between the minimum and maximum value of V_c. In the case of a circular source, this never exceeded $\pm 10\%$, which was therefore assumed to be the reference value of the experimental uncertainty. In case of planar 2D source the uncertainty was instead higher and could reach $\pm 15\%$.

To analyse the dependence of V_c/w_i in the parameters given by Eq. (3.3) we performed a different series of experiments. In each of these, we conveniently changed the values of the control parameters at the source, i.e. w_i, b_i, and ρ_i, in order to vary one of the three, i.e. Γ_i, b_i/H, ρ_i/ρ_0, non-dimensional parameters whilst keeping the other two fixed.

3.4 Results

Results for the case of planar 2D sources are presented in Fig. 3.4. Results were produced for three source sizes (i.e. $b_i/H = 0.028, 0.056, 0.111$), a fixed density ratio $\rho_i/\rho_0 = 0.7$ and a plume Richardson number in the range $0.1 < \Gamma_i < 20$. Therefore results concern slightly forced and lazy releases, only. For this reason, as it will be clarified in presenting the results for the circular sources, we did not investigate the influence of the density ratio ρ_i/ρ_0 for these releases (these experiments were actually performed chronologically after those on circular sources). Plotting the non-dimensional critical velocity on the plume Richardson number V_c/w_i (Fig. 3.4a) shows two main features: i) a general dependence of the form $\frac{V_c}{w_i} \propto \Gamma_i^{1/3}$ and ii) differences between the series obtained with different source size which are of the same order of the experimental error. This undetectable influence of the source size b_i/H confirm our preliminary observations about the dynamics of these releases. As previously observed, these are characterised by a strong interaction with the ventilation flow, which is forced to be fully entrained in the buoyant fluid release. More instructive information about the dynamics of the planar 2D releases can be then highlighted by verifying the scaling of the critical velocity predicted by (3.1), i.e. on $(B_i/W)^{1/3}$. As Fig. 3.4b shows, this scaling is verified in the whole range of Γ_i investigated here. All releases, independently of their

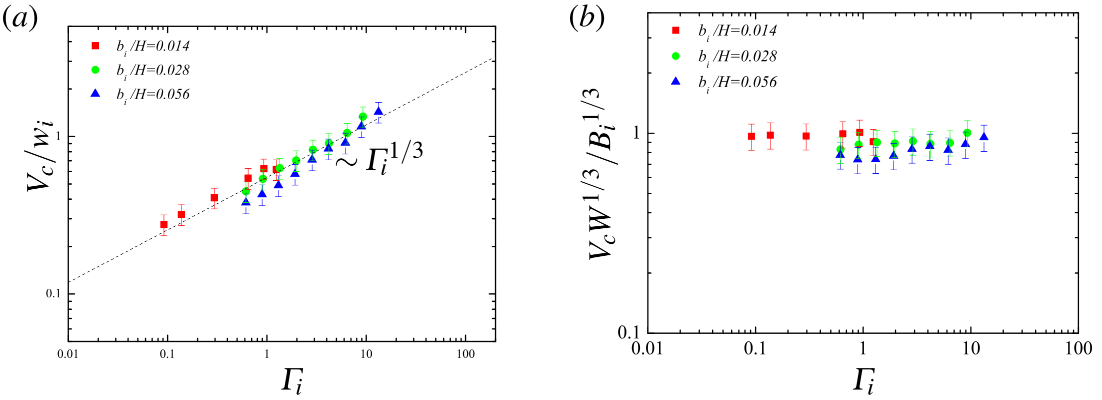

Fig. 3.4 a) $\frac{V_c}{w_i}$ and b) $V_c\left(\frac{W}{B_i}\right)^{\frac{1}{3}}$, as a function of Γ_i for the planar source.

source conditions (b_i and Γ_i) are characterised by a constant Froude number $Fr_W = \dfrac{V_c W^{1/3}}{B_i^{1/3}}$ whose values are of order unity. This proves that these releases behave as a line source of ‘pure’ buoyancy. This can be explained by the fact that, as a consequence of the strong interaction and mixing between the ambient and the buoyant fluid, the dynamics of these releases loose any dependence on the source conditions, that are therefore fully characterised by their buoyancy flux per unit length, only.

Results for the circular source are shown in Fig. 3.5 and 3.6 and are compared to those obtained by Le Clanche et al. (2014) in a reduced-scale model with aspect ratio $H/W = 0.5$, slightly different from that of the reduced model used here, and equipped with different instrumentation. Figure 3.5 shows the dependence of the non-dimensional critical velocity on the Richardson number Γ_i, for varying radii b_i/H and a fixed density ratio $\rho_i/\rho_0 = 0.7$. Figure 3.6 shows the influence of the density ratio ρ_i/ρ_0 on a series of releases with fixed Γ_i, each of which has the same radius b_i/H. Note that to ensure a turbulent release, larger radii had to be adopted for larger Γ_i. As previously mentioned, the constraints of $Re_i > 700$ significantly limited exploration of the effect of a varying radius at large Γ_i, whereas the constraint on highly forced releases was mainly limited by the power of the fan producing the tunnel ventilation.

Experimental results on slightly forced to lazy releases, i.e. $\Gamma_i > 0.1$, agree well with previous data obtained by Le Clanche et al. (2014) and therefore confirm their main findings, namely that the non-dimensional critical velocity i) does not show any clear dependence on the density ratio ρ_i/ρ_0, whereas ii) it clearly exhibits a dependence on the plume Richardson number of the form $\propto \Gamma_i^{1/3}$.

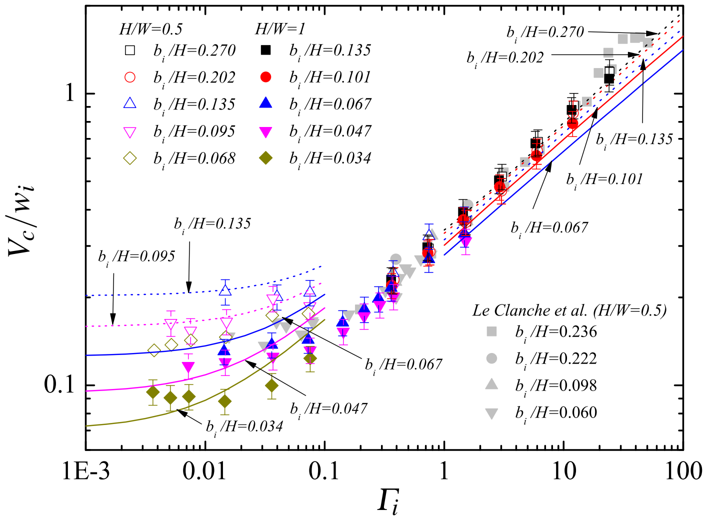

Fig. 3.5 Non-dimensional critical velocity as a function of plume Richardson number Γ_i for a fixed density ratio $\rho_i/\rho_0 = 0.7$. Comparison between experimental data (symbols) obtained for different aspect ratios and analytical solution (Eq. 3.9) (lines).

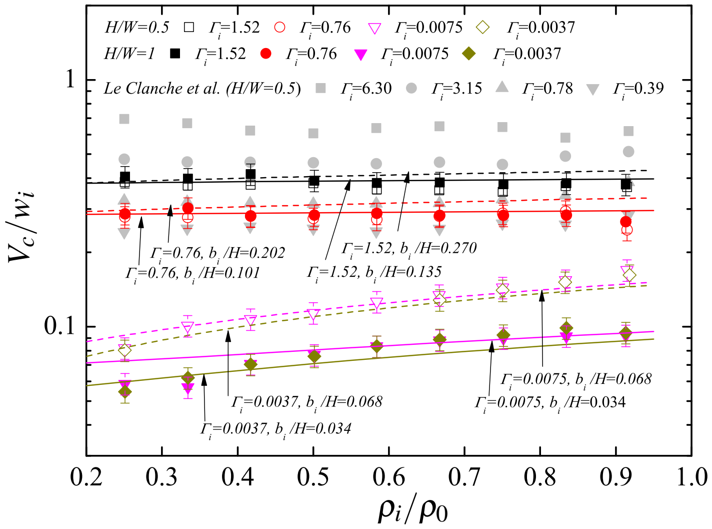

Fig. 3.6 Non-dimensional critical velocity as a function of plume density ratio ρ_i/ρ_0 for different Γ_i. Comparison between experimental data (symbols) obtained for different aspect ratios and analytical solution Eq. (3.9) (lines).

Extending the investigation to $\Gamma_i < 0.1$ reveals further interesting features. Firstly, we observe a weakening of the dependence of the non-dimensional critical velocity on Γ_i as this falls below 0.1. This feature is in agreement with the phenomenological observation of the two distinct flow regimes previously discussed and represented in Fig. 3.1. This weakening of the dependence on Γ_i is also in accordance with the prediction given by the simple dimensional argument, which indicates $V_c/w_i \sim const$ for $\Gamma_i \to 0$ (for any fixed pair b_i/H and ρ_i/ρ_0). The critical velocity exhibits non-negligible dependence on b_i/H as $\Gamma_i \to 0$ (see Fig. 3.5), whereas any influence of b_i/H seems to diminish for $\Gamma_i > 1$. As already mentioned however, the investigation on the role of b_i/H for large Γ_i was limited by the constraints imposed by the experimental set-up. Data on highly forced releases also reveals a clear dependence of the critical velocity on the density ratio, which implies a significant reduction of V_c/w_i as the flow attains non-Boussinesq conditions. It is worth noting that this effect, which could not be observed in the data set of Le Clanche et al. (2014), is only observed in momentum-driven flows and becomes undetectable as $\Gamma_i > 0.1$. This suggests that, as far as the critical velocity is concerned, non-Boussinesq effects have a significant dynamical effect only in the case of forced momentum-driven releases, and become negligible as buoyancy begins to act on the flow dynamics. In other words, the buoyancy driven releases seems to lose information about their source conditions, notably concerning its density. This can be physically interpreted as the effect of the intermittency in the rising of volumes of buoyant fluid and to enhanced mixing in the very near field of the source. The evidence of the negligible influence of the density ratio on V_c for circular releases was actually the reason due to which we avoided performing experiments with varying ρ_i/ρ_0 in case of planar 2D sources (which were performed chronologically after the ones with circular sources).

Further insight into the functional dependence (3.3) is provided by the comparison (also shown in Fig. 3.5 and Fig. 3.6) between the experimental results and those provided by the analytical solution (3.13). It is worth noting that plotting the data in the whole range of Γ_i investigated would require to specify the dependence $C = C(\Gamma_i)$. It is also worth noting that reliable solutions of the plume equations (3.4), spanning over the whole range of Γ_i, would have required include a dependence of the entrainment coefficient on the plume Richardson number (Craske et al., 2017; van Reeuwijk et al., 2016). Taking into account these dependencies would have however precluded an analytical expression for the non-dimensional critical velocity V_c/w_i, and on the relative asymptotic solutions. Plotting the analytical solutions (3.3) results requires therefore to adopt two different values of the parameter C, which are obtained by fitting the data in the momentum-driven regime, i.e. $\Gamma_i < 0.1$, and in the buoyancy-driven regime, i.e. $\Gamma > 1$. This provide a value $C_F = 0.7$ for forced releases and $C_L = 0.44$ for lazy releases, which implicitly implies smaller head-loss coefficient γ for jet-like impinging releases rather than for plume-like releases. This latter feature is consistent with the idea that, for plume-like impinging plumes, the volume of fluid in the impingement region can induce generation of momentum due to its buoyancy, which would results in reducing the whole momentum losses, and therefore increase γ.

Focusing on the results for momentum driven releases, we note a general good agreement between analytical solutions (3.13) and the experimental data. The model is shown to be able to capture well both the dependence on the source diameter b_i/H (see Fig. 3.5) and on the density ratio ρ_i/ρ_0 (see Fig. 3.6). It is worth noting that results were obtained for two different aspect ratios of the tunnel sections, i.e. $H/W = 0.5$ and $H/W = 1$. Both sets of data agree well with the model results, whose predictions do not include any influence of a varying aspect ratio, since it represents the buoyant release as a forced plume in a laterally unbounded co-flow. This good agreement between the experimental data therefore suggests that, in the range of source size investigated here, the dynamics of these releases is almost unaffected by the confinement of the ventilation flow by the lateral tunnel walls.

In case of buoyancy-driven releases ($\mathit{\Gamma} \geq 1$) the model correctly predicts the negligible role of a varying density ratio on the critical velocity (see Fig. 3.6). However, concerning the effect of a varying source diameter (see Fig. 3.5) the comparison between model and experimental data is less instructive because the differences predicted by the model are of the same order of the experimental uncertainty, at least in the range of diameter investigated.

To unveil the role of the source size b_i, as well as of the other length scales involved in the problem, namely the tunnel height H and width W, we therefore represent the data adopting different scalings, and we compare these to the data obtained for the planar 2D sources. Firstly we adopt the scaling suggested by the asymptotic solution (3.19) for $\mathit{\Gamma}_i \to \infty$, the one that would be expected by releases behaving as point sources of ‘pure’ buoyancy. These are presented in Fig. 3.7a where we also plot (dotted line) the value of $\widehat{\mathrm{Fr}}_c$ predicted theoretically. The normalisation of V_c by $(B_i/H)^{1/3}$ is of course not expected to be appropriate for momentum dominated releases, which explains the large scatter of the data for $\mathit{\Gamma} < 0.5$. We can also observe an agreement between the model and the experiments of data obtained for $\mathit{\Gamma} \geq 1$, with data for circular source obtained with $H/W = 0.5$, that lie systematically below data for both circular and planar source obtained for $H/W = 1$. Note however that an effective scaling of the critical velocities induced by buoyancy driven releases, i.e. $\mathit{\Gamma} \geq 1$, can also be achieved by adopting the tunnel width W instead of the height H as a characteristic length. Adopting this scaling (see Fig. 3.7b) the data obtained for $H/W = 0.5$ (and for any source diameter) collapse on the data for $H/W = 1$, including both circular and planar source releases. Physically, this can be simply due to the interaction of the radial outflow after the impingement at the ceiling with the tunnel lateral walls, occurring for buoyancy

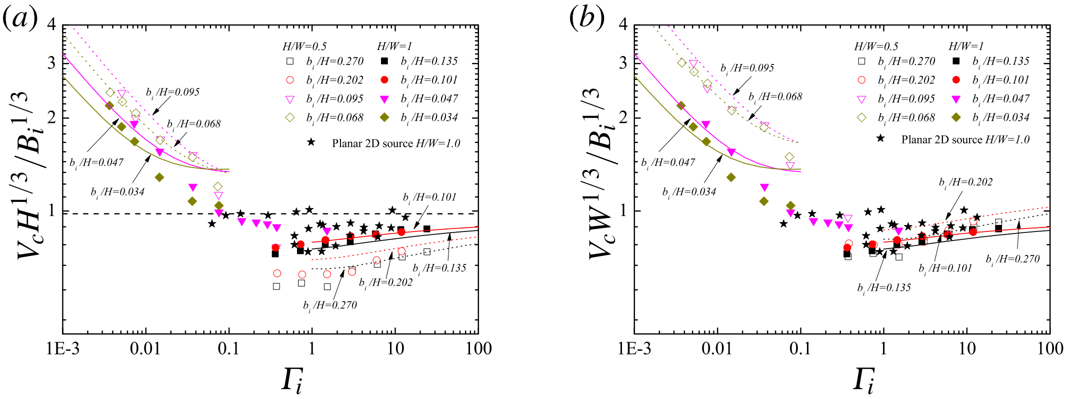

Fig. 3.7 a) $V_c\left(\frac{H}{B_i}\right)^{\frac{1}{3}}$ and b) $V_c\left(\frac{W}{B_i}\right)^{\frac{1}{3}}$, as a function of Γ_i. Also shown in a) is the critical Froude number $\widehat{\mathrm{Fr}}_c = 0.98$ obtained from (3.19) (dashed horizontal line) and analytical solution (Eq. 3.9) (lines).

dominated releases. This is in turn due to two main factors: i) the large source diameters of these releases (which were needed to ensure fully turbulent releases) and ii) the enhanced meandering motion of the buoyant releases as they rise toward the ceiling (Burridge et al., 2017). This meandering motion, which is typical in buoyant plumes, implies fluctuations of the plume centres of mass as it rises and, consequently, enhanced fluctuations of the position of the impingement at the ceiling with respect to the tunnel axis. The interaction of the radial outflow with the lateral walls implies then that the tunnel width W becomes the only relevant length scales, which acts in constrain laterally the buoyancy flux.

This finding suggests that the dynamics of plume-like releases in ventilated tunnels can reliably be modelled as Boussinesq releases (neglecting any effect arising at low values of the ratio ρ_i/ρ_0) of pure buoyancy emitted by a line source, therefore governed by the amount of buoyancy flux per unit width B_i/W whose dynamical effects on the backlayer flow have to be balanced by the ventilation flow V_c, in order to prevent its spreading upwind the source.

3.5 Conclusions

We have investigated the dynamics of a release of buoyant fluid discharged from a circular source placed at the centre of a longitudinally ventilated tunnel. In particular, we focused on the dependence of the so-called ‘critical ventilation velocity’ V_c, that allows the buoyant fluid to be confined downwind of the release point, on varying conditions at the source: the injection velocity w_i, density ρ_i and radius b_i. By assuming negligible diffusive effects, and a tunnel with a fixed aspect ratio (between height and width), the non-dimensional critical velocity V_c/w_i has been shown to depend on three non-dimensional groups: the plume Richardson number Γ_i, the non-dimensional source radius b_i/H and the density ratio ρ_i/ρ_0. This latter parameter is particularly relevant in order to investigate dynamical effects known as non-Boussinesq, i.e. related to large density differences between buoyant and ambient fluid, whose influence is still not fully elucidated in the case of highly buoyant releases, i.e. large Γ_i.

To investigate these dependencies, we performed experiments in a reduced-scale tunnel, where buoyant releases were produced with a mixture of helium and air. Experiments on planar 2D sources (placed perpendicularly to the tunnel axis, so as to occupy the whole tunnel section) show that these releases act a line source of 'pure' buoyancy, which implies that $V_c \propto (B_i/W)^{1/3}$, i.e. that the critical velocity actually depends only on the buoyancy flux at the source B_i per unit width.

Experiments on circular sources have instead shown the following main features:

- the dependence of V_c/w_i on Γ_i reveals the existence of two flow regimes, one for $\Gamma_i \ll 1$ and one for $\Gamma_i \gg 1$;
- the transition between the two regimes occurs in the range $10^{-2} < \Gamma_i < 1$;
- V_c/w_i does not show any dependence on the density ratio as $\Gamma_i > 0.1$, whereas for lower Γ_i the dependence is of the form $(\rho_i/\rho_0)^{1/2}$; and
- in the range of source radii investigated, V_c/w_i seems to be more sensitive to b_i/H for forced releases, i.e. $\Gamma_i < 1$, rather than for lazy releases $\Gamma_i > 1$.

To obtain further insight into the dynamics of releases issued from circular sources we interpreted the experiments by comparing their results to an analytical solution of a simple model of a top-hat plume in a crossflow, which was formulated following the well-established approach by Morton et al. (1956). Despite its simplicity, the model is able to capture main trends identified by the experiments, namely the existence of two flow regimes, depending on Γ_i, and the rise of non-Boussinesq effects for highly forced releases only, $\Gamma_i < 0.1$. In case of momentum driven releases, the model helps in elucidating the role of the source radius on b_i/H and of the density ratio ρ_i/ρ_0 on the flow dynamics. Notably these dependence can be well highlighted by the asymptotic solution in the limits $\Gamma_i \to 0$. According to the asymptotic solution, V_c/w_i is shown to depend on $(\rho_i/\rho_0)^{1/2}$, although it does not fully rescale on it. The good agreement between model and experimental data, collected for two different aspect ratio of the tunnel section, further suggest that the lateral walls do not have an influence on the dynamics of the light-gas release as it rises and impinges at the tunnel ceiling.

For lazy releases, i.e. $\Gamma_i \geq 1$, the model predicts a dependence on source radius b_i and tunnel height H. However, the experimental data for buoyancy driven releases are also in close agreement with the behaviour observed for planar 2D source: a critical velocity depending on the on the buoyancy flux at the source B_i per unit width, only, irrespective of its geometry (planar, circular), its velocity and and its density. This is due to the interaction of the radial outflow produced after the impingement at the lateral walls, which implies that the tunnel width becomes the only relevant length scale influencing the dynamics of the rising back layer flow. The simple scaling $V_c \propto (B_i/W)^{1/3}$ observed experimentally would have two major theoretical implications:

- for pure and lazy releases, the release can be represented as a line sources of ‘pure’ buoyancy, for any source conditions (in terms of density ratio and source geometry); and
- the so-called non-Boussinesq effects have no major influence on the flow dynamics as far as gravitational effects take over those related to inertia.

It is worth noting that, from a practical point of view, both features support the use of simplified mathematical models for the simulation of these flows, and define the ventilation systems for the management and the mitigation of accidental risks related to the releases of toxic and flammable fluids in enclosed spaces.

Chapter 4

Critical velocity in ventilated tunnels in the case of fire plumes and densimetric plumes

We focus on the critical velocity in longitudinally ventilated tunnels and on its dependence on the power of the fire source. In particular we aim at identifying the reason for the appearance of the so-called ‘super-critical’ velocity, a ventilation velocity that becomes independent of the heat release rate when it becomes large. A critical review of existing literature studies allows us to point out possible explanations for this peculiar phenomenon. Among these, we focus here on effects related to heat fluxes (diffusive and radiative) and to the presence of large (compared to the tunnel height) flames. The study is conducted by combining experimental, numerical and theoretical methods. The experiments were performed in a reduced-scale tunnel using densimetric plumes (air/helium mixture and hot air). Numerical simulations were performed with Fire Dynamics Simulator (FDS) and concerned densimetric plumes and fire plumes (propane). These show that the diffusive heat fluxes at the tunnel walls affect only marginally the critical ventilation. Similar conclusions can be drawn for the role of the radiative fluxes. The main phenomenon that alters the flow dynamics and induces the critical velocity to become almost independent on the heat release rate when it becomes large, is the presence of large flames, representing a source of distributed buoyancy within the tunnel and located downwind of the injection of flammable gases. These results also show that plumes arising from small fires can be reliably modelled as buoyant densimetric plumes released at ground level. The dynamics induced by larger fires instead require the modelling of a volumetric source of buoyancy within the tunnel.

4.1 Introduction

Constraining the propagation of hot smoke with a forced ventilation is a key issue for the management of risks related to the occurrence of fires within road and rail tunnels. This goal can be attained with different ventilation systems, adapted to one-way or two-way tunnels. In the case of a one-way tunnel, the basic strategy is to avoid the propagation of the front of the hot smoke upstream of the fire location, in order to allow the users to escape in the opposite direction and the safety services to approach as close as possible to the fire. To obtain this condition it is necessary to impose a 'longitudinal' ventilation velocity that is referred to as 'critical'. The study of the dependence of the smoke propagation on the power of the fire and the intensity of the mechanical ventilation has therefore motivated so far a large number of studies on the field. From a qualitative point of view, these studies generally agree on the fact that the critical velocity increases with the one-third power of the heat release rate (HRR) of the fire and tends to become independent of it as it exceeds a threshold. There are however two main features that have to be clarified and arising from the literature:

- the reasons for this general behaviour have not been fully identified;
- from a quantitative point of view, the literature results show a general poor agreement with one another.

The aim of this paper is to shed light on these aspects using theoretical, experimental and numerical methods. Before providing insight on our methods and results, we begin by presenting some background concepts (4.1.1) that are needed to critically review the existing literature on this subject (4.1.2). Based on this review we then identify the main key questions (4.1.3) that need to be tackled.

4.1.1 Background

A general sketch of the main physical phenomena affecting the dynamics of the flow within a longitudinally ventilated tunnel in case of a fire is presented in Fig. 4.1. A part of the energy flux induced by the presence of the fire is transferred to the surrounding space by radiation, emitted by the flames and the hot smoke. The convective heat fluxes induce in turn a buoyancy flux, generating a thermal plume, that rises and impinges on the ceiling, creating a backlayering flow.

In the simplest representation of this phenomenon, the heat transfer due to radiative fluxes and diffusive fluxes at the tunnel walls are neglected. By further considering that the heat capacity c_p is constant, we can express the buoyancy flux at the source as directly proportional to the HRR, referred to here as Q:

$$B_i = \frac{gQ}{\rho_0 T_0 c_p} \tag{4.1}$$

where ρ_0 and T_0 are reference ambient air density and temperature, respectively and g is the gravitational acceleration. If we also consider that diffusive processes are negligible, we then conclude that the extent l of the backlayering flow depends only on the the buoyancy flux B_i, the ventilation velocity V and the height H and width W of the tunnel, i.e.:

$$l = f(B_i, V, H, W) \tag{4.2}$$

We therefore have a dependence on four independent control parameters having two independent physical dimensions. This leads to a non-dimensional form of Eq. (4.2) of the form:

$$\frac{l}{H} = f(Ri, \frac{W}{H}) \tag{4.3}$$

where $Ri = \frac{B_i}{V^3 H} = \frac{gQ}{\rho_0 T_0 c_p V^3 H}$ is the Richardson number, which expresses a ratio between the buoyancy effects, induced by the presence of a fire, and the inertial effects, associated to the mechanical ventilation of the tunnel. We can then define the critical ventilation velocity $V = V_c$ as the smallest one imposing a zero extent of the back layering flow, i.e. $l = 0$. Then, for a given tunnel aspect ratio W/H, and assuming that relation Eq. (4.3) is a one-to-one function, we have

$$f(Ri_c) = 0 \tag{4.4}$$

i.e. $Ri_c = const$, being $Ri_c = \frac{B_i}{V_c^3 H}$ the critical Richardson number. The dependence of V_c on B_i (and therefore on Q) will be then expressed as:

$$V_c \sim \left(\frac{B_i}{H}\right)^{1/3} \sim \left(\frac{gQ}{\rho_0 T_0 c_p H}\right)^{1/3} \tag{4.5}$$

As we will see in the next paragraph, this functional dependence has been recurrently proposed in literature studies, in order to link the critical ventilation velocity to the heat release rate.

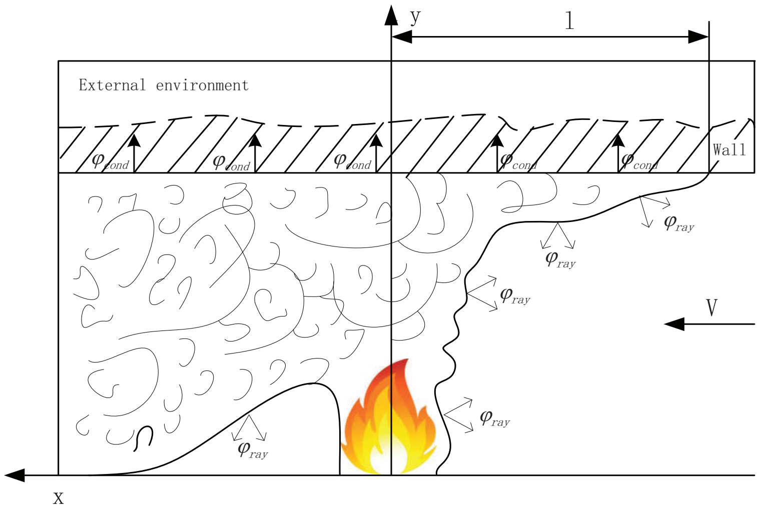
y
l
External environment
φ_{cond}
φ_{cond}
φ_{cond}
φ_{cond}
φ_{cond}
Wall
φ_{ray}
φ_{ray}
φ_{ray}
V
φ_{ray}
φ_{ray}
x

Fig. 4.1 Sketch of smoke movements and heat transfers during a fire occurring in a ventilated tunnel.

4.1.2 Literature review

The first documented experiments in a reduced-scale tunnel were performed by Thomas (1968). Based on his experimental data, he concluded that the formation of the backlayer flow could be prevented by imposing a ventilation velocity scaling on the one-third power of the HRR:

$$V_c = \left(\frac{gQ}{\rho_0 T_0 c_p W} \right)^{1/3} \tag{4.6}$$

which is therefore in the form of relation Eq. (4.5), except for the fact that the width W is used as a characteristic length instead of the height H.

A similar correlation was subsequently proposed by Danziger and Kennedy (1982):

$$V_c = \left(\frac{gQ}{\rho_0 T_f c_p W Fr_c} \right)^{1/3} \tag{4.7}$$

where $T_f = \dfrac{Q}{\rho_0 c_p U_c W H} + T_0$ and $Fr_c = Ri_c^{-1/2} = 4.5$ represents the critical Froude number.

Based on experiments in a reduced scale tunnel and using a propane burner as the heat source, Oka and Atkinson (1995) identified a dependence on the form:

$$\left. \begin{aligned} &V_c^* = K_v (0.12)^{-1/3} (Q^*)^{1/3} \quad \text{for} \quad Q^* < 0.12 \\ &V_c^* = K_v \quad \text{for} \quad Q^* > 0.12 \end{aligned} \right\} \tag{4.8}$$

where $0.22 \leq K_v \leq 0.38$, depending on the source size, shape, location of the fire, and where the non-dimensional heat release rate and critical velocity are defined as $Q^* = \dfrac{Q}{\rho_0 c_p T_0 g^{1/2} H^{5/2}}$, $V_c^* = \dfrac{V_c}{\sqrt{gH}}$. Similarly to Thomas (1968) and Danziger and Kennedy (1982), Oka and Atkinson (1995) identify a one-third power law dependence of form of relation Eq. (4.5). They however argue that this is restricted to small HRR, whereas for larger HRR (and namely for $Q^* > 0.12$) the critical velocity becomes independent of Q^*, reaching a condition referred to as 'super-critical'.

A similar behaviour was also reported by Wu and Bakar (2000) and Li et al. (2010). Wu and Bakar (2000) simulated the fire source by means of a propane gas, placed within a porous bed burner and found that:

$$\left.\begin{aligned} V_c^* &= 0.40(0.20)^{-1/3}(Q^*)^{1/3} \quad \text{for} \quad Q^* < 0.20 \\ V_c^* &= 0.40 \quad \text{for} \quad Q^* > 0.20 \end{aligned}\right\} \tag{4.9}$$

where (differently from Oka and Atkinson (1995)) Q^* and V_c^* are defined using the hydraulic height $\overline{H}$ instead of the tunnel height H as a characteristic length of the tunnel, in order to include eventual variability induced by a varying aspect ratio of the tunnel cross section. In relation Eq. (4.9) the proportionality coefficient and the critical value of the non-dimensional HRR at which the transition between the two regimes occur are different from those given in Eq. (4.8). These differences are likely to be due (at least partially) to the fact that Wu and Bakar (2000) used a water system to cool the external tunnel walls, therefore enhancing the global heat transfers. A further experimental study is that of Li et al. (2010), who performed experiments using propane gas in porous bed burner, and suggested the following relation:

$$\left.\begin{aligned} V_c^* &= 0.81(Q^*)^{1/3} \quad \text{for} \quad Q^* < 0.15 \\ V_c^* &= 0.43 \quad \text{for} \quad Q^* > 0.15 \end{aligned}\right\} \tag{4.10}$$

In Eq. (4.10) the proportionality constant in the one-third power law regime and the critical condition for the transition regime are different from that provided by previous authors. However, the value of V_c^* is very close to that identified by Wu and Bakar (2000).

It is worth noting that a similar behaviour, i.e. the weakening of dependence of the (non-dimensional) critical velocity on the (non-dimensional) HHR, was also observed by Vauquelin (2005) with a completely different experimental set-up, and based on the injection of a mixture of air and helium. To explain this peculiar behaviour, Le Clanche et al. (2014) performed experiments on a similar set-up focusing on the role of the source condition, namely of a varying diameter of the source, and of a eventual role of varying densities of the buoyant release. They suggested that the weakening of the dependence of the critical

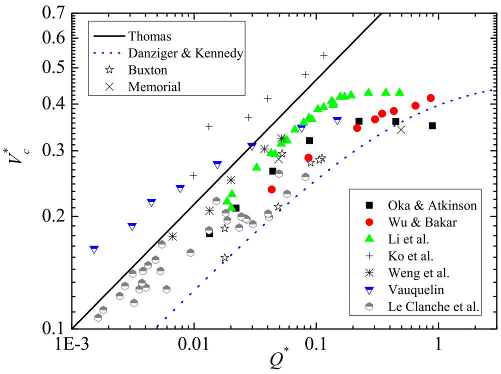

Fig. 4.2 Overview of literature data on the non-dimensional critical velocity as a function of the non-dimensional heat release rate.

velocity on the HRR could be partially attributed to an enhancement of the size of the source for increasing HRR.

Other recent results are those of Ko et al. (2010) and Weng et al. (2015). Ko et al. (2010) used pool fires with three kinds of fossil fuels (methanol, acetone, and n-heptane) and acknowledge a one-third power law dependence of V^* on Q^*, even though with a proportionality coefficient that is greater than the one proposed by Wu and Bakar (2000). Weng et al. (2015) conducted experiment in a reduced-scale tunnel using a methanol pool fire and found:

$$V_c^* = 0.82(Q^*)^{1/3} \tag{4.11}$$

Note that the proportionality coefficient is close to the one identified by Li et al. (2010) for low heat release rates.

An overall picture of the literature data is presented in Fig. 4.2, where we plot the dependence of the non-dimensional critical velocity V_c^* on the non-dimensional heat release rate Q^* (using the tunnel height H as the characteristic length scale in the normalisations). These results include data collected in reduced-scale tests, using different methods to simulate the fire source: densimetric plumes produced with a light gas mixture (Vauquelin (2005)), a propane bed burner (Oka and Atkinson (1995), Wu and Bakar (2000), Li et al. (2010)) and pool fires (Ko et al. (2010), Weng et al. (2015)). In Fig. 4.2 we also include results obtained in large-scale tunnels, namely from the Buxton gallery and the Memorial test programs (Wu and Bakar, 2000).

4.1.3 Open questions

The data presented in Fig. 4.2 are clearly affected by a significant scatter. The experimental uncertainties are certainly relevant, especially for the data collected in large scale tests, but these are unlikely to be the only cause for the high dispersion of the results. We can therefore raise doubt on the effective existence of a one-to-one relation between V_c^* and Q^*. We stress here, that such a dependence would imply three major constraints, i.e. that:

- the heat source can be fully characterised by the buoyancy flux only, and that this flux is proportional to the heat release rate;
- radiative and diffusive effects are negligible;
- the variation of the geometry of the tunnel and of the source has no effect on the critical velocity.

As previously discussed, these three conditions imply a proportionality between V_c and $Q^{1/3}$. This explains the evolution of the data by Megret and Vauquelin (2000) and by Oka and Atkinson (1995) for low values of the heat release rate. A similar tendency can be also identified in the data by Wu and Bakar (2000) and of the real-scale experiments in the Buxton gallery (Bettis et al., 1993), even though the proportionality constant is however different between V_c and $Q^{1/3}$. The variation on the proportionality constant can be due for example to the variability of the tunnel geometry, as well as to variations in the parameters that characterise the heat source, such as its size and form, its position, and to the extension of the flames.

The main aspect that needs however to be discussed is the fading out of the proportionality between V_c and $Q^{1/3}$ for large heat release. This feature led previous authors to identifying a ‘super-critical’ ventilation velocity (Ingason et al., 2015; Wu and Bakar, 2000).

Grant et al. (1998) and Oka and Atkinson (1995) suggest that this behaviour has to be due to a sort of ‘blocking’ of the flow due to the presence of the fire, as the flames are large and attain the ceiling. The mechanism inducing this blocking (and induced by the blocking) has not however been clarified. Wu and Bakar (2000) argue instead that this is caused by the intermittency of the flame. Hwang and Edwards (2005) suggest that the maximum temperature above the fire source plays the key role.

It is evident that the weakening of the dependence of V_c on Q (which is reduced compared to the one-third power identified for low HRR) implies that the similarity conditions of the flow are altered so that Eq. (4.3) does not hold anymore. The key problem is therefore to identify the physical phenomena that are responsible for this breaking of the dynamical similarity. This can be the symptom of physical phenomena arising for large HRR and with negligible role for small HRR, and related to non-dimensional parameters that are not taken into account in Eq. (4.3), due for example to:

- fluid-mechanics effects, induced by large density differences (determined in turn by large temperatures), and known as 'non-Boussinesq effects' (Le Clanche et al., 2014; Rooney and Linden, 1996);
- effects induced by the presence of a growing fire and to heat transfer phenomena.

A first attempt in tackling the first aspect was presented by Le Clanche et al. (2014). In this paper we are instead concerned with the second feature. We aim in particular at focusing on the role of three phenomena that are induced by the enhancement of the heat release rate Q and that have not been so far clarified:

1. the growth of the extension of the flames, i.e. of the volume of the heat source, occurring as Q increases;
2. an increasing role of radiative effects, which implies a reduction between the buoyancy flux at the source and the total thermal energy flux injected in the system;
3. the growing influence of heat losses at the tunnel walls.

4.2 Materials and methods

In order to investigate the three over-mentioned phenomena, we combine different methodologies. Firstly we performed experiments in a reduced scale tunnel simulating the source with a plume of densimetric (helium) and thermal (hot air) plume. This first set of comparison allows us to focus on the role of heat fluxes at the tunnel walls, without involving any effect related to the presence of flames and minimising eventual effects of heat radiation (sect. 5.3.1). These results are subsequently compared to results obtained in experiments using gas-burners. To that purpose, we have developed a simple model to link the conditions of a fire plume to those of an equivalent densimetric plume issuing from an area source (sect. 4.2.2). This allows us to compare the different sets of data and identify analogies and differences between the two kind of releases. To get further insight in this comparison we then turn to numerical simulations of both fire and densimetric plumes in ventilated tunnels (sect. 4.2.3). These allows us also to evaluate the role of radiation, which would be difficult to quantify experimentally.

4.2.1 Experiments with buoyant plumes

We consider a horizontal and infinitely long tunnel within which a buoyant fluid is continuously released. The critical velocity V_c depends on the conditions imposed at the source (density ρ_i, velocity w_i and radius b_i), the fixed tunnel geometry (i.e. the fixed ratio between height H and width W), the density of the ambient fluid ρ_0. Consequently, by further assuming negligible diffusive effects, the critical velocity can be expressed as :

$$V_c = f(w_i, \rho_i, \rho_0, g, b_i, H, c_p, \lambda/e), \tag{4.12}$$

where λ and e are the tunnel wall thermal conductivity and thickness, respectively. According to the Vashy-Buckingham theorem, the non-dimensional critical velocity can be expressed as a function of four non-dimensional parameters:

$$\frac{V_c}{w_i} = f(\Gamma_i, \frac{\rho_i}{\rho_0}, \frac{b_i}{H}, \lambda^*), \tag{4.13}$$

where $\Gamma_i = \dfrac{5}{8\alpha_0}\dfrac{\eta_i g b_i}{w_i^2}$ is the plume Richardson number, with $\eta_i = (\rho_0 - \rho_i)/\rho_0$ and $\alpha_0 = 0.127$ (a reference value for the 'top-hat' entrainment coefficient) and where $\lambda^* = \frac{\lambda}{e\rho_0 c_p w_i}$. The plume Richardson number is a parameter that allows for a classification of buoyant releases (Hunt and Kaye, 2005) into momentum-driven forced plumes ($\Gamma < 1$), and buoyancy-driven lazy ($\Gamma > 1$) plumes (plumes with $\Gamma = 1$ are said to be 'pure'). The parameter λ^* represents instead a ratio between the thermal flux injected within the tunnel through the source and the thermal flux transferred through the tunnel walls, and is therefore a measure of the heat losses of the tunnel (note that its structure is similar to that of the Stanton number, with a diffusive heat exchange coefficient λ/e instead of a convective coefficient).

In order to investigate the functional dependence given by Eq. (4.13) we have performed experiments in a reduced-scale model (Fig. 4.3) of length $L = 9\,\mathrm{m}$, width $W = 0.36\,\mathrm{m}$ and height $H = 0.185\,\mathrm{m}$. The buoyant plumes were obtained by injecting releases of light isothermal gases, given by a mixture of air and helium, and hot air. A longitudinal air flow is created by an extraction fan located at the outlet of the tunnel. The measurement of a spatially averaged ventilation velocity is provided by a hot-wire anemometer placed within a Venturi tube at the inlet.

In the isothermal experiments (Fig. 4.3a), the flow rates of air and helium are controlled and measured independently. A tiny fraction of nebulised oil is added into the mixture and visualization is realized by a lens installed at the inlet of the tunnel. The critical condition is defined by visualising the backlayering flow, and regulating the power of the fan in order to set the front of the backlayering flow at the source position. Five source diameters were used (D_i=2.5, 3.5, 5.0, 7.5, 10.0 cm), with a fixed density ratio 0.7. The Richardson number at the source was in the range $0.004 < \Gamma_i < 24$ (note that to ensure a turbulent release, larger radii had to be adopted for larger Γ_i).

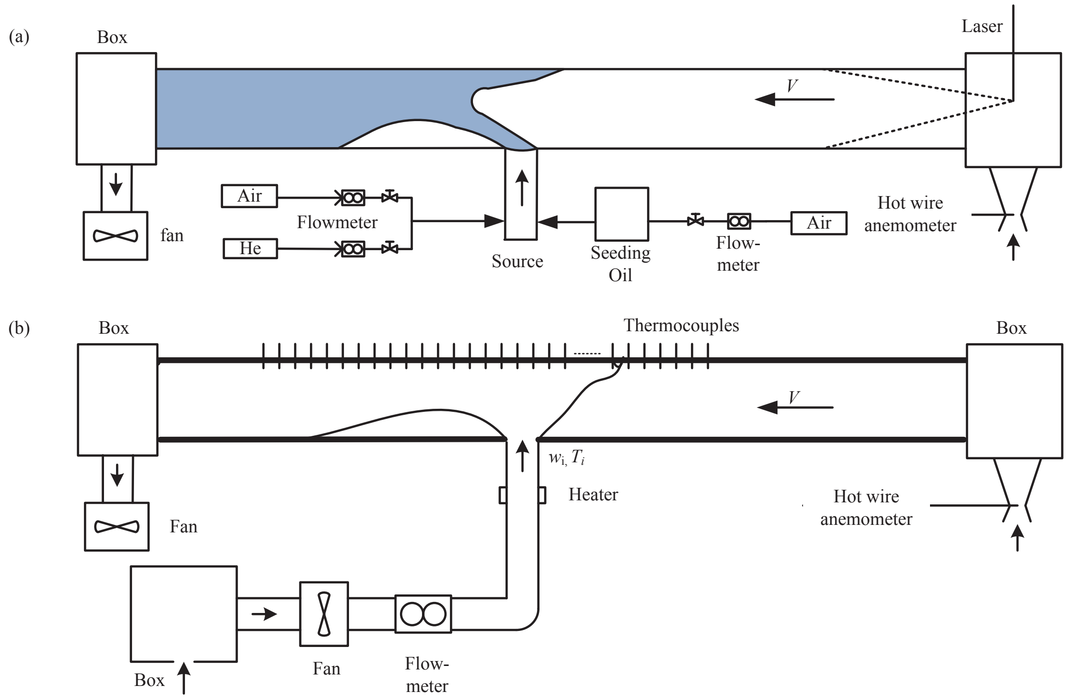
(a)
Box
Laser
V
Air
He
Flowmeter
fan
Source
Seeding
Oil
Flow-
meter
Air
Hot wire
anemometer
(b)
Box
Thermocouples
Box
V
w_i, T_i
Heater
Hot wire
anemometer
Fan
Box
Fan
Flow-
meter

Fig. 4.3 Schematic of the experimental set-up for (a) the ‘isothermal model’ and (b) the ‘thermal model’.

In the thermal experiments, heat release rates between 700 W and 10 kW were produced using a fan and an electric heater, controlled and regulated in temperature by a PID controller. The ceiling (through which most of the heat transfer occurs) is made of plaster with a thermal conductivity $\lambda = 0.16\ \mathrm{W}{\cdot}m^{-1}.^{K-1}$ and thickness $e = 1.8$ cm. The longitudinal extension of the backlayer flow l was estimated using K-type thermocouples measuring air temperature. These were installed on the tunnel axis at the ceiling level and 2 cm apart. The source of the diameter is kept equal to D_i=10 cm. An exhaustive description of the experimental protocol and of the measurements techniques used in these experiments is provided in Salizzoni et al. (2017).

In both kind of experiments the uncertainties were estimated by performing the same experiment 20 times for a reduced number of experimental conditions. For each of these conditions, the uncertainty was then quantified as half of the difference between the minimum and maximum value of V_c. This never exceeded $\pm 10\%$, which was therefore assumed to be the reference value of the experimental uncertainty.

Name	Propane	Methanol	Acetone	N-heptane
Chemical formula	C_3H_8	CH_2OH	C_3H_6O	C_7H_{16}
Enthalpy (MJ/kg)	46.34	20.0	25.8	44.6
$\Delta\ T_i$ (°C)	2002	2125	1781	2000

Table 4.1 Enthalpy of combustion for fossil fuels and relative temperature rise predicted by the model (neglecting radiative heat losses).

4.2.2 A model for fire plumes

In order to model a fire plume as a generic densimetric plume issuing from a ground level circular source of given diameter D_i, we have to compute two physical parameters: the temperature T_i (and therefore the density ρ_i) and the velocity w_i at the source. To that purpose we consider that the presence of a fire implies the full combustion of a generic fossil fuel $C_xH_yO_z$, so that:

$$C_xH_yO_z + \frac{1}{2}(2x + \frac{y}{2} - z)O_2 \rightarrow xCO_2 + \frac{y}{2}H_2O \tag{4.14}$$

By assuming that the HRR is known, we can then compute the mass flow rate of fuel at the source as well as the temperature rise $\Delta T_i = T_i - T_0$ from the enthalpy of combustion ΔH (values for the different fuels are given in Table 4.1).

The mass of fossil fuel is then computed as $\dot{m}_{fuel} = Q/\Delta H$, whereas the mass of air (composed of 20% O_2 and 80% N_2) needed for the full combustion is:

$$\dot{m}_{air} = \frac{5(4x + y - 2z)\dot{m}_{fuel}}{4M_{fuel}}M_{air} \tag{4.15}$$

where M_{fuel} and M_{air} are the molecular weights of the fuel and of air, respectively. The temperature rise of the hot gases is:

$$\Delta T_i = \frac{Q}{c_{pm}(\dot{m}_{fuel} + \dot{m}_{air})} \tag{4.16}$$

where c_{pm} is the specific heat of the mixtures of CO_2, H_2O and N_2 produced by the combustion process, and computed as:

$$c_{pm} = \frac{xM_{co_2}C_{pco_2} + y/2M_{H_2O}C_{pH_2O} + (4x + y - 2z)M_{N_2}C_{pN_2}}{xM_{co_2} + y/2M_{H_2O} + (4x + y - 2z)M_{N_2}} \tag{4.17}$$

Making use of the ideal gas law, the density of the mixture is then:

$$\rho_i = \frac{P_0 M_i}{R T_i} \tag{4.18}$$

where $P_0 = 10^5$ Pa is a reference ambient pressure, $R = 8.31$ is the universal gas constant, and M_i is the molar mass of the hot gases, computed as:

$$M_i = \frac{x M_{co_2} + y/2 M_{H_2O} + (4x + y - 2z) M_{N_2}}{x + y/2 + 4x + y - 2z} \tag{4.19}$$

Finally, the velocity at the source w_i can be estimated as:

$$w_i = \frac{\dot{m}_{fuel} + \dot{m}_{air}}{\rho_i A} \tag{4.20}$$

where A is a planar surface area of fire source. Knowing the source size D_i, its density ρ_i, and the ejection velocity w_i, we are then able to associate a plume Richardson number Γ_i for the different plumes arising from the fire, for varying HRR.

In Table 4.1 are reported the temperature rises provided by the model for different type of fuels. Note that these results refer to the case of full combustion and negligible heat losses. It is worth noting that Eq. (4.16) provides almost the same temperature of the hot gases T_i (around 2000 K) for any type of fuel, regardless of the HRR.

4.2.3 Numerical simulations

Numerical simulations were carried out with Fire Dynamics Simulator (FDS) 6.3, solving a low-Mach number formulation of the Navier Stokes equations adopting a Large Eddy Simulation (LES) approach with a Deardorff subgrid closure model. The tunnel aspect ratio $H/W = 1/2$ is the same as that of the reduced scale model used in this study and of tunnel C in Wu and Bakar (2000), whose results will be used as a reference for the simulation of fire plumes (Fig. 4.4). The length of the numerical tunnel is however reduced compared to that of these two others tunnels, and equal to $24H$. We performed two kind of simulations: with plumes generated by the injection of propane and with plumes generated by the injection of an active scalar (temperature). In both cases the source was a square, placed at a distance of $18H$ from the inlet of the tunnel. The power of the heat release rate ranged from 1 to 30 kW. In the fire plumes simulations, the fraction of propane converted into smoke particulate was set equal to 10% . In the hot-air plume simulations the temperature at the source was set equal to 1300 K.

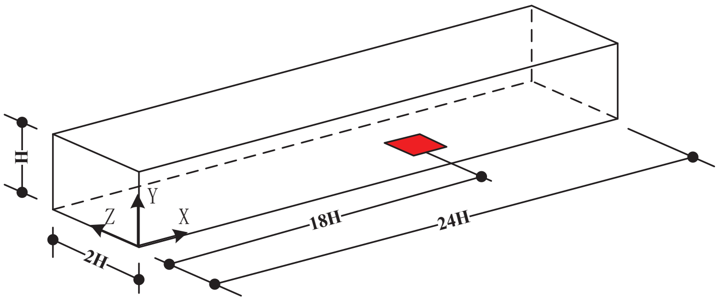

Fig. 4.4 Tunnel geometry of numerical model.

The tunnel walls are 5 cm thick, with a density of 2000 $\mathrm{kg/m^3}$, a specific heat of 0.88 $\mathrm{kJ/(kg\ K)}$ and a conductivity equal to 1.2 $\mathrm{W/(m\ K)}$. Temperature sensors were set 2 cm below the ceiling from 0.5 m upstream the fire source to 0.5 m downstream of it. To estimate the position of the front of the backlayering flow we analysed the longitudinal profile of mean temperature. Each simulation lasted 60 s. The flow required approximately 30 s to reach a steady state (statistically). Therefore the position of the backlayer flow was obtained by averaging the velocity field between 30 s and 60 s.

According to McGrattan et al. (2008) the mesh size close to the fire source has to be estimated depending on a characteristic fire diameter defined as:

$$D^* = \left(\frac{Q}{\rho_0 c_p T_0 \sqrt{g}} \right)^{\frac{2}{5}} \tag{4.21}$$

whose ratio on the grid size Δx values have to be in the range $4 \leq D^*/\Delta x \leq 16$. For a HRR of about 3 kW, D^* is approximately 0.09 m, and therefore $\Delta x \simeq 0.01$ m.

To save computing time, we used an unevenly distributed grid, obtained by stretching the mesh along the x-direction. The tunnel is divided into three sub-domains: the domain close to the inlet is referred to as the ‘Left Domain’, the domain within which is placed the heat source is the ‘Middle Domain’, and that close to the outlet is the ‘Right Domain’. The lengths for the three domains are 4 m, 1 m and 1 m, respectively. In the Middle Domain the grid is twice as fine as the one in the other two domains.

Before performing the numerical experiments we carried out a grid sensitivity study, to evaluate the dependence of our numerical solution on the resolution of the mesh. The characteristics of the different grids tested are listed in Table 4.2. In order to enlighten the dependence of the numerical solution on the grid refinement we focus here on longitudinal profiles of the mean and the standard deviation of the temperature registered at just below the ceiling (at a distance of approximately $0.1H$). Based on these results we adopted Grid 4

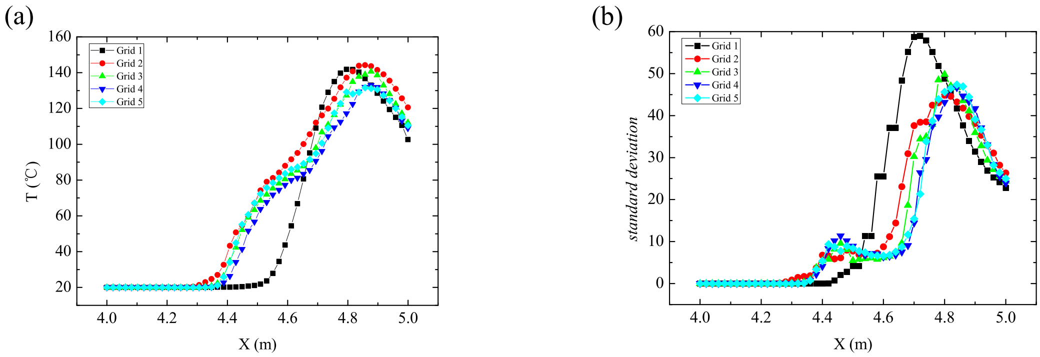

Fig. 4.5 Longitudinal profiles of the mean and of the standard deviation of the temperature along the tunnel ceiling for the five girds tested (See Table 2).

as the reference grid for our numerical study, made up of 756000 cells. Note that Eq. (5.14) implies a higher mesh resolution for smaller fires. In the present study the smallest fire was 0.20 kW, which makes $D^*/\Delta x = 4$, i.e. within the recommended range.

Test	Number of cells X Y Z	Total cells	Cells size in the Middle domain (as a fraction of H)	Cells size in the Right and Left Domains (as a fraction of H)
Grid 1	300 25 12	90000	0.08×0.08×0.08	0.08×0.08×0.08
Grid 2	350 50 25	437500	0.04×0.04×0.04	0.08×0.04×0.04
Grid 3	378 54 27	551124	0.036×0.036×0.036	0.072×0.036×0.036
Grid 4	420 60 30	756000	0.032×0.032×0.032	0.064×0.032×0.032
Grid 5	504 72 36	1306368	0.028×0.028×0.028	0.056×0.028×0.028

Table 4.2 Details of the meshes adopted in the grid sensitivity study.

4.3 Results

In the analysis of the results we proceed as follows. Firstly, we examine results relative to densimetric air-helium plumes, for varying source conditions, and we compare these to those with hot-air plumes, to enlighten the role of the heat losses at the tunnel walls (sect 3.1). These data are consequently compared to literature data on fire plumes arising from propane burner and methanol pools (sect 3.2). To further analyse the analogies and differences between the two set of data we finally turn to numerical simulations (sect 3.2), that also allows us to evidence the role of radiative fluxes (sect 3.3).

4.3.1 Densimetric plumes: experiments and numerical simulations

As a first step, we focus on the experiments with densimetric plumes. A previous study by Le Clanche et al. (2014) already investigated the functional dependence given by Eq. (4.13),

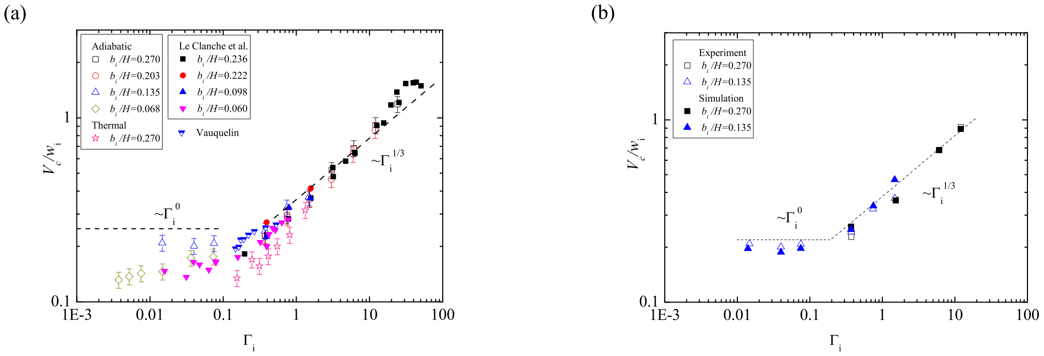

Fig. 4.6 Non-dimensional critical velocity V_c/w_i as a function of the plume Richardson number Γ_i. (a) experimental results comparison between our results (hollow points) and data from Le Clanche et al. (2014) (solid points); (b) comparison between experimental and numerical results.

in the case of $\lambda^* = 0$, i.e. $\frac{V_c}{w_i} = f(\Gamma_i, \frac{\rho_i}{\rho_0}, \frac{b_i}{H})$. Focusing on slightly forced and lazy releases, i.e. $\Gamma_i > 0.1$, they showed that the variations of the radius and of the density ratio have a slight influence on the non-dimensional critical velocity. Among the three non-dimensional parameters, Γ_i is therefore the one having the largest influence on V_c/w_i. The non-dimensional critical velocity V_c/w_i shows a dependence of the form $\Gamma_i^{1/3}$, which in dimensional form implies a dependence of the form $V_c \sim B_i^{1/3}$. According to these results, for a fixed tunnel and source geometry, the dependence of V_c on the HRR has therefore to follow a one-third power law. As discussed by Le Clanche et al. (2014), a plausible explanation for a different behaviour, such as that shown by the data by Vauquelin (2005), could be related to a source size that increases for increasing HRR.

In the present study we have further explored this, performing experiments also for highly forced releases ($\Gamma \ll 1$) and extending our investigation on the role of the parameter λ^*, i.e. on the functional dependence

$$\frac{V_c}{w_i} = f(\Gamma_i, \lambda^*) \tag{4.22}$$

Results on both air-helium plumes and hot air plumes are shown in Fig. 4.6 (a) and are compared to those obtained by Le Clanche et al. (2014) and by Vauquelin (2005). Concerning the air-helium plumes experiments, the new set of data for $\Gamma_i > 0.1$ are in close agreement with those by Le Clanche et al. (2014), and exhibit a dependence of the form $\propto \Gamma_i^{1/3}$. For $\Gamma_i < 0.1$, we observe a weakening of the dependence of the non-dimensional critical velocity for low values of Γ_i. As this falls below 0.1, and the buoyancy fluxes becomes negligible on the flow dynamics, the non-dimensional critical velocity tends to a constant, i.e. $V_c/w_i \sim const$. We can therefore identify two different regimes, for low and large Γ_i, with a transition region of limited extent, roughly in the range $0.1 \leq \Gamma_i \leq 0.5$. For releases $\Gamma_i \leq 0.1$, which therefore are momentum-dominated, we would therefore expect a dependence of V_c on the HRR that would be different than a one-third power law on the HRR. In this respect, it is interesting to note that all data from the experiments by Vauquelin (2005) lay in the transition region, between forced and lazy releases. These source conditions provide then a further explanation of the fact that these data do not show a clear dependence of the form $V_c \sim Q^{1/3}$.

Similar experiments have been conducted by injecting hot air instead of helium and therefore involving thermal effects, i.e. characterised by $\lambda^* \neq 0$. In these thermal plumes experiments the range of the source conditions were limited to $0.2 \leq \Gamma_i \leq 2$. All data collected in the hot-air plumes experiments, for which $\lambda^* \neq 0$, indicate that the non-dimensional critical velocity is reduced compared to the cases in which $\lambda^* = 0$. The differences between the two set of data, i.e. $\lambda^* \neq 0$ and $\lambda^* = 0$ are slightly larger than the experimental uncertainty and show a clear influence of the thermal losses in reducing the magnitude of the non-dimensional critical velocity.

In Fig. 4.6b we compare the numerical results to the predictions provided by the numerical simulations. In the numerical model tunnel, we test sources of different sizes and with the density ratio of the experiments ($\frac{\rho_i}{\rho_0} = 0.7$). The radiative solver is turned off and the walls are set adiabatic. The results show that the numerical results predict accurately the critical velocity and the existence of two flow regimes, for forced plume ($\Gamma_i \rightarrow 0$), $V_c/w_i \propto const.$ and for lazy releases ($\Gamma_i > 1$), $V_c/w_i \propto \Gamma_i^{1/3}$.

4.3.2 Comparison between densimetric plumes and fire plumes

Once identified the dependence of the non-dimensional critical velocity as a function of the source conditions for densimetric plumes, we aim at finding out how, and to what extent, this dependence is modified by the presence of a distributed source of buoyancy, such as a flame. The comparison is performed by means of the model presented in Sect. 2.2, representing the fire plumes as densimetric plumes induced by a localised (at ground level) source of buoyancy. Results of the model, applied to two sets of literature data, are presented in Table 4.3. In evaluating the velocity w_i, the temperature T_i (and the relative ρ_i) we consider two cases: i) that of negligible radiative fluxes, implying that the whole HRR is converted into a convective flux (and therefore buoyancy); ii) that of a radiative flux whose intensity is equal to 30 % of the HRR. It is worth noting that, in both cases, the model predicts a plume characterised by a decreasing Γ_i for increasing HRR. This means that, according to the model, the buoyant releases induced by a fire correspond to plumes that become more forced (i.e. momentum-driven) for increasing HRR. A comparison between our results on

					T_i=1693(K)		T_i=2293(K)	
	Type	Fuel	D_i (m)	$\dot{Q}$ (kW)	w_i (m/s)	Γ_i	w_i (m/s)	Γ_i
Wu &Bakar	Burner	Propane	0.1	1.5	0.31	21.5	0.42	12.3
				3.0	0.63	5.38	0.85	3.07
				7.5	1.57	0.86	2.13	0.49
				10.5	2.20	0.44	2.99	0.25
				12.0	2.51	0.34	3.41	0.19
				15.0	3.14	0.22	4.27	0.12
				22.5	4.71	0.09	6.40	0.05
				30.0	6.28	0.05	8.54	0.03
Weng et al.	Pool fire	Methanol	0.08	1.59	0.44	8.21	0.60	4.68
			0.10	3.19	0.57	6.22	0.77	3.55
			0.12	4.78	0.59	6.89	0.80	3.94
			0.15	8.97	0.71	5.98	0.96	3.41
			0.17	12.4	0.73	6.44	1.00	3.68

Table 4.3 Plume parameters for propane and pool fire for using the model presented in Sect. 4.2.2, assuming heat losses by radiation equal to the 30% of the HRR ($\Delta T = T_i - T_0 = 1400$ K) and no heat losses ($\Delta T = T_i - T_0 = 2000$ K).

densimetric plumes and results of our model applied to literature data on fire plumes in tunnels is presented in Fig. 4.7a, taking into account the effects of radiation, and in Fig. 4.7b, neglecting the role of radiation.

The values V_c/w_i and Γ_i depend on the temperature rise, but the general trend remains unchanged. We observe a good agreement between model and densimetric plumes for most data points and for both temperature rise, i.e. ΔT_i is 1400 K and 2000 K. Discrepancies can be observed for the lowest value of Γ_i, corresponding to releases with higher HRR. At low HRR, V_c is proportional to the one-third power of Q, which implies that V_c/w_i is $\propto \Gamma_i^{1/3}$. For larger values of HRR in the experiments of Oka and Atkinson (1995),Wu and Bakar (2000) and Li et al. (2010), V_c tends to become a constant independent of Q. This implies a dependence of V_c/w_i that differs from a one-third power and becomes proportional to the square root of Γ_i. The numbers of data point following this dependence actually depends on the temperature rise, and decrease for decreasing ΔT_i. In any case, the data corresponding to the conditions of a ‘super-critical velocity’ show a dependence on the source Richardson number that is markedly different from that of densimetric plumes. This means that for the higher HRR fires, the behaviour of the buoyant release can not be assimilated to that of a densimetric plume emitted by a ground-level source.

To further enlighten the difference between a densimetric plume and a fire plume, we show in Fig. 4.8 the dependence of the critical velocity induced by these two different types of releases for identical values of the HRR. The reference case study is given by the experiments of Wu and Bakar (2000). The general behavior of the dependence of V_c as a function of the HRR is well reproduced by our numerical simulations. The numerical results tend to slightly overestimate the experimental data for the larger values of HRR. As already enlightened by previous authors (e.g. Li et al. (2010)), this kind of discrepancies is likely to be due to the role of heat losses at the tunnel wall. Their intensity in the case of Wu and Bakar (2000) was certainly amplified by the use of water cooling systems on the external tunnel walls during the experiments. This can justify the lower values of V_c observed in the experiments, when compared to our numerical simulations, as well as to similar simulations performed by other authors (e.g. Van Maele and Merci (2008)).

Results in Fig. 4.8 clearly show that, for low HRR, the values of the critical velocity V_c obtained for propane fires and densimetric plumes are in close agreement (points denoted as 'a', 'b' and 'c') and follow the same trend, i.e. a dependence on $Q^{1/3}$ (Fig. 4.8 a) in dimensional form and on $\Gamma_i^{1/3}$ in non-dimensional form (Fig. 4.8b). For larger values of the HRR, which would correspond to highly forced, momentum-driven, plumes, characterised by $\Gamma_i < 0.1$ (Fig. 4.8b), the behavior of the fire plumes and densimetric plumes differ more and more. The excess of momentum imposed in the densimetric plumes leads to non-dimensional velocities that tend to a constant (Fig. 4.8b), implying dimensional values of V_c that are larger than those given by a one-third power law (Fig. 4.8a). In the case of propane fires, we instead observe the opposite behaviour, characterised by the well acknowledged super-critical velocity, i.e. independent of Q. As shown in Fig. 4.9, this condition takes place as the size of the flames becomes 'large', i.e. attains and exceeds the height of the tunnel (Fig. 4.9d). In this case, the buoyancy flux is no longer emitted by a localised ground level source but from a volume distributed source extending downstream the location where the propane is actually injected. This displacement of the fire source implies then a reduction of the ventilation velocity needed to prevent the backlayer flow to move upstream of the position of the fire, and induce the critical velocity to become less and less sensitive to increase in the HRR, so that V_c tends to a constant.

4.3.3 The role of radiation

As shown in Fig. 4.10, the radiative fraction, i.e. the percentage of energy transferred from the fire as radiation on the total HRR (as estimated by the FDS simulations), tends to increase for increasing Q, from a minimal 30 % for low HRR to values attaining 50 % for large HRR. Despite this, the effects on the V_c are small. For low values of HRR, with an amount of 30 % of radiative losses, the values of V_c is altered by approximately 10 %. For large values of HRR, despite a 50 % reduction of the convective fluxes, we observe no significant difference

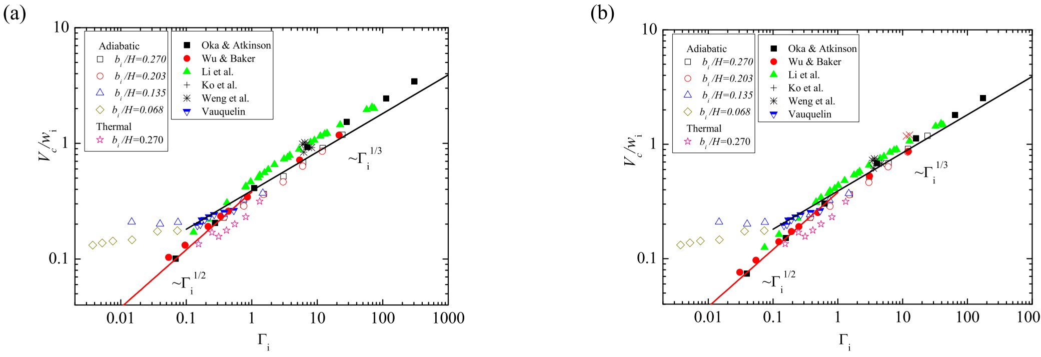

Fig. 4.7 Non-dimensional critical velocity as a function of Γ_i for ΔT_i equal to (a) 1400 K and (b) 2000 K.

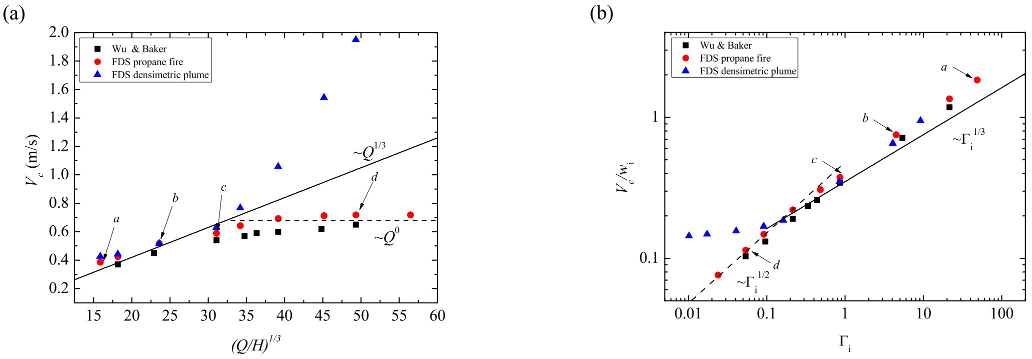

Fig. 4.8 Comparison of critical velocity between numerical simulation and experiment in Wu and Bakar (2000), Γ_i is obtained assumeing a temperature rise $\Delta T_i = 1400$ K (assuming heat losses by radiation equal to 30 % of the HRR). Temperature field and fire of a, b, c, d are shown in Fig. 4.9.

between the cases with and without radiation. This feature is actually in agreement with the general independence of V_c on variations in Q. The role of the radiative fluxes is then only to allow the super-critical velocity to be reached for a lower HRR.

4.4 Conclusion

In this study, we have investigated the origin of the so-called super-critical velocity, arising for large fires in case of longitudinally ventilated tunnel. Our investigation is focused on the influence of physical phenomena that are related to the presence of fire with high temperatures and large flames, i.e. of same order as the tunnel height. To that purpose, we have combined small-scale experiments on densimetric plumes, produced by the injection of light gases and hot air in a reduced scale tunnel, a simple theoretical model to represent fire plumes as

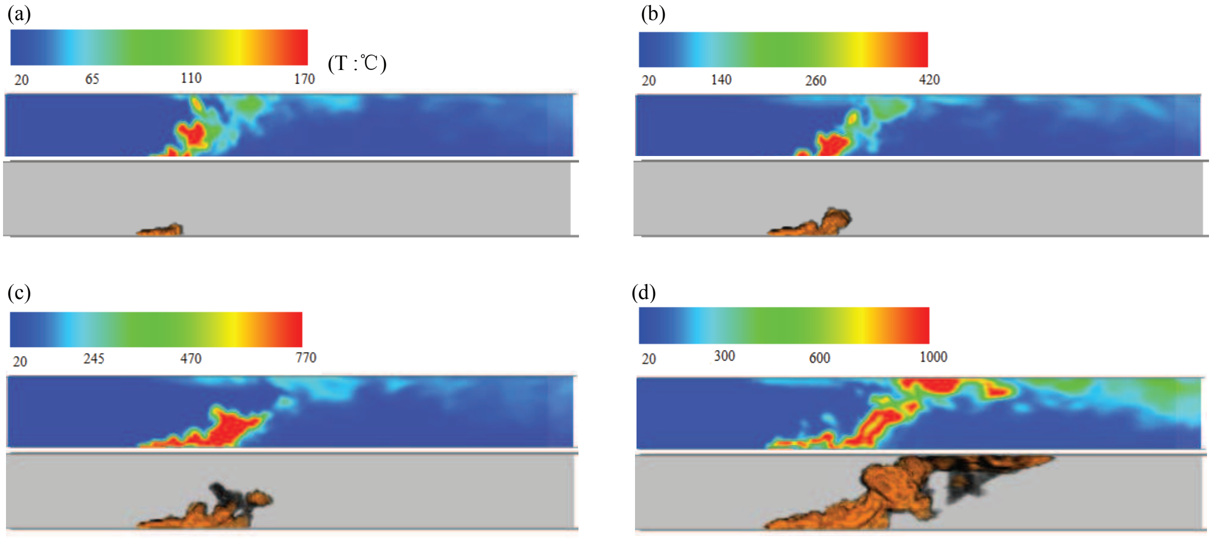

Fig. 4.9 FDS simulations of propane fires. Spatial distribution of temperature and flames ($x-z$ plane at $y = W/2$) for different HRR: 1.0, 3.3, 7.5 and 30 kW.

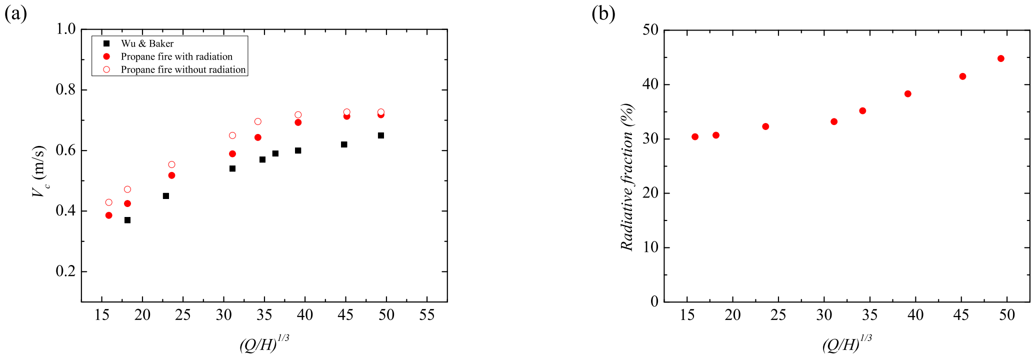

Fig. 4.10 Influence of radiation on critical velocity, (a) critical velocity at different HRR and (b) radiative fraction.

densimetric plumes, and numerical simulations with the code FDS. The results show the main following features:

- The role of heat losses at the tunnel walls can induce a slight reduction in the critical velocity. In the small scale experiments this influence could be evidenced by comparing results for hot-air and light gas(helium and air mixture) plumes. The difference is however slightly larger than the experimental uncertainty. Therefore, heat losses due to diffusive heat fluxes cannot justify the appearance of a super-critical velocity.
- For 'low' HRRs, the critical velocity needed to control densimetric plumes and fire plumes are the same, provided that the densimetric plumes are not excessively momentum dominated , i.e. for $\Gamma_i > 0.1$. Interestingly, we observe that the dynamics of fire plumes for increasing HRR behaves as that of densimetric plumes with reduced Γ_i, i.e. that become more forced. As the size of the flame in the fire plumes increases and reaches the tunnel height, its dynamics becomes progressively different from that of a densimetric plume. This means that densimetric plumes represent a reliable model for fire plumes in ventilated tunnel, but only in the case of a limited extent of the flames.
- The appearance of a super-critical velocity corresponds to the condition at which the fire plume no longer behaves as a densimetric plume induced by a localised source of buoyancy. This phenomenon can therefore attributed to the existence of a distributed source of buoyancy extending downstream the source and occupying the whole tunnel height.

As a conclusion, we can then assert that the downstream displacement of the volume distributed buoyancy source can be then regarded as the main reason for the progressive weakening of the dependence of the critical velocity on the HRR, i.e. for the appearance of a super-critical ventilation velocity.

Appendix: sensitivity to different subgrid models

To investigate the influence of subgrid models on the critical velocity, we compare the results using two subgrid models (the default Deardorff's model and Vreman's model) at two heat release rates, 1000 W and 23000 W.

The comparison is based on the analysis of longitudinal profiles of the velocity and temperature taken at 2 cm below the ceiling. The temperature profile is shown in Fig. 4.11, and the velocity profile is shown in Fig. 4.12. The temperature field is shown in Fig. 4.13, and the velocity field is shown in Fig. 4.14. All the data is the average value between 30 s

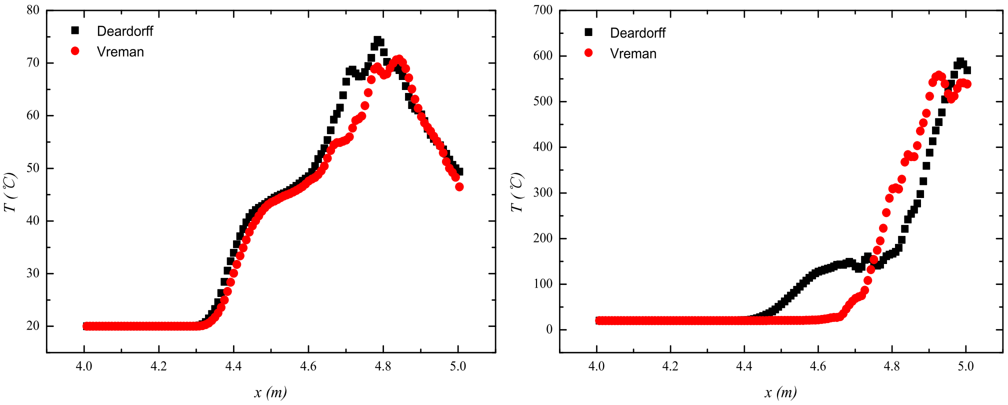

Fig. 4.11 Longitudinal temperature profiles at the ceiling level of HRR at 1000 W (*V*=0.35 m/s) and 23000 W (*V*=0.70 m/s).

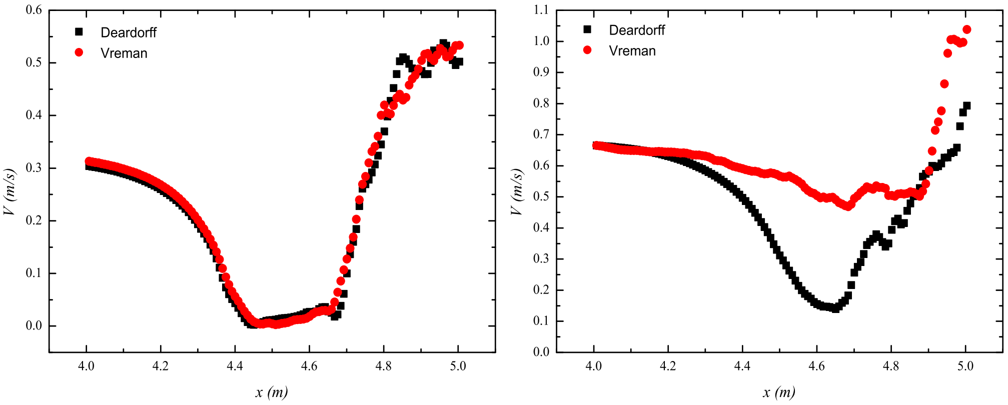

Fig. 4.12 Longitudinal velocity profiles at the ceiling level of HRR at 1000 W (*V*=0.35 m/s) and 23000 W (*V*=0.70 m/s).

and 60 s . For HRR=1000 W, the ventilation velocity is 0.35 m/s and for HRR=23000 W, the ventilation velocity is 0.70 m/s.

For HRR=1000 W, the critical velocity given by Deardorff's model is 0.38 m/s and is 0.37 m/s by Vreman's model. For HRR=23000 W, the critical velocity is 0.71 m/s when computed with the Deardorff's model and 0.65 m/s with Vreman's model. It can be seen that for small HRR, the two subgrid models give similar results while for large HRR the Deardorff's model provides a higher critical velocity. The difference between the two is however little.

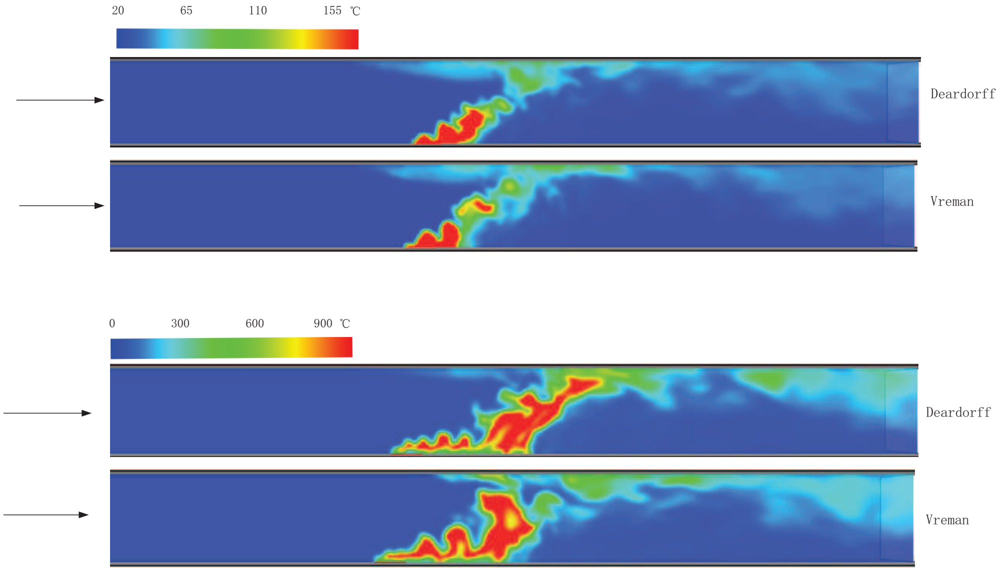

Fig. 4.13 Temperature field of HRR at 1000 W (V=0.35 m/s) and 23000 W (V=0.70 m/s).

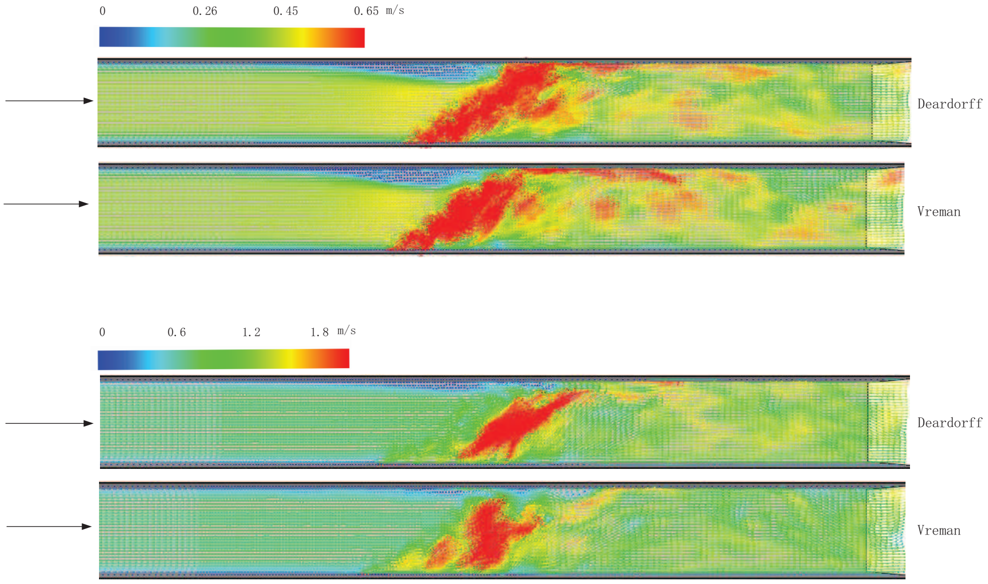

Fig. 4.14 Velocity field of HRR at 1000 W (V=0.35 m/s) and 23000 W (V=0.70 m/s).

Chapter 5

Effect of inclination on critical ventilation velocity

Due to the stack effect, smoke movement in inclined tunnels can be significantly different from that in horizontal tunnels. This can have a significant influence on the critical velocity. Previous tunnel fire studies have a suggested correlation between the critical velocity V_c and the tunnel slope θ in a form $V_c/V_{c0} = 1 + k\theta$, where V_{c0} is the critical velocity in the horizontal tunnel, and k is a constant. The value of k, determined experimentally and numerically in different studies, can be however very different from one case to another. The reason for these difference have not been so far clarified, which motives further research work. In order to unveil this feature, we tackle this problem theoretically, experimentally and numerically. The theoretical model relies on an a top-hat plume impinging on the ceiling, and predicts a dependence, in case of buoyancy-driven releases, of the form $V_c/V_{c0} = \sqrt{1 + C_k \sin\theta}$ (which is different from that proposed by previous authors). Experiments are performed in a reduced scale tunnel, inclined from -5° to $+5^\circ$, and using light gas mixture (air/helium) to simulate the presence of light smokes. Numerical simulations are performed using FDS (Fire Dynamics Simulator) with hot-air plume and propane fire.

Experimental results show that the dynamical condition at the source affects the critical velocity: when the buoyant plume is momentum-driven, the influence of slope is small; when the buoyant plume is buoyancy-driven, the influence of slope is large. This features are conveniently reproduced by the analytical model adopting $C_k = 2.1$. Similar influence of Γ_i has been observed in the hot-air plume simulation with that in the experiment. Finally, in the numerical simulation of propane fire, results show that the influence of the slope on the ratio V_c/V_{c0} is not affected by the heat release rate.

5.1 Introduction

The critical velocity is the minimum ventilation velocity that has to be imposed in a longitudinally ventilated tunnel in order to prevent reverse flow of smoke in case of fire. Its dependence on the heat release rate of the fire (Oka and Atkinson (1995), Wu and Bakar (2000)), has been so far the object of several studies, focusing on the case of horizontal tunnels. The case of inclined tunnels has instead received less attention.

The influence of slope (defined as negative when the entrance of fresh air is at a lower elevation than the source) on the movement of smoke is mainly related to the ‘stack effect’ (Merci, 2008) i.e. to the role of the component of buoyancy along the tunnel axis. For these reasons we generally expect that, compared to a horizontal tunnel, the critical velocity will be larger for downhill slope (and smaller for uphill slope).

In the literature, it is common practice to evaluate the effect of slope on the critical velocity V_c assuming as a reference case the value V_{c0} of the critical velocity obtained for the horizontal case.

For operational purposes, the correlation provided by the US Department of Transport Subway Environment Simulation Program (SES), is $V_c/V_{c0} = 1 + 0.0374s^{0.8}$. This correlation is assumed to hold for tunnels with downgrades from 0° to 10°. The correlation is also adopted by the NFPA 502 standard (Annex D, 2014 edition).

The results of research studies are instead generally presented by fitting the experimental or numerical data with a linear relation of the form

$$V_c/V_{c0} = 1 + k\theta \tag{5.1}$$

where k is a coefficient and θ is the inclination of a tunnel defined by angle in degree (in practice, tunnel slope can also be defined as a percentage $s = \tan\theta \times 100\%$, i.e. given by the ratio of uphill height to horizontal length).

Atkinson and Wu (1996) conducted experiment in a reduced-scale tunnel using propane in porous bed burner for varying heat release rates. They found that the critical velocity ratioV_c/V_{c0} varied little for values of $Q^* = \dfrac{Q}{\rho_0 c_p T_0 g^{1/2} H^{5/2}}$ between 0.2 and 0.4, where Q is heat release rate, c_p is specific heat capacity, ρ_0 and T_0 are the ambient air density and temperature, respectively, g is gravity acceleration and H is tunnel height. They concluded that the stack effect has a slight influence on the critical velocity in the range $0 \leq \theta \leq 10^\circ$, and proposed the following relation:

$$V_c/V_{c0} = 1 + 0.014\theta \tag{5.2}$$

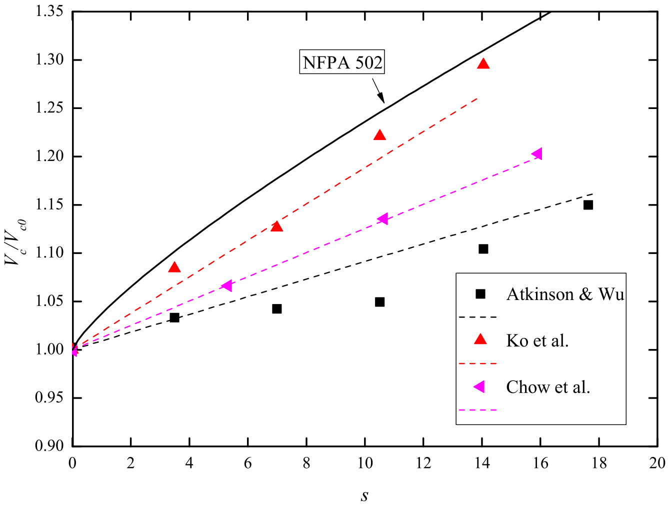

Fig. 5.1 Critical velocity ratio V_c/V_{c0} as a function of tunnel slope.

This correlation is in good agreement with the tendency identified by Vauquelin (2005) in an isothermal reduced-scale model test, with channel slope between -16% and +16%.

Ko et al. (2010) conducted experiments at five different slopes 0, 2, 4, 6, and 8° using methanol, acetone, and n-heptane at two different fire pools. The heat release rate varied in the range $1.11-15.6$ kW. Ko et al. (2010) found that the critical velocity increases with tunnel slope for each fuel type and pool size, non-dimensional critical velocity could be fitted into a single correlation, regardless of the heat release rate:

$$V_c/V_{c0} = 1 + 0.033\theta \tag{5.3}$$

Yi et al. (2014) investigated the influence of slope in a reduced-scale model (in the range $-3\% \leq s \leq 3\%$), using methanol pool fires. Yi et al. (2014) found that, as the tunnel slope increases from downhill to uphill, the critical velocity decreases at a rate that is independent of the heat release rate of the fire source, according to a fit of the form:

$$V_c/V_{c0} = 1 + 0.034s \tag{5.4}$$

Chow et al. (2015) studied the smoke movement in a reduced-scale tilted tunnel using gasoline 93# with three pool diameters, and for tunnel slopes up to 9°, and fitted their results by the following relation:

$$V_c/V_{c0} = 1 + 0.022\theta \tag{5.5}$$

An overall comparison of the literature data previously presented is shown in Fig. 5.1. Note that this plot includes results obtained with different experimental condition, in particular

	$D_i(m)$	H/W	D_i/W	Tunnel shape (m)
Atkinson & Wu (propane burner)	0.10	0.89	0.36	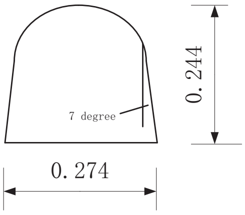
Ko et al. (pool fire)	0.065, 0.085	1	0.16, 0.21	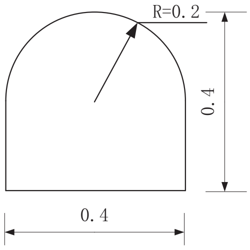
Chow et al. (pool fire)	0.16, 0.20, 0.26	0.67	0.11, 0.13, 0.17	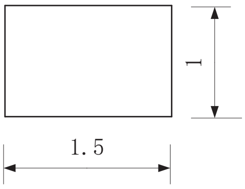

Table 5.1 Tunnel geometry of reduced scale tests in previous study.

with different typologies of heat sources: propane gas burner for Atkinson and Wu (1996), pool fire for Ko et al. (2010) and for Chow Chow et al. (2015). The plot also includes the relation recommended in the NFPA 502. To improve the readability of the graph, we plot only one-set of data for each experiment, together with the linear relation used by the different authors to fit their data sets. Note also that we have avoided plotting the data from Yi et al. (2014), since these are affected by too large experimental uncertainties.

In Fig. 5.1 it is clearly shown that the values of the constant k vary significantly from one study to another. In principle, this different behavior can be explained by the fact that these data have been obtained in different experimental set-up, with different geometrical configuration and different typologies of fire sources. The different experimental set-ups are summarized in Table 5.1, where we report the values of the source diameter D_i, the tunnel height H and width W, as well as their ratios, the shape of the tunnel section and the typology of fuel used.

Here we aim in evaluating the influence of these varying factors on the critical velocity. Namely, aim of this study is to investigate the influence of the source condition on the critical velocity in inclined tunnels using light gas mixture (air/helium) as buoyant source. To that purpose, we propose a mathematical model of top-hat plume in a crossflow in an inclined tunnel. Its predictions are compared to the results of experiments, performed in a reduced scale tunnel. We also conduct numerical simulations using the software FDS 6.3, which is used to investigate the difference between buoyant plumes and propane fires.

5.2 Theory

In a general way, the release of light gas from a a circular source placed at the center of the tunnel can be represented as a buoyant plume in a crossflow impinging on the ceiling. The sketch of a plume released in an inclined ventilated tunnel is shown in Fig. 5.2. The balance equations for mass, vertical momentum, density difference and longitudinal momentum can be written as

$$\begin{cases} \dfrac{\mathrm{d}}{\mathrm{d}y}(\rho w b^2) = 2\rho_0 u_e b, & \text{(5.6a)} \\ \dfrac{\mathrm{d}}{\mathrm{d}y}(\rho w^2 b^2) = (\rho_0 - \rho) g b^2 \cos\theta, & \text{(5.6b)} \\ \dfrac{\mathrm{d}}{\mathrm{d}y}\left[(\rho_0 - \rho) w b^2\right] = 0, & \text{(5.6c)} \\ \dfrac{\mathrm{d}}{\mathrm{d}y}(\rho u w b^2) = C_x \sqrt{\rho \rho_0}(V - u)^2 b/\pi - (\rho_0 - \rho) g b^2 \sin\theta, & \text{(5.6d)} \end{cases}$$

where b is the characteristic plume radius, w and u are its vertical and longitudinal velocities, respectively, $u_e = \alpha w$ is the entrainment velocity, ρ is the plume density, V is the ventilation velocity, θ is the tunnel inclination, and C_x is a drag coefficient. Boundary conditions imposed at the source are $b(0) = b_i$, $w(0) = w_i$, $u(0) = 0$, and $\rho(0) = \rho_i$. The equations (5.6a)-(5.6d) are based on the control equations of the case in a horizontal tunnel (equations 3.4a-3.4d), detailed information of which is presented in Chapter 3. The vertical and longitudinal momentum equations are slightly changed to include the effect of the buoyancy. This model is here used to compute the velocity w_H, radius b_H and density ρ_H characterize the plume at the impingement point.

As in Chapter 3, the critical velocity for the inclined tunnel can be computed by assuming that the momentum flux imposed by the ventilation flow balances the longitudinal momentum flux, the pressure force of the buoyant flow at the ceiling and the longitudinal component of

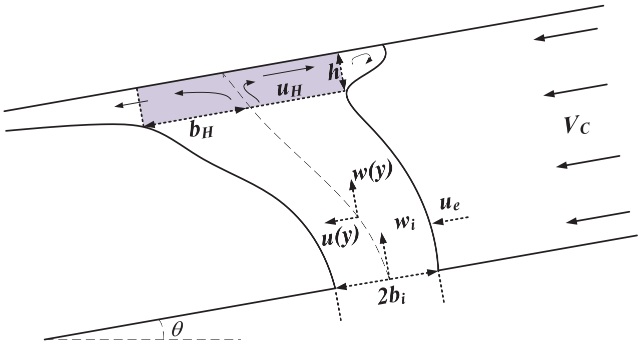

Fig. 5.2 Sketch of the plume released in an inclined ventilated tunnel and of its impingement at the tunnel ceiling.

the buoyancy force due to the buoyancy fluctuated momentum:

$$\rho_0 {V_c}^2 = \varphi[\rho_H {u_H}^2 + \frac{1}{2}(\rho_0 - \rho_H) g h \cos\theta] + \varphi_2(\rho_0 - \rho_H) g h \sin\theta. \tag{5.7}$$

Compared with the horizontal case, an additional term $\varphi_2(\rho_0 - \rho_H) g h \sin\theta$ is included to account the effect of buoyancy in the longitudinal direction. As in Chapter 3, the pressure term is neglected so that Eq. (5.7) can be approximated as:

$$\rho_0 {V_c}^2 = C^2 \rho_H {w_H}^2 + C_2(\rho_0 - \rho_H) b_H g \sin\theta \tag{5.8}$$

with $C^2 = \varphi/\gamma^2$ and $C_2 = (\varphi_2 \gamma)/2$.

To obtain an analytical solution and compare this critical velocity with that in a corresponding horizontal tunnel V_{c0} (Eq. (3.8)), an assumption needs to be made; namely that the term $\cos\theta$ in Eq. (5.6b) has little effect on $\rho_H {w_H}^2$. To validate this assumption, numerical solutions of Eq. (5.6) have been computed at $\theta = 0$, 5° and 10°. The case $\theta = 0$ provides a reference value $\rho_{H0} {w_{H0}}^2$, where ρ_{H0} and w_{H0} are the computed density and the vertical velocity at the ceiling for a horizontal tunnel. The critical velocity in the horizontal tunnel is thus $\rho_0 {V_{c0}}^2 = C^2 \rho_{H0} {w_{H0}}^2$. Results of the ratio between $\rho_H {w_H}^2$ and $\rho_{H0} {w_{H0}}^2$ are shown in Fig. 5.3, which suggest that $\rho_H {w_H}^2$ is close to $\rho_{H0} {w_{H0}}^2$, so $\rho_0 {V_{c0}}^2 = C^2 \rho_H {w_H}^2$. In other words, the term $\cos\theta$ in Eq. (5.6b) can be neglected when computing the critical velocity, and the solutions obtained in Eq. (3.10) can be directly applied to the case of a slightly inclined tunnel.

With the above assumption, the ratio between critical velocity and its corresponding horizontal case V_c/V_{c0}:

$$\frac{V_c}{V_{c0}} = \sqrt{1 + C_k \frac{\rho_0}{\rho_H} \Gamma_H \sin\theta} \tag{5.9}$$

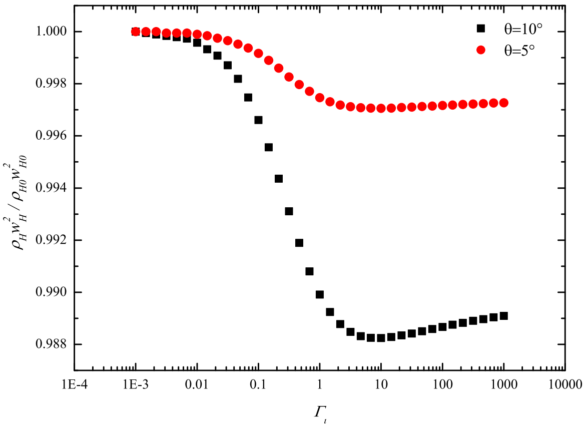

Fig. 5.3 Numerical solution of the ratio $\rho_H {w_H}^2/\rho_{H0} {w_{H0}}^2$ at 5° and 10°. Computations are performed with: $D_i = 0.1$ m, density ratio $\rho_i/\rho_0 = 0.7$.

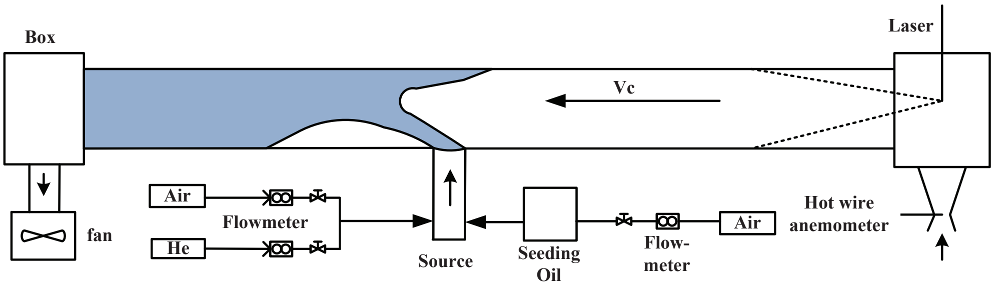

Fig. 5.4 Schematic of the experimental set-up.

with $C_k = (8\alpha_0 C_2)/(5C)$. This solution suggests that the influence of the tunnel slope is linked to the dynamical conditions of the plume at the impingement, notably on its local value of the Richardson number Γ_H and the local density difference. For a lazy plume, we expect that $\Gamma_H \to 1$ and $\dfrac{\rho_0}{\rho_H} \to 1$ (see the discussion in Section 3.2.2), Eq. (5.9) reduces to:

$$\frac{V_c}{V_{c0}} = \sqrt{1 + C_k \sin\theta} \tag{5.10}$$

5.3 Experimental and numerical methods

5.3.1 Experiment

Experiments were performed in an isothermal reduced-scale model (Fig. 5.4) of length $L = 8.9$ m, width $W = 0.36$ m and height $H = 0.185$ m. The tunnel inclination could be adapted from -5° to +5° i.e. -8.7% to +8.7%. The side walls are made in PMMA which allows the flow to be visualised.

Γ_i	6.02	1.53	1.48	0.37	0.075	0.181	0.0075
D_i	0.1	0.1	0.05	0.05	0.05	0.035	0.025
ρ_i/ρ_0	0.7	0.7	0.7	0.7	0.7	0.53	0.7

Table 5.2 Test conditions for tunnel inclined from -5° to +5°.

The longitudinal ventilation is created by an extraction fan installed at the tunnel outlet. The volume flow rate of the incoming air is measured by a hot-wire anemometer placed within a Venturi tube at the tunnel inlet. The buoyant source is modeled by an air/helium mixture, released from a circular source at the tunnel ground. The flow rates of air and helium are controlled independently and measured by two flow meters. To visualize the flow, air/helium mixture is seeded with nebulized oil and a lens is installed at the tunnel inlet. Note that the mass of oil added into the buoyant release is tiny, and therefore does not affect the density of the mixture. In the experiments we produced releases with a varying values buoyancy flux at source:

$$B_i = g\frac{\Delta\rho}{\rho_0}\frac{\pi}{4}{D_i}^2 w_i \tag{5.11}$$

and providing a varying plume Richardson number:

$$\Gamma_i = \frac{5}{8\alpha}\frac{\eta_i g b_i}{w_i^2} \tag{5.12}$$

where $\alpha = 0.127$ is a reference top-hat plume entrainment constant, ρ_0 is the density of ambient air, $\Delta\rho = \rho_0 - \rho_i$, ρ_i is the density of plume and w_i is the velocity at the source. The buoyant release could then be classified as momentum-driven forced plumes ($\Gamma_i < 1$), and buoyancy-driven pure ($\Gamma_i = 1$) and lazy ($\Gamma_i > 1$) plumes (Le Clanche et al., 2014). The releases ranged from highly forced ($\Gamma_i \ll 1$) to lazy ($\Gamma_i > 1$), issuing from source with varying source diameter. Four source diameters were used (D_i=2.5, 3.5, 5.0, 10.0 cm), with a Richardson number in the range $0.0075 \leq \Gamma_i \leq 6$. Note that, in order to avoid low-Reynolds number effects, lazy plumes had to be released from larger sources. The density ratio (ρ_i/ρ_0) at the source was set equal to 0.7, except for one case, needed to compare our results with similar data produced by Vauquelin (2005). The test conditions are summarised in Table 5.2.

5.3.2 Numerical simulations

The simulation was performed in a tunnel with a same cross-section ($H/W = 0.5$) of the experimental test but smaller length L ($L = 33H$ instead of $L = 44H$) to save computation time. The tunnel inclination was adapted by varying gravity components in x and y direction.

At the inlet, the ventilation velocity was fixed and at the outlet it was set as 'open'. The circular source ($D_i = 0.1$ m) in the experiment is modeled by a square source with the same area, i.e. 0.09×0.09 m. This was located 4.5 m away from inlet and at the tunnel centre. 50 temperature receptors were set 2 cm below the ceiling from 0.5 m upstream the fire source to 0.5 m downstream of it. To estimate the position of the front of the backlayering flow we analysed the longitudinal profile of mean temperature. The front was set at the location at which the air below the ceiling was characterised by a 2 °C difference compared to the ambient temperature.

Two kinds of buoyant releases were simulated: hot-air plumes and propane fires. The hot-air plume was used to reproduce the air/helium mixture in the experiments (i.e. same density ratio and flow rate). To this purpose, the radiation solver was turned off and the tunnel walls were set as adiabatic. Propane releases were instead used to reproduce the case of a real fire, including the effects of i) a distributed source of buoyancy (flames) ii) radiation iii) heat losses at the tunnel walls. The wall thickness was 5 cm, with the wall backed up to ambient. The wall was defined as 'concrete' with a density equal to 2000 kg/m^3, a specific heat of 0.88 kJ/(kg K) and a conductivity of 1.2 w/(m K).

We simulated five cases of propane fire. For four of these, the fire was characterised by a heat release rate (HRR) that was the same as that of an 'equivalent case' of a hot-air plume, i.e. $Q = c_p q_i \rho_i (T_i - T_0)$ (q_i is the flow rate), therefore providing a same buoyancy flux

$$B_i = \frac{Qg}{\rho_0 c_p T_0} \tag{5.13}$$

as that characterising the densimetric plumes. The case characterised by the highest HRR, i.e. Q = 15 kW, had however no corresponding hot-air plume.

To increase the resolution in the near-source region, the grid was stretched in the longitudinal direction. The tunnel was then divided into three sub-domains: the domain close to the inlet is referred to as 'Left Domain', the domain containing the source as 'Middle Domain', and the domain close to the outlet as 'Right Domain'. The lengths of the three domains were 4 m, 1 m and 1 m, respectively. The grid size in the Middle Domain is kept the same in the three directions 0.008m×0.008m×0.008m, while in the other domains the size is 0.016m×0.008m×0.008m. As a result, the simulation domain was divided into 420×43×21 grids along the length, width and height direction, i.e. a total of 379260 cells.

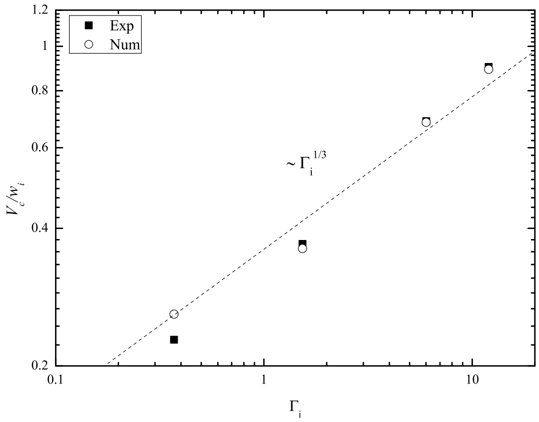

Fig. 5.5 Non-dimensional critical velocity as function of Γ_i, in case of buoyant fluid releases: comparison between the experimental and numerical results

As indicated by (McGrattan et al., 2008), another criterion that has to be satisfied by the grid size is given by the value of a characteristic fire diameter:

$$D^* = \left(\frac{Q}{\rho_0 c_p T_0 \sqrt{g}} \right)^{\frac{2}{5}} \tag{5.14}$$

According to (McGrattan et al., 2008) the non-dimensional ratio $D^*/\delta x$ (δx is the nominal size of a mesh cell) has to be in the range $4 \sim 16$. Note that this recommendation requires higher mesh resolution for smaller fires. In the present study the smallest fire was 0.20 kW, which makes $D^*/\delta x$ equal to 4, i.e. within the recommended range.

Each simulation lasted 60 s. The flow required approximately 30 s to reach a steady state (statistically). Therefore the position of the backlayer flow was obtained by averaging the velocity field between 30 s and 60 s. A first validation of the numerical results could be obtained by comparison with the experimental results, for the horizontal case. This is shown in Fig. 5.5, presenting the dependence of the non-dimensional critical velocity V_c/w_i on the plume Richardson number at the source Γ_i, in case of buoyant plumes. For the four values of Γ_i investigated, the FDS predictions agree well with the experimental results and are proportional to $\Gamma_i^{1/3}$ as suggested by Le Clanche et al. (2014).

Preliminary numerical results are presented in Fig. 5.6. The temperature field and smoke in case of a HRR of 0.57 kW and 15 kW show that, at a same ventilation, the backlayering length is different depending on the slope: a positive slope helps the formation of the backlayer, while a negative slope helps reaching the critical condition.

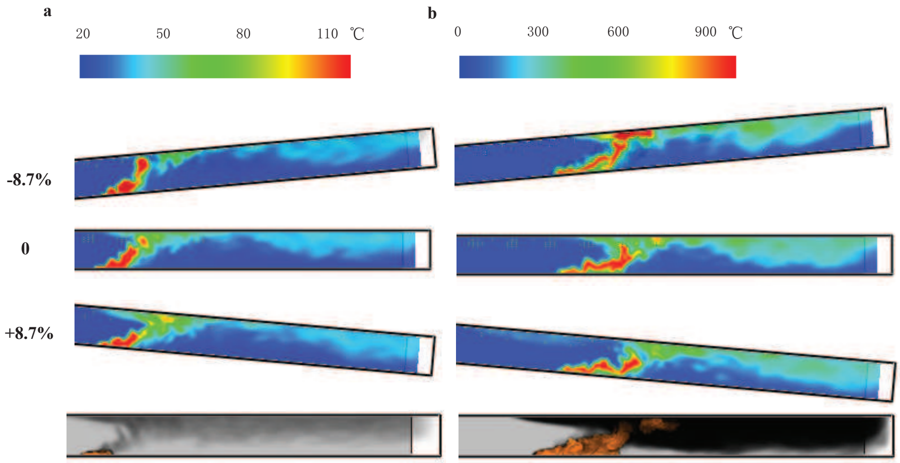

Fig. 5.6 Temperature field of propane at 0.57 kw (V=0.33 m/s) and 15.0 kw (V=0.55 m/s) at -8.7%, 0 and 8.7%.

5.4 Results

5.4.1 Experimental and analytical results of air/helium releases

Figure 5.7 shows the experimental and analytical results concerning the dependence of the critical velocity, normalized as V_c/w_i and V_c/V_{c0}, as a function of slope for a wide range of source Richardson number Γ_i. Generally good agreement has been achieved between the experiment and the model (Eq. 5.9), adopting a value of the constant C_k equals to 2.1 . Note in particular that the role of Γ_i is correctly reproduced. The non-dimensional critical velocity V_c/w_i is clearly dependent on the plume Richardson number Γ_i, but this dependence varies significantly with a varying slope. In general we observe that V_c/w_i increases with an increasing slope. This tendency is clearly visible for large values of Γ_i and tends to fade out for small Γ_i. The trend can be also conveniently evidenced by analysing the velocity ratio V_c/V_{c0}. For a same slope, as Γ_i decreases, the ratio V_c/V_{c0} becomes closer to one. Note that, despite some discrepancies mainly due to the experimental uncertainties, this set of data is in general agreement with the results of Vauquelin (2005).

To explain these results it is useful to recall some fundamental concepts arising from the literature on buoyant plume dynamics and reflected in the solution in Eq. (5.9). The Richardson number Γ_i is a non-dimensional parameter expressing the ratio of the inertial force to buoyancy at source. A main finding of plume theory (Van Den Bremer and Hunt, 2010) indicates that the lower the value of Γ_i, the larger the distance needed to attain pure plume conditions, i.e. $\Gamma_H = 1$. Based on this, and given the relatively short distance between the source and the ceiling, highly forced releases impinge on the ceiling with an identical

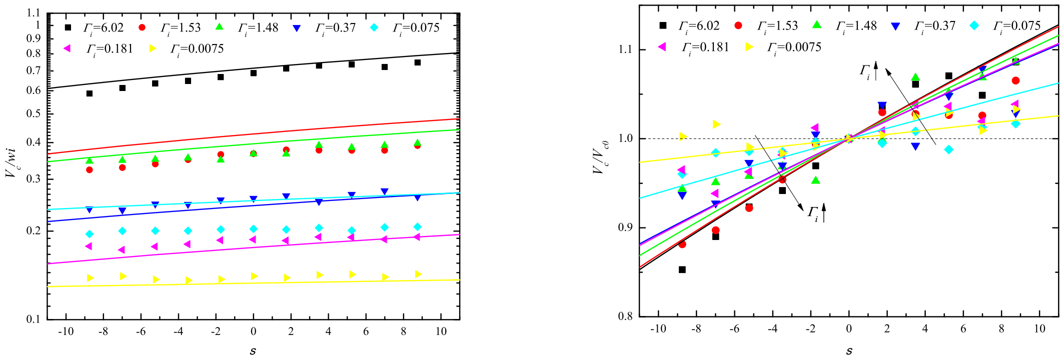

Fig. 5.7 Dependence of V_c/w_i and of the critical velocity ratio V_c/V_{c0} as a function of the slope, comparison between experimental results and analytical solution of the model Eq. (5.9).

balance of fluxes. Compared to forced plumes, lazy plumes rapidly attain the condition of a pure plume ($\Gamma_H \rightarrow 1+$) as Γ decreases quickly with distance from the source. When Γ_i is large, the flow impinging the ceiling is buoyancy dominated, and the influence of stack effect is large, so that V_c/V_{c0} increases with the increase of slope. Conversely, when Γ_i is small, the flow impinging the ceiling is still momentum dominant, and the influence of the stack effect is small. Therefore for $\Gamma_i \rightarrow 0$, the ratio V_c/V_{c0} remains close to unity, regardless of the slope.

5.4.2 Numerical results of hot-air plume and propane

As specified in Section 5.3.2, the propane fire cases were set by imposing a HRR that was the same as that imposed in case of hot-air plumes. The comparison of the results of these two sets of simulations will be then based on the value of a critical tunnel Froude number, defined as:

$$Fr_c = V_c \left(\frac{H}{B_i}\right)^{1/3} \tag{5.15}$$

and expressing the ratio between the inertia of the ventilation flow (at the critical condition) and the effects due to the injection of buoyancy at the source.

Figure 5.8 shows a comparison between the experimental and numerical results, considering the case of the injection of buoyant plumes (with D_i=0.1 m). The two sets of data, for both Γ_i=6.02 and Γ_i=1.53, show a general good agreement with each other. Note also that releases for higher Richardson number, i.e. Γ_i=12, behave very similarly to those with lower ones, i.e. Γ_i=6.02 and 1.53. Therefore, when plotted as the ratio V_c/V_{c0} the critical velocity seems to collapse on a single curve. The only data that differs from this general behavior are the numerical results for Γ_i=1.53. The reasons for this are still unclear and require further investigations.

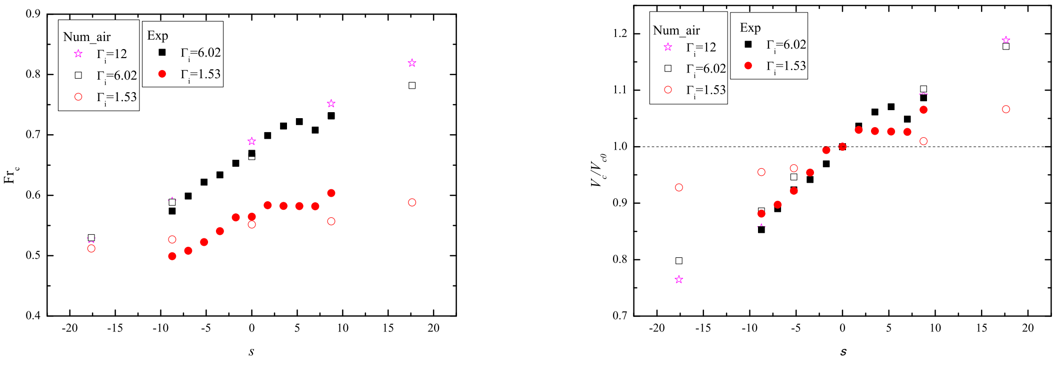

Fig. 5.8 Dependence of the critical Froude number Fr_c and of the critical velocity ratio V_c/V_{c0} as a function of the slope in case of buoyant plumes. Comparison between experimental and numerical results (D_i=0.1 m).

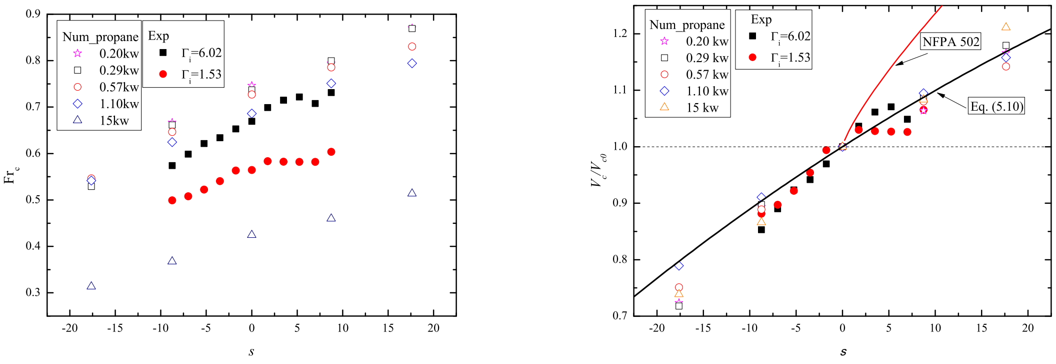

Fig. 5.9 Dependence of the critical Froude number Fr_c and of the critical velocity ratio V_c/V_{c0} as a function of the slope in case of propane fires. Comparison between experimental results on buoyant plumes and numerical results on propane fires (D_i=0.1 m), the solution provided by Eq. (5.10) is also plotted.

Figure 5.9 shows the experimental and numerical results with propane for D_i=0.1 m. The numerical results show that, for low values of Q, Fr_c is insensitive to variations of Q. Differently from the case of buoyant (air/helium or hot-air) plumes, the dependency of V_c/V_{c0} on slope does not vary with heat release rate Q. In fact, all the results relative to propane fires show a trend which is very similar to that of the results of lazy plumes in the helium releases experiments. Consequently, the data could be fitted by Eq. (5.10), the analytical solution proposed for the lazy plume.

Therefore, numerical results support previous findings (Atkinson and Wu, 1996; Chow et al., 2015; Ko et al., 2010; Yi et al., 2014): in a real fire, Q is of little importance in determining the critical velocity ratio, both in case of small fire (with small flame extent) or a large fire (with flame reaching the tunnel ceiling). The different behaviour observed in the case of buoyant plumes and propane fires has therefore to be attributed to the presence of combustion, since this produces a volume distributed buoyant source.

5.5 Conclusions

Literature results on the dependence of the critical velocity on the tunnel slope suggest that varying conditions (source size and fuel typology) imposed at the source may play a significant role in determining the critical conditions. To investigate the effect of the source condition, we propose a mathematical model of a top-hat plume in a crossflow impinging on the ceiling. We have also investigated the influence of tunnel inclination on the critical ventilation velocity by means of experiments in a reduced scale tunnel using air/helium mixture and numerical simulations of buoyant sources induced by the injection of hot-air and propane fires.

Our analytical solution suggests that the effect of the slope of a buoyant plume can be expressed as:

$$\frac{V_c}{V_{c0}} = \sqrt{1 + C_k \frac{\rho_0}{\rho_H} \mathit{\Gamma}_H \sin\theta} \tag{5.16}$$

A correlation which differs from that proposed in previous studies.

Results of densimetric plume experiments and hot-air plume simulations confirm that the effect of the slope exhibits a clear dependence on the source Richardson number $\mathit{\Gamma}_i$, in accordance with Eq. (5.16). For forced releases (small $\mathit{\Gamma}_i$), the effect of slope on the critical condition is reduced. For lazy releases (large $\mathit{\Gamma}_i$), the effect of slope on the critical condition is large. These features can be correctly reproduced by Eq. (5.16). For lazy releases, Eq. (5.16) reduces to:

$$\frac{V_c}{V_{c0}} = \sqrt{1 + C_k \sin\theta} \tag{5.17}$$

In case of a volume distributed buoyancy source, i.e. a fire, the power seems to be have very little influence on the effect of the slope, and the results of V_c/V_{c0} could be fitted into a single line, irrespective of the HRR. In this case, the results show a similar trend with lazy releases and could be fitted by Eq. (5.17).

Chapter 6

Effect of blockage on critical ventilation velocity in tunnels

We conducted small-scale experiments and numerical simulations to investigate the effect of vehicular blockage on the critical velocity in a longitudinal ventilated tunnel. In the experiment, the fire source was modeled by densimetric plumes (air/helium mixture) and three sizes of blocks, occupying 15%, 19% and 43% of the tunnel cross-section, were studied. Numerical simulations were performed with Fire Dynamics Simulator (FDS) and concerned hot-air plumes and fire sources (propane). Experimental data shows that only the block close to the fire source affects the critical velocity, whereas the effect of other blocks (of the same size) located further upstream is trivial. As the fire-blockage distance becomes larger, the critical velocity changes and becomes close to that of an empty tunnel. The relative position of the block and the fire source has a large influence on the critical velocity V_c: when the ventilation flow cannot reach the fire plume directly, a larger V_c is needed compared with that in an empty tunnel; when the ventilation flow can reach the fire plume directly a smaller V_c is needed, and the reduction ratio is similar to the blockage ratio. Numerical simulations have shown good agreement with the experiments with both source conditions, i.e. hot-air plumes and propane fires. The temperature and velocity fields given by the numerical simulations suggest that, despite a different dynamical behaviour between densimetric plumes and fire plumes, the critical velocity changing ratio seems to be only affected by the blocks rather than by the source condition.

6.1 Introduction

In case of a tunnel accident, with people evacuating as fast as possible, there might be vehicles left close to the fire source producing a blocking effect on the ventilation flow (Fig. 6.1). In this case, local ventilation velocity might be increased or decreased due to the relative position of the fire and the block, inducing significant modifications to the value of the critical velocity, defined as the minimum longitudinal ventilation velocity that prevents the smoke from flowing upstream the source. When considering the case of empty tunnel, it is generally agreed that at low heat-release rates the critical velocity varies as the one-third power of the heat release rate, and becomes almost independent of it for large heat-release, as the flames reaches the ceiling (Le Clanche et al., 2014; Oka and Atkinson, 1995; Weng et al., 2016; Wu and Bakar, 2000). This dependence can however be altered by obstacles placed within the tunnel, whose presence can significantly affect the incoming ventilation flow.

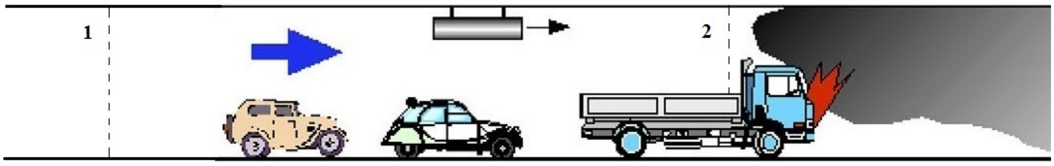

Fig. 6.1 Tunnel fire with vehicle blockages upstream in the longitudinal ventilation, adapted from Vauquelin (2008).

In order to study the role of obstacles blocking the ventilation in tunnels, there have been to date several experimental and numerical studies, focusing for example on the effects of blocks on the maximum gas temperature beneath ceiling (Hu et al., 2013) or on the smoke backlayering (Zhang et al., 2016). Most of the studies focused however on the influence of the obstacles on the critical ventilation velocity. In these studies, a common approach is to assume that, for a given heat release rate, the velocity needed to push the smoke downstream, in presence of vehicle blocking the flow, would be the same as that needed within an empty tunnel. Identifying as ‘1’ and ‘2’ two different positions in the tunnel (see Fig. 6.1), the first located well upstream the burning vehicle (i.e. position 1) and the second placed where the burning vehicle is placed (i.e. position 2), we can refer to as $V_{c,1}$, A_1, $V_{c,2}$, A_2, the relative flow velocities and tunnel cross-sectional area. Volume conservation implies that $V_{c,1}A_1 = V_{c,2}A_2 = V_{c,2}A_1(1-\psi)$, where $\psi = (A_1 - A_2)/A_1$ is the tunnel blockage ratio. Assuming that $V_{c,2} = V_{c0}$, and referring to as V_c the velocity at the position ‘1’, we can then write:

$$V_c = V_{c0}(1-\psi) \tag{6.1}$$

which expresses a reduction of the critical velocity for an increasing of the blockage ratio.

Oka and Atkinson (1995) studied the effect of blockage by placing a propane gas burner above a broken vehicle. They found that, for a vehicle occupying the tunnel half-height, with a reduction of the tunnel section of 12%, the reduction in critical velocity was 15%. For a reduction of the effective section of 32% the reduction in the critical velocity was instead $40\% - 45\%$.

Li et al. (2010) placed a model of a train above a porous burner to simulate a fire occurring beneath the vehicle. They found that when the train section was 20% of the tunnel section, the critical velocity was reduced by 23%, which was in accordance with Eq. (6.1).

Lee and Tsai (2012) studied three vehicles types in different array configurations placed upstream a gasoline pool fire, occupying $5\% - 31\%$ of the cross-sectional area. They showed that when the ventilation flow could reach the fire directly, the critical velocity decreased at same ratio of the blockage ratio, due to the increase of the local ventilation (Eq. (6.1)). The distance between the fire and the vehicles also influenced the critical velocity but played a secondary role. On the contrary, when the ventilation could not reach the fire directly, the fire power increases and the critical velocity increases compared to the case of an empty tunnel.

Li et al. (2012) carried out numerical simulations in a small-scale tunnel using Fire Dynamic Simulator (FDS) with a fire source placed above a thermally inert cube, and with a blockage ratio varying from 10% to 71%. They verified that the reduction of the critical velocity due to blockage could be taken as corresponding blockage ratio in tunnels (Eq. (6.1)).

Tang et al. (2013) investigated experimentally the effect of the fire-blockage distance on the critical velocity and the backlayering length by placing a block upstream a porous burner source. The fire was locally protected by the block, thus inducing a lager critical velocity. It was found that when the fire-blockage distance was lager than a certain value (larger than 3.3 times the hydraulic diameter of the tunnel) the critical velocity would become the same as that in an empty tunnel. During the test, when increasing the fire-blockage distance, both the backlayering length and the critical velocity decreased progressively, until reaching a constant value. Based on these observations they proposed a correlation relating the critical velocity in presence of a block and the corresponding critical velocity in an empty tunnel:

$$\frac{V_c}{V_{c0}} = \begin{cases} \dfrac{1}{1-\psi\left(1-\frac{L}{3.3\overline{H}}\right)} & \dfrac{L}{\overline{H}} \leq 3.3, \\ 1 \quad \dfrac{L}{\overline{H}} > 3.3. \end{cases} \tag{6.2}$$

where L is the fire-blockage distance, $\overline{H}$ is the hydraulic diameter of the tunnel. It should be noted that this correlation is an empirical fit of one set of experimental results for a fixed blockage ratio ($\psi = 10\%$). Note also that, this correlation does not hold when the blockage ratio ψ is too large (for $L = 0$, when $\psi \to 1$, $V_c \to \infty$).

Rojas Alva et al. (2017) used an air-helium mixture release to simulate the presence of a fire smoke, with arrays of vehicles placed upstream. Three sizes of vehicles were used, producing blockage ratios in the range $10-41\%$. The fire sources were placed downstream either directly behind the vehicle or behind the spacing between vehicles. It was found that the critical velocity decreased in proportion with the blockage ratio when the ventilation could reach the fire directly (Eq. (6.1)). When the ventilation could not reach the fire directly a larger air flow was instead needed.

Lee and Tsai (2012) and Rojas Alva et al. (2017) found that apart from the blockage ratio, the relative position of the fire and the block also plays a role: when the fire was protected by the block and could not be reached by the ventilation flow directly, an increase, rather than a decrease, in the critical velocity was observed, although the increasing ratio was not studied in detail. Tang et al. (2013) suggested that when the fire is placed just downstream the block, the local ventilation flow velocity is smaller compared with the empty tunnels and a larger critical velocity (according to Eq. (6.2) and imply $L = 0$) is needed. In Tang et al. (2013), the protection of the block on the fire is simply indicated by a smaller ventilation velocity imposed on the fire source, however, no physical argument is provided to explain this.

The effect of the fire-blockage distance and the relative position between the fire and the blocks on the critical velocity have already been discussed (Lee and Tsai (2012), Lee and Tsai (2012), Tang et al. (2013)). In this study we experimentally examine these matters at different blockage ratios using a buoyant plume. Moreover, we interpret the difference between one block and an array of blocks of the same size placed upstream the fire. Finally, we perform numerical simulations with densimetric plumes and propane fires to study the effect of the source conditions on the critical velocity. In a tunnel accident, when a car is burning, other cars usually need to stop, therefore the situation with several blocks of the same size placed upstream was investigated.

6.2 Experiments

Experiments were performed in an isothermal reduced scale tunnel of 8.9 m (length) × 0.36 m (width) × 0.185 m (height), sketched in Fig. 6.2, with an hydraulic diameter $\overline{H} = 0.24$ m. The side walls are made in polymethylmethacrylate (PMMA) which allows visual observation. Detailed information about the experimental set-up can be found in Chapter 2.

The longitudinal ventilation is created by an extraction fan installed at the tunnel outlet. The volume flow rate of the incoming air is measured by a hot-wire anemometer placed

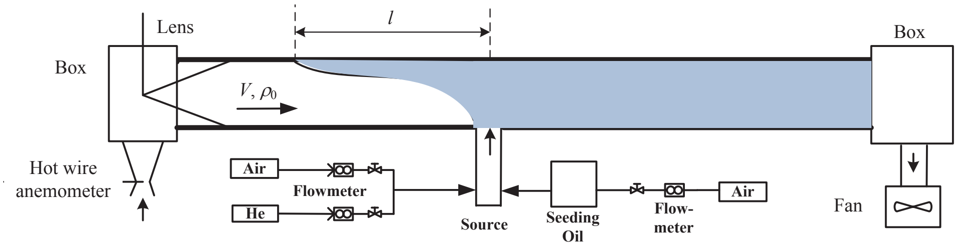

Fig. 6.2 Schematic of the experimental set-up.

within a Venturi tube at the tunnel inlet. The buoyant source is modeled by an air/helium mixture, released from a circular source (diameter $D_i = 0.1$ m) at the tunnel ground. The flow rates of air and helium are controlled independently and measured by two flow meters. To visualize the flow, the air/helium mixture is seeded with nebulized oil and a lens is installed at the tunnel inlet. Note that the mass of oil added into the buoyant release is tiny, and therefore does not affect the density of the mixture. In the experiment, the velocity at the source w_i is fixed at 0.69 m/s, density ρ_i at 0.84 kg/m^3, the corresponding heat release rate is 0.57 kW, computed as $Q = (\rho_0 - \rho_i) c_p T_0 \frac{\pi}{4} D_i^2 w_i$, with c_p the heat capacity, and T_0 and ρ_0 the ambient air temperature and density, respectively.

To study the effect of blockage on the critical velocity, a set of blocks were placed upstream the source. Three kinds of blocks, refereed to as block1, block2 and block3, were used: 0.05 m (length) × 0.1 m (width) × 0.1 m (height) (block1), 0.08 m × 0.16 m × 0.08 m (block2), and 0.12 m × 0.24 m × 0.12 m (block3), with blockage ratio 15%, 19% and 43%, respectively. Fig. 6.3 shows a schematic diagram of the top view and the side view in the tunnel cross-section for different configurations of the blocks. Three blocks configurations, refereed to as A, B and C, were considered. In configuration A, one block was placed at the center; in configuration B, one array of blocks were placed at the centre and in configuration C, two arrays of blocks were placed at the sides. In configuration A and B, the fire source was placed downstream the block and was partly blocked, so that the ventilation could not reach the fire plume directly; in configuration C, the blocks were at the sides and the ventilation flow could reach the fire directly. Note that in configuration B and C there are several blocks placed upstream the source.

We expect that when the distance between the source and the obstacles is large enough, the critical velocity would not be affected by any blockage effect. In order to evaluate this threshold distance, we placed blocks at an increasing distance from the source. For the configuration block1, the distance was 0, 0.1, 0.2, 0.3, 0.4, 0.5 and 0.6 m. For the configuration block2, the distance was 0, 0.16, 0.32, 0.48 and 0.64 m. For the configuration block3, the distance was 0, 0.24 and 0.48 m. The uncertainty of the critical velocity was estimated by repeating several times the same experiment. The uncertainty of V_c/V_{c0} was estimated of order 10%.

6.3 Numerical simulations

The simulations were performed in a tunnel with the same cross-section of the experimental test, i.e. $H/X = 0.5$, but with smaller length to save computation time. At the inlet, the ventilation velocity was fixed and at the outlet it was set as 'open'. The fire source is modeled by a square source with the same area as in the experiment, i.e. of dimensions 0.09×0.09 m. This was located 4.5 m away from the inlet and at the tunnel center.

Two kinds of buoyant releases were simulated: hot-air plumes and propane fires. The hot-air plume was used to reproduce the air/helium mixture in the experiment (i.e. same density ratio and flow rate). To this purpose, the radiation solver was turned off and the tunnel walls were set as adiabatic. Propane releases were instead used to reproduce the case of a real fire, with small fire at 0.25 kW and large fire at 7.5 kW. The physical property of the wall was defined as 'concrete' with density 2000 $\mathrm{kg/m^3}$, specific heat 0.88 $\mathrm{kJ/(kg\ K)}$ and conductivity 1.2 $\mathrm{W/(m\ K)}$, the wall thickness was 5 cm with the wall backed up to the ambient. The physical property of the blocks was defined as 'steel' with density 7850 $\mathrm{kg/m^3}$, specific heat 0.46 $\mathrm{kJ/(kg\ K)}$ and conductivity 45.8 $\mathrm{W/(m\ K)}$. The thickness was 1 cm.

A set of 50 thermocouples were placed 2 cm below ceiling in a region of 1.0 m (from 0.5 m upstream to 0.5 m downstream of the fire source). The grid size was the same as that in Chapter 4, with a mesh stretching in the longitudinal direction to obtain finer grids near the source. The tunnel is divided into three sub-domains: the domain close to the inlet is defined as 'Left Domain', the domain within which the source is placed is referred to as 'Middle Domain', and the domain close to the outlet is defined as 'Right Domain'. The lengths for the three domains were 4 m, 1 m and 1 m. The grid size in the Middle Domain is kept the same in the three directions 0.008m × 0.008m × 0.008m, while in the other domains the size is 0.016m × 0.008m × 0.008m. As a result, the simulation domain was divided into 420 × 43 × 21 grids along the length, width and height direction, i.e. a total of 379260 cells. Each simulation lasted 60 s. The flow required approximately 30 s to reach a statistically steady state. The position of the backlayer flow was then obtained by averaging the temperature field between 30 s and 60 s. The critical velocity was obtained by interpolation when the backlayering length is zero.

In the hot-air plume simulation, the critical velocity for an empty tunnel was 0.25 m/s, close to that (0.26 m/s) observed experimentally. The critical velocity in an empty tunnel for

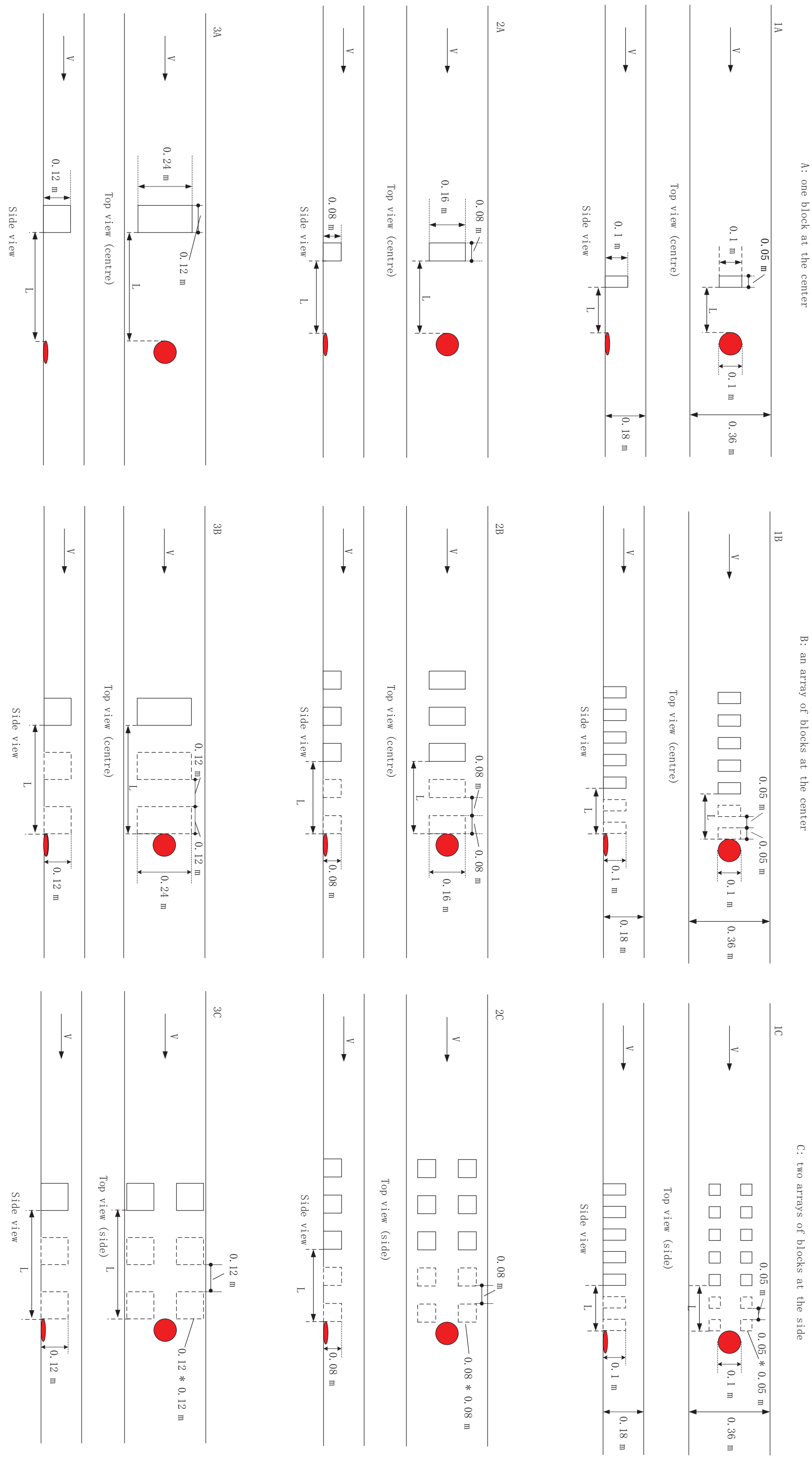
A: one block at the center
B: an array of blocks at the center
C: two arrays of blocks at the side
1A
1B
1C
2A
2B
2C
3A
3B
3C
Top view (centre)
Top view (side)
Side view
V
L
0.05 m
0.1 m
0.36 m
0.18 m
0.08 m
0.16 m
0.12 m
0.24 m
0.05 * 0.05 m
0.08 * 0.08 m
0.12 * 0.12 m

Fig. 6.3 The block locations in the experiment. Three different sizes of blocks (block1 $\psi = 0.15$, block2 $\psi = 0.19$, and block3 $\psi = 0.43$) were used. In configuration A, one block was placed at the center; in configuration B, one array of blocks were placed at the center; in configuration C, two arrays of blocks were placed at the side.

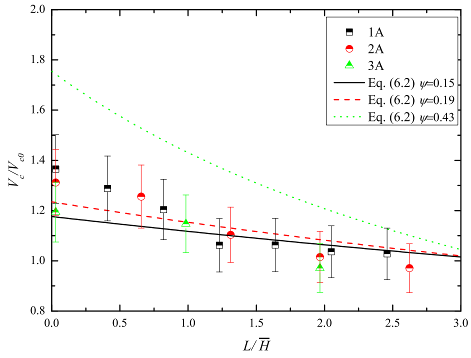

Fig. 6.4 Effect of the fire-blockage distance for configuration A (one block at the center); comparing experiments with Eq. (6.2) by Tang et al. (2013).

the 0.25 kW source (small fire) is 0.25 m/s (same as the hot-air plume simulation) and for the 7.5 kW source (large fire) is 0.53 m/s.

6.4 Results

6.4.1 Experimental results

Figure 6.4 shows the non-dimensional critical velocity V_c/V_{c0} as a function of the non-dimensional fire-blockage distance $L/\overline{H}$ of one block placed at the centre upstream (configuration A) in the experiment and the comparison with Eq. (6.2). We observe the same trend between the experiment and Tang et al. (2013): as the fire-blockage distance becomes larger, the critical velocity attains its corresponding value in an empty tunnel. However, a large discrepancy between the experimental results and the prediction by Eq. (6.2) is found when the block is placed not far away from the source, especially for a large block. A possible explanation is related to a different blockage ratio: Tang et al. (2013) used a single blockage ratio of about 10%, whereas the blockage ratio is much larger in the present study. Photos of the flame shape in Tang et al. (2013) suggest that the influence of blocking on the critical velocity is mainly exerted through a local sheltering of the fire. At the same time, a large acceleration is achieved near the ceiling, which facilitates attaining locally the critical condition (see also the numerical study in Lee and Tsai (2012)). The changing ratio of the critical velocity depends on the relative effect of these two factors.

Lee and Tsai (2012) found that the distance between the fire and the block affected V_c only marginally, which contradicts our observations. The reason is that in Lee and Tsai (2012), the non dimensional distance $L/\overline{H}$ is always lower than 0.25, whereas in the present study we investigate the influence of the fire-blockage distance in a much wider range.

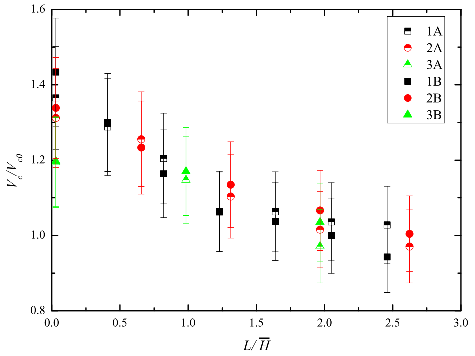

Fig. 6.5 Effect of the fire-blockage distance for one block (configuration A) and an array of blocks (configuration B) placed at the centre upstream the source.

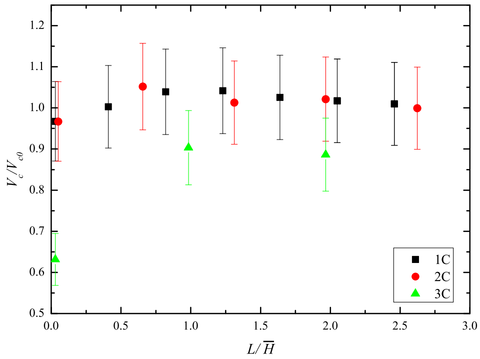

Fig. 6.6 Effect of the fire-blockage distance for two arrays of blocks placed at the sides upstream the source (configuration C).

Figure 6.5 shows the difference between one block (configuration A) and one array of blocks (configuration B) placed at the centre, upstream the source. No significant difference is found between the two sets of data, which suggests that only the block close to the source affects the critical velocity whereas the influence of the other blocks of the same size located further upstream is not relevant.

Figure 6.6 shows the effect of the fire-blockage distance for two arrays of blocks placed at the sides upstream the source (configuration C). In this case, the ventilation could reach the plume directly which implies a reduction of the critical velocity. Fig. 6.6 shows that when $L = 0$, for block1 (ψ=15%) and block2 (ψ=19%) the changing of critical velocity is negligible, whereas for large blocks (block3) the decreasing ratio of the critical velocity (37%) is close to the blockage ratio (43%), as suggested by Eq. (6.1).

Figure 6.7 shows the experimental results for $L = 0$ (i.e. for a block located just upstream the source), along with the data from a similar study, Rojas Alva et al. (2017). Good agreement has been achieved between the two data-sets for both conditions (obstructed and non-obstructed). For non-obstructed case, the data follows Eq. (6.1), although the value is

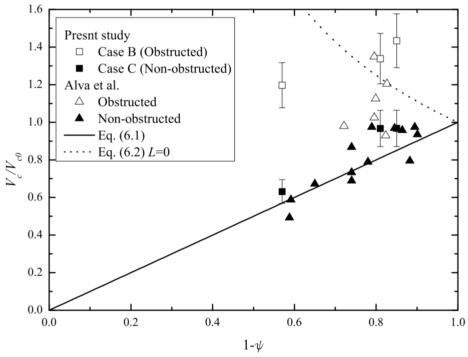

Fig. 6.7 Non dimensional critical velocity V_c/V_{c0} as a function of 1-ψ. Data from the experimental results ($L = 0$) and from Rojas Alva et al. (2017). Solid line is from Eq. (6.1) and dot line is from Eq. (6.2) (putting $L = 0$)

slightly larger; for the obstructed case, V_c/V_{c0} is larger than 1, but the trend is very different from Eq. (6.2). The application of Eq. (6.2) to cases with large blockage ratio is therefore questionable.

6.4.2 Comparison with numerical results

Figure 6.8 shows the comparison between the experimental results and the numerical simulations of the hot-air plume for configuration B when the blocks are located at the centre (a) and configuration C, when the blocks are located at the sides (b). In (a), when the fire source is partially blocked, the critical velocity is larger, but when $L/\overline{H}$ is larger than unity, $V_c \to V_{c0}$. Generally, a good agreement between the experiment and the numerical simulations has been achieved. However, a discrepancy is found for $L = 0$ (numerical results are smaller). The reason might be that FDS could not properly model the recirculation flow downstream the block, which directly affects the trajectory and the entrainment of rising the buoyant plume. In Lee and Tsai (2012) and Li et al. (2012), the effect of the block just upstream the source on the critical velocity was not investigated, hence this phenomenon was not observed. In Fig. 6.8 (b), when the ventilation reaches the fire plume directly, the critical velocity is smaller. For large blocks (configuration C) when $L = 0$, the numerical result of the decreasing of V_c/V_{c0} (39%) is close to the result of the experiment (37%) and the blockage ratio (43%).

Figure 6.9 shows the temperature and the velocity fields of the hot-air plume in configuration B (blocks at the center) and configuration C (blocks at the sides) for block1 ($\psi = 15\%$) at the condition $L/\overline{H} = 0.4$. The ventilation velocity is 0.26 m/s. The temperature field for the two cases clearly shows that the backlayer is different even at a same blockage ratio but with a different relative position between the fire and the blocks. Looking at the velocity field, with blocks placed at the center, we observe a recirculation flow downstream the block, with

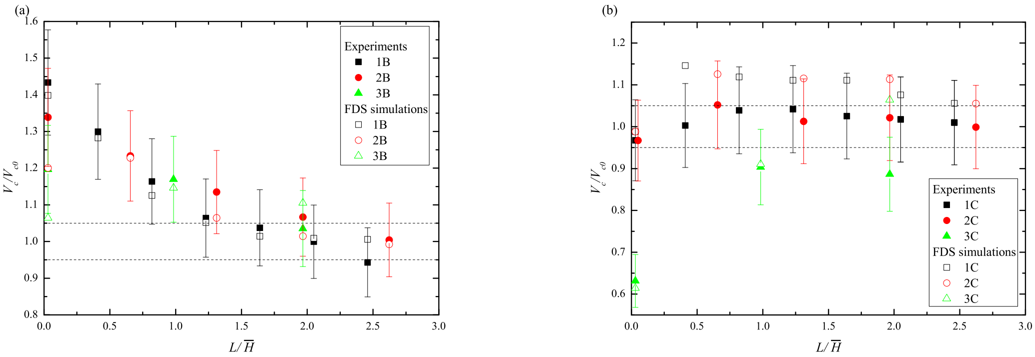

Fig. 6.8 Comparison between the experimental results and the numerical simulation of hot-air plume in case of the blocks located at the centre (configuration B) (a) and at the sides (configuration C) (b) of the tunnel.

a buoyant plume that raises almost vertically before being blown downstream. Although the ventilation flow is accelerated close to the ceiling, the critical ventilation velocity needed is larger compared to that in a corresponding empty tunnel. In case of blocks placed at the sides, the ventilation flow is accelerated, due to a decrease in the cross-section. The accelerated flow can reach the plume directly, and therefore a smaller critical velocity is needed. A ventilation velocity profile of the longitudinal velocity along height at 0.05 m before the source is shown in Fig. 6.10. For the case block1B ($\psi = 15\%$, blocks at the center) a recirculation bubble takes place close to the ground and the backlayer forms at the ceiling, suggesting that a larger ventilation is needed to obtain the critical condition. For the case of block1C ($\psi = 15\%$, blocks at the sides) the bulk flow is accelerated and no backlayer is detected.

Figure 6.11 shows the comparison between the experimental results and the numerical simulations of propane fire for configuration B when blocks are placed at the centre (a) and configuration C when the blocks are placed at the sides (b). For the small fire, only the cases close to the source were investigated, since it was found that when $L/\overline{H}$ is larger than unity, the change of the critical velocity is small. Numerical results are generally within the experimental uncertainties, which suggests that the blockage effect on the critical velocity is not directly affected by the fire source conditions. For configuration B (blocks at the center), as in the hot-air plume simulation, we observe a discrepancy between the experimental and numerical results when the fire-blockage distance L is small (numerical results are smaller). Fig. 6.12 shows the temperature and velocity fields in configuration B (blocks at the center) and configuration C (blocks at the sides) for block1 ($\psi = 15\%$) at the condition $L/\overline{H} = 0.4$ for large fire. Compared to the hot-air plume, the fire plume represents a volumetric source of buoyancy within the tunnel. Unlike the hot-air plume, which is deflected at the source position, the fire plume is displaced downstream while the combustion continues. Although

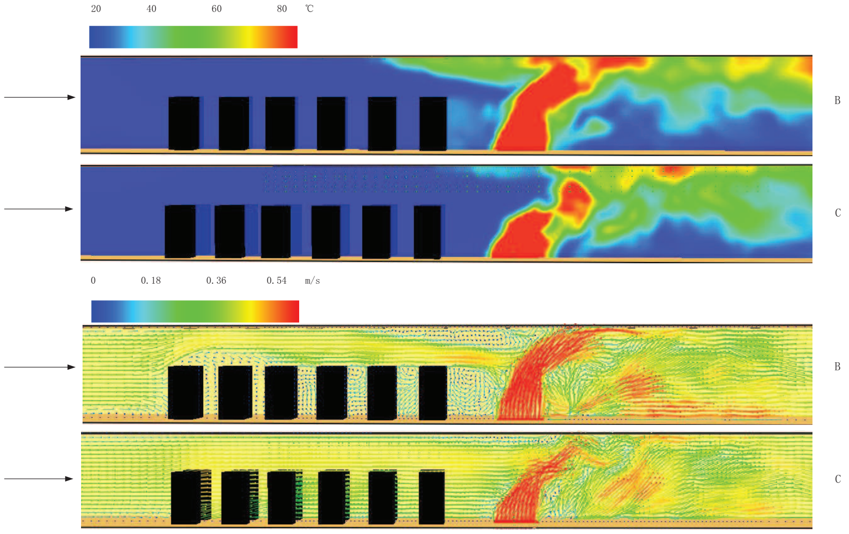

Fig. 6.9 Temperature and velocity fields of the hot-air plume in configuration B (blocks at the center) and configuration C (blocks at the side) for block1 (ψ=15%) at the condition $L/\overline{H} = 0.4$. The ventilation velocity is 0.26 m/s.

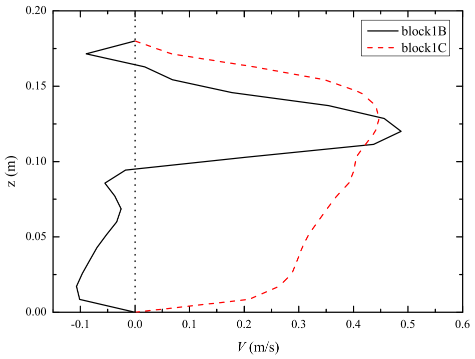

Fig. 6.10 Vertical velocity profiles of the longitudinal velocity at 0.05 m upstream the source (the same condition as Fig. 6.9).

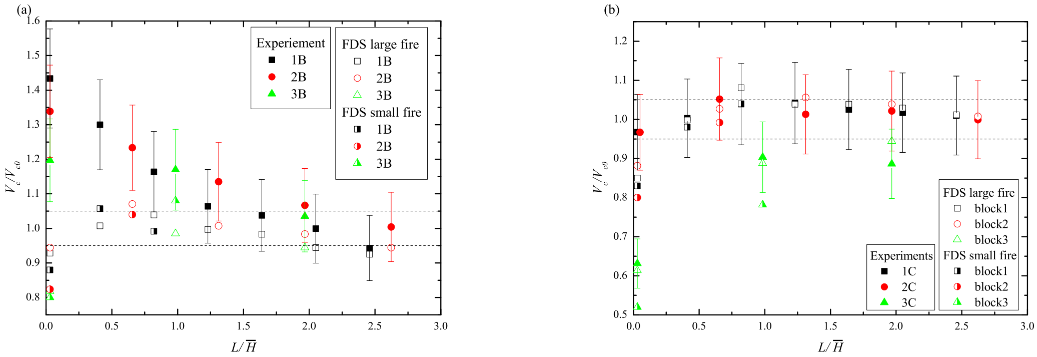

Fig. 6.11 Comparison between experimental results and numerical simulation of the propane fire (large fire at 7.5 kW and small fire at 0.25 kW) in case of blocks located at the centre (configuration B) (a) and the sides (configuration C) (b) of the tunnel.

different conditions of the source are observed between the hot-air plume simulations and the propane fire simulations, the critical velocity changing ratio is similar for the two kinds of simulations. Therefore, in a tunnel with a block, the critical velocity changing ratio seems to be only affected by the blocks rather than by the source condition.

6.5 Conclusions

We have investigated the influence of the presence of blocks on the critical velocity in a longitudinally ventilated tunnel. We focused on the influence of the blockage size, the fire-blockage distance and the relative position of the fire and the block. To that purpose, we have combined small-scale experiments on densimetric plumes (produced by the injection of light gases), and numerical simulations with the code FDS with hot-air plumes and propane fires. The results show the main following features:

- Results from configuration A (one block placed at the center) and configuration B (an array of blocks placed at the center) suggest that only the block close to the fire source affects the critical velocity, whereas the effect of other blocks of the same size located further upstream is negligible.
- The block affects the critical velocity only when it is placed close to source. When the non-dimensional fire-blockage distance $L/\overline{H}$ is larger than unity, the change in critical velocity becomes trivial.
- The relative position of the block and the fire source has a large influence on the critical velocity V_c, so that different V_c could be obtained even for a same blockage ratio. When

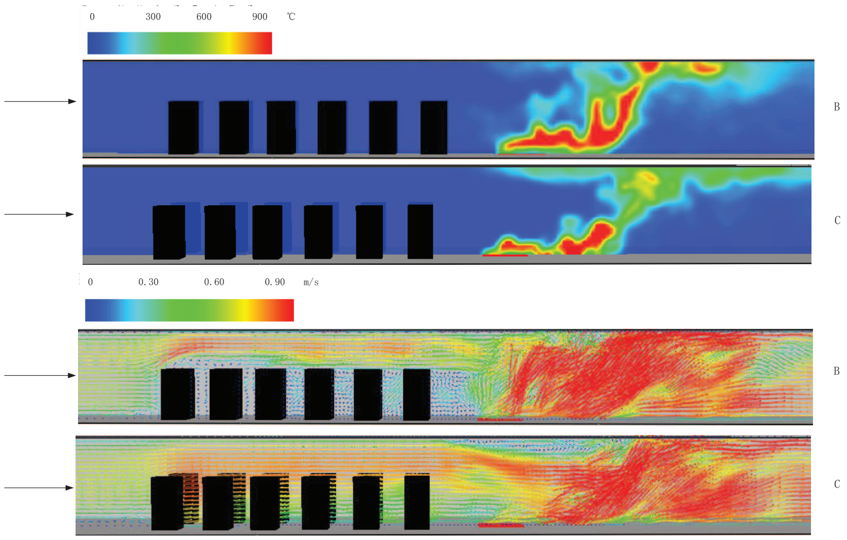

Fig. 6.12 Temperature and velocity fields of the large fire (7.5 kW) in configuration B (blocks at the center) and configuration C (blocks at the side) for block1 (ψ=15%) at the condition $L/\overline{H} = 0.4$. The ventilation velocity is 0.55 m/s.

the fire source is partially blocked and the ventilation flow cannot reach the fire plume directly, a larger V_c is needed compared with the case of a corresponding empty tunnel; when the ventilation flow can reach the fire directly, a smaller V_c is needed, and the reduction ratio is similar to the blockage ratio.

- Numerical simulations with hot-air plume and propane fire show good agreement with experiments with densimetric plumes when blocks are placed at the sides. However a discrepancy between the experimental and numerical data is found when the blocks are located at the centre upstream when the non-dimensional fire-blockage distance is small. The reason might be that the interaction between the recirculation flow (formed after block) and the plume makes the situation very complex.
- In the numerical simulations, while different flow behavior is observed between the hot-air plume and the propane fires, the critical velocity changing ratio is similar for the different source conditions. This suggests that the critical velocity changing ratio is mainly affected by the presence of blocks, whereas the effect of the source (buoyant plume, small or large fire) is small.

Chapter 7

Conclusions and Perspectives

Conclusions

In this thesis the critical velocity (a minimum ventilation velocity that prevents the smoke from flowing upstream the source) in longitudinal ventilated tunnels in case of a fire has been studied.

The fire is first modeled by a release of light gas in ambient air. In the experiments, the light fluid is an air/helium mixture. A theoretical model based on the classical plume study to investigate the critical velocity of a buoyant release has been proposed. The model depicts a buoyant plume rising from a circular source in a crossflow within a wide horizontal tunnel. In the experiments it was found that the behavior for momentum-driven and buoyancy-driven plumes was different. For momentum-driven plumes, the influence of the source radius and the non-Boussinesq effects (the effects due to large differences between the densities of the buoyant plume and the ambient fluid) are not negligible, and both the features can be well described by the model. For buoyancy-driven plumes, both the experiment and the model show that the non-Boussinesq effects are negligible. The experimental results are on one hand in a good agreement with the predictions of the theoretical model, on the other hand, they are also in good agreement with a simple scaling suitable for a line source of pure buoyancy.

Subsequently, the cause for the so-called ‘super-critical’ velocity in the tunnel fire study is discussed. This part combines the experimental study of densimetric plumes (air/helium mixture and hot-air) and the numerical study of propane fires. It was found that heat losses at the tunnel walls can induce a slight reduction in the critical velocity, but it cannot justify the appearance of the super-critical velocity. Small fires could be reliably modeled by densimetric plumes when these are not excessively momentum-driven. Large fires can no longer be modeled as localized buoyancy source but should be modeled as a distributed buoyancy source. The ‘super-critical’ velocity is caused by the downstream displacement of the volume distributed buoyancy source.

The tunnel inclination on the critical velocity is investigated in the third part. The influence of slope (defined as negative when the entrance of fresh air is at a lower elevation than the source) on the movement of smoke is mainly related to the role of the component of buoyancy along the tunnel axis. Compared to a horizontal tunnel, the critical velocity will be larger for positive slope (and smaller for negative slope). Our experiments and numerical simulations on densimetric plumes suggest that the dynamical condition at the source affects the critical velocity of a buoyant plume: when the buoyant plume is momentum-driven, the influence of slope is small; when the buoyant plume is buoyancy-driven, the influence of slope is large. A theoretical model (based on the previous model of the critical velocity in a horizontal tunnel) which gives a correlation for the critical velocity ratio V_c/V_{c0} (V_c and V_{c0} are critical velocities in an inclined and horizontal tunnel) can reliably reproduce these behaviors. An approximation of the model for a buoyancy-driven plume provides a correlation: $V_c/V_{c0} = \sqrt{1+C_k \sin\theta}$, C_k is a constant fitted from our experiment, which is independent of the buoyancy flux at the source for buoyancy-driven releases. For a volume distribute buoyancy source, i.e. a fire, numerical simulations suggest that the power of the fire has very little influence on the critical velocity ratio V_c/V_{c0}. Moreover, the results of the fire simulations show a similar trend with buoyancy-driven releases and can be well fitted by the correlation provided by the model.

The final part of the thesis focuses on the effect of vehicle blockage on the critical velocity, experimentally and numerically. The vehicles are modeled by blocks of different sizes placed upstream of the buoyancy or fire source. Some important parameters, such as the tunnel blockage ratio, the fire-blockage distance and the relative position of the fire and the block, are investigated. The similar results obtained when putting one block and an array of blocks of the same size at the center (laterally) upstream the source suggest that only the block close to fire source affects critical velocity, whereas the effect of other blocks located further upstream is negligible. As the fire-blockage distance becomes larger, the critical velocity changes and becomes close to the value in an empty tunnel. The relative position of the block and the fire source has large influence on the critical velocity. When the blocks are placed at the center laterally, the source is partly protected. In this situation the ventilation flow does not directly impinge on the fire plume and the critical velocity is increased comparing with the case in an empty tunnel. On the other hand, when the block is placed at the sides laterally, the ventilation flow directly reaches the fire plume and the critical velocity is then observed lower than that in an empty tunnel. The reduction ratio of the critical velocity is similar to the reduction in cross-section of the tunnel induced by the presence of the block, which is attributed to the fact that the block induces an increase in the local ventilation velocity thus promoting the downstream plume thrust. On the contrary, when the block protects the source, the local ventilation velocity is zero at the source and is increased where the plume is not present, thus causing an increase in the critical velocity. Similar results are obtained between the buoyant plumes and the propane fires, which suggests that the variation of the critical velocity ratio (ratio between the case with blocks and that in an empty tunnel) is mainly affected by the blocks, whereas the effect of the source condition (buoyant plume, small or large fire) is small.

Perspectives

Smoke control in case of a fire in a tunnel can be achieved by mechanical ventilation. One simple strategy is to provide the tunnel with a longitudinal ventilation flow, which is discussed in the present study. Based on the results obtained in this simple configuration, more sophisticated strategies could be investigated. Here we introduce two other strategies: one is to add movable screens at the tunnel ceiling; the other is to develop a transverse system (see Fig 1.2).

In the first strategy, when the fire starts in a tunnel, the nearby screens are activated, providing a barrier to retard the smoke flowing to other places. Combining this strategy with longitudinal ventilation, a much smaller ventilation velocity would be needed to prevent the smoke from flowing upstream, since a large proportion of the smoke is blocked near the ceiling. To obtain a good design, the size of the screen and the distance between two screens needs to be investigated.

In the second strategy, when the fire starts in a tunnel, the nearby fans are activated, creating air flow to extract the smoke out of the tunnel directly. Compared with the longitudinal ventilation strategy, this strategy requires to detect the location of the fire source, which requires a corresponding fire detection system to be built. During the fire control operation, the extraction fans must be powerful enough to create longitudinal flows from both sides to confine the smoke between the vents and the fire source. Operationally, jet fans installed beneath the ceiling could be operated together with the extraction vents to produce the longitudinal flows to suppress smoke from spreading. To design an effective system, the power of the extraction fans and the distance between two fans needs to be decided. The longitudinal ventilation study presented in this thesis could provide some preliminary information for the longitudinal flow needed to confine the smoke.

Appendix A

Introduction of the numerical simulation

A.1 Introduction

A.1.1 Navier-Stokes equations at low-Mach number

General form of the equations

The dynamic and thermodynamical condition of a fluid are fully modelled by the following system of equations:

$$\begin{cases} \dfrac{\partial \rho}{\partial t} + \dfrac{\partial \rho u_i}{\partial x_j} = 0, & \text{(A.1a)} \\ \dfrac{\partial \rho u_i}{\partial t} + \dfrac{\partial \rho u_i u_j}{\partial x_j} = -\dfrac{\partial \rho}{\partial x_i} + \dfrac{\partial \tau_{ij}}{\partial x_j} + \rho g_i, & \text{(A.1b)} \\ \dfrac{\partial \rho h}{\partial t} + \dfrac{\partial \rho u_j h}{\partial x_j} = \dfrac{\mathrm{d}p}{\mathrm{d}t} + \tau_{ij} \dfrac{\partial u_i}{\partial x_j} - \dfrac{\partial q_i}{\partial x_i} + S. & \text{(A.1c)} \end{cases}$$

where x is the vector position, $\mathbf{u}(\mathrm{x},t)$ is the velocity field, $\rho(\mathrm{x},t)$ is the density field, t is the time, p is the pressure, τ_{ij} is the tensor of viscous stresses, h is the internal enthalpy, q_i is the diffusive heat flux and S is the heat sources. The relationship between the mass enthalpy of a small fluid element ($\mathscr{H}(\mathrm{x},t)$) and the internal enthalpy is:

$$h = \mathscr{H} - \frac{1}{2} u_i u_i \tag{A.2}$$

In case of a Newtonian fluid, the diffusive heat flux and viscous stresses tensor can be written as:

$$\begin{cases} q_i = -\rho c'_p k \dfrac{\partial T}{\partial x_i}, & \text{(A.3a)} \\ \tau_{ij} = \mu \left(\dfrac{\partial u_i}{\partial x_j} + \dfrac{\partial u_j}{\partial x_i} \right) + \mu' \dfrac{\partial u_k}{\partial x_k} \delta_{ij}. & \text{(A.3b)} \end{cases}$$

with k the diffusivity, T the temperature, $\mu = \rho \nu$ the dynamic viscosity and ν the kinematic viscocity, and δ_{ij} the Kronecker symbol:

$$\delta_{ij} = \begin{cases} 1 & \text{for} \quad i = j, \\ 0 & \text{for} \quad i \neq j. \end{cases} \tag{A.4}$$

The second dynamic viscosity, μ', is related to the first by $\mu' \approx -\frac{2}{3}\mu$. The modified specific heat c'_p, is related to the specific heat of gas, c_p, by the following relationship:

$$c'_p = \frac{\int_{T_{ref}}^{T} c_p(T') dT'}{T - T_{ref}} \tag{A.5}$$

where T_{ref} is reference temperature.

The Sutherland formula can be used to calculate the value of the dynamic viscosity as a function of the temperature:

$$\mu = \mu_0 \sqrt{\frac{T}{T_0}} \frac{1 + \frac{C_\mu}{T_0}}{1 + \frac{C_\mu}{T}} \tag{A.6}$$

where the subscript ‘0’ corresponds to a reference value and C_μ, equals to 123.6 K in dry air.

The equations of ideal gas write:

$$\begin{cases} h(T) = c'_p(T) \times (T - T_0), & \text{(A.7a)} \\ p = \rho \dfrac{R}{M} T. & \text{(A.7b)} \end{cases}$$

with R the universal constant of ideal gas and M the molar mass of the gas considered.

Low Mach number approximation

By injecting Eq. (A.7a) into the enthalpy (Eq. A.1c) and use the mass conservation equation, one can have:

$$\frac{\partial c'_p \rho T}{\partial t} + \frac{\partial c'_p \rho T u_j}{\partial x_j} = \frac{Dp}{Dt} + \tau_{ij} \frac{\partial u_i}{\partial x_j} - \frac{\partial q_i}{\partial x_i} + S \tag{A.8}$$

with the derivative $\frac{Dp}{Dt} = \frac{\partial p}{\partial t} + u_j \frac{\partial p}{\partial x_j}$. Assuming a low-Mach number, the ideal gas law (Eq. A.7b) can be written as:

$$\rho T = \rho_0 T_0 \tag{A.9}$$

where ρ_0 and T_0 are a density and a reference temperature, respectively. Assuming Eq. (A.9), Eq. (A.8) reduces to:

$$\frac{\partial u_j}{\partial x_j} = -\frac{1}{c'_p}\frac{Dc'_p}{Dt} + \frac{1}{c'_p \rho_0 T_0}\left(\frac{Dp}{Dt} + \tau_{ij}\frac{\partial u_i}{\partial x_j} - \frac{\partial q_i}{\partial x_i} + S\right) \tag{A.10}$$

By analyzing the Eq. (A.10), we realize that the divergence of the velocity is equal to the sum of five terms. After assessing the order of quantity of each term on the right side of A.10 (see (Carlotti, 2013) for more detail), the equation of enthalpy reduces to:

$$\frac{\partial u_j}{\partial x_j} = -\frac{1}{c'_p}\frac{Dc'_p}{Dt} + \frac{1}{c'_p \rho_0 T_0}\left[\frac{\partial}{\partial x_i}\left(\rho c'_p \kappa \frac{dT}{dx_i}\right) + S\right] \tag{A.11}$$

Final form of the system of equations

In a general way, the pressure can be decomposed in its hydrostatic and hydrodynamic (refered to as p_d) components:

$$p(x,y,z,t) = p_0 + \rho_0 g_i (x_i - x_i^0) + p_d \tag{A.12}$$

where $p_0(t)$ is the reference pressure at a fixed point of the flow.

Using the decomposition of the pressure by Eq. (A.12) in the set of equations A.1, we obtain the final system of the Navier-Stokes equations:

$$\begin{cases} \frac{\partial \rho}{\partial t} + \frac{\partial \rho u_j}{\partial x_j} = 0, & \text{(A.13a)} \\ \frac{\partial \rho u_i}{\partial t} + \frac{\partial \rho u_i u_j}{\partial x_j} = -\frac{\partial p_d}{\partial x_i} + \frac{\partial}{\partial x_j}\left(\rho \nu \frac{\partial u_i}{\partial x_j}\right) + (\rho - \rho_0) g_i, & \text{(A.13b)} \\ \frac{\partial u_j}{\partial x_j} = -\frac{1}{c'_p}\frac{Dc'_p}{Dt} + \frac{1}{c'_p \rho_0 T_0}\left[\frac{\partial}{\partial x_i}\left(\rho c'_p \kappa \frac{\partial T}{\partial x_i}\right) + S\right], & \text{(A.13c)} \\ \rho T = \rho_0 T_0. & \text{(A.13d)} \end{cases}$$

A.1.2 Poisson equation on the pressure

By dividing the momentum equation (Eq. A.13b) by the density, ρ, rearranging the equation and taking its divergence, we have:

$$\frac{\partial}{\partial x_i}\left(\frac{1}{\rho}\frac{\partial p_d}{\partial x_i}\right) = -\frac{\partial}{\partial t}\left(\frac{\partial u_i}{\partial x_i}\right) - \frac{\partial}{\partial x_i}\left(u_j\frac{\partial u_i}{\partial x_j}\right) + \frac{\partial}{\partial x_i}\left[\frac{1}{\rho}\frac{\partial}{\partial x_j}\left(\rho\nu\frac{\partial u_i}{\partial x_j}\right)\right] + g_i\frac{\partial}{\partial x_i}\left(\frac{\rho-\rho_0}{\rho}\right) \quad \text{(A.14)}$$

This equation constitutes the Poisson equation. However, because of the left side, corresponding to the variable coefficients $\frac{\partial}{\partial x_i}\left(\frac{1}{\rho}\frac{\partial}{\partial x_i}\right)$, the numerical resolution methods are inefficient, thus increasing the computation time. We would therefore like to replace the term $\frac{1}{\rho}\frac{\partial p_d}{\partial x_i}$ with an expression that is a gradient.

Term $\frac{1}{\rho}\frac{\partial p_d}{\partial x_i}$ is then replaced with the sum of a gradient and a corrective term that can be included in the Poisson equation as a perturbation. This corrective term should be as small as possible and easy to calculate, such as:

$$\frac{1}{\rho}\text{grad}(p_d) = \text{grad}(H) + \underline{V} \quad \text{and} \quad \underline{V} \quad \text{small} \quad \text{(A.15)}$$

Several solutions are possible, but the version 6 of FDS arbitrarily chooses H, implying that $\underline{V} = \frac{1}{\rho}\text{grad}(p_d) - \text{grad}(H)$ and verifies that $\underline{V}$ is small. The solution proposed by FDS6 is:

$$\frac{1}{\rho}\text{grad}(p_d) = \text{grad}\left(\frac{p'}{\rho}\right) - p_d\text{grad}\left(\frac{1}{\rho}\right) \quad \text{(A.16)}$$

where p_d is a priori small.

With this solution, the Poisson equation becomes:

$$\frac{\partial^2(p_d/\rho)}{\partial x_i\partial x_i} = -\frac{\partial}{\partial x_i}\left(p_d\frac{\partial(1/\rho)}{\partial x_i}\right) - \frac{\partial}{\partial t}\left(\frac{\partial u_i}{\partial x_i}\right) - \frac{\partial}{\partial x_i}\left(u_j\frac{\partial u_i}{\partial x_j}\right) + \frac{\partial}{\partial x_i}\left[\frac{1}{\rho}\frac{\partial}{\partial x_j}\left(\rho\nu\frac{\partial u_i}{\partial x_j}\right)\right] + g_i\frac{\partial}{\partial x_i}\left(\frac{\rho-\rho_0}{\rho}\right) \quad \text{(A.17)}$$

This last formulation of Poisson equation allows p_d to be computed, by the numerical methods.

A.1.3 Turbulence modeling

Most flows of interest in fire engineering and tunnel building ventilation are turbulent. However, the domains to be meshed are generally very large, and preclude using Direct Numerical Simulation (DNS), which would require a mesh size smaller than the smallest turbulence scales (Kolmogorov scale, η_t). We must therefore model the turbulence. For this, two types of approaches are possible: the Reynolds-Averaged Navier–Stokes (RANS) or the Large Eddy Simulation (LES). RANS simulations decompose the instantaneous quantities into an average quantity and its fluctuation according to the Reynolds decomposition. For a quantity f, we have:

$$f = < f > + f' \tag{A.18}$$

where f' represents the fluctuations of f around its temporal average $< f >$.

The principle of the LES is to use a filter on the Navier-Stokes equations, which will eliminate small scales fluctuations. The large eddies of the flow are then simulated and the smaller are modeled by a subgrid model. This approach is based on the assumption that, in a turbulent flow, the large vortex structures are mostly responsible for the transport of energy and the momentum. The result of the filter of a quantity f is $\overline{f}$:

$$\overline{f}(\underline{x}) = \frac{1}{L_f} \int f(\underline{r}) \cdot \chi \left(\frac{\underline{x} - \underline{r}}{L_f} \right) d\underline{r} \tag{A.19}$$

with L_f the filter scale and χ a function defined in $\mathbf{R}^3$, of integral 1, which is 1 in the center and is negligible outside $[-1,1]^3$. Thus, when $L_f \to 0$, we have that $\overline{f} \to f$. For more details on the average Reynolds and the filters, the reader is referred to Pope (2000).

Applying the above filter and decomposing the quantity f as $f = \overline{f} + f_{sgs}$, with f_{sgs} the unresolved quantity (called the subgrid) that has to be modeled, the set of equations A.13 can be rewritten:

$$\left\{ \begin{aligned}
&\frac{\partial \overline{\rho}}{\partial t} + \frac{\partial \overline{\rho u_j}}{\partial x_j} = 0, && \text{(A.20a)}\\
&\frac{\partial \overline{\rho u_i}}{\partial t} + \frac{\partial \overline{\rho u_i u_j}}{\partial x_j} = -\frac{\partial \overline{p_d}}{\partial x_i} + \frac{\partial}{\partial x_j} \overline{\left(\rho \nu \frac{\partial u_i}{\partial x_j} \right)} + (\overline{\rho} - \rho_0) g_i, && \text{(A.20b)}\\
&\frac{\partial \overline{u_j}}{\partial x_j} = -\overline{\frac{1}{c'_p} \frac{Dc'_p}{Dt}} + \overline{\frac{1}{c'_p \rho_0 T_0} \left[\frac{\partial}{\partial x_i} \left(\rho c'_p \kappa \frac{dT}{dx_i} \right) + S \right]}, && \text{(A.20c)}\\
&\overline{\rho T} = \rho_0 T_0. && \text{(A.20d)}
\end{aligned} \right.$$

Favre filtering

At constant density, the only cross terms in Eq. (A.20) are $\overline{u_i u_j}$. For a variable density, new cross terms appear: $\overline{\rho f}$ with $f = u_i$ and $f = u_i u_j$. In order to take these terms into account it is customary to introduce the Favre filtering, defined as:

$$\widetilde{f} = \frac{1}{\overline{\rho}} \cdot \overline{\rho f} \tag{A.21}$$

The Favre filter of one of the components of the velocity is then:

$$\widetilde{u_i} = \frac{1}{\overline{\rho}} \cdot \overline{\rho u_i} \tag{A.22}$$

The Favre filter of the density is $\widetilde{\rho} = \overline{\rho}$. Given that $\rho T = \rho_0 T_0$, we also have $\widetilde{T} = \frac{\rho_0}{\overline{\rho}} \cdot T_0$, i.e.:

$$\widetilde{\rho}\widetilde{T} = \rho_0 T_0 \tag{A.23}$$

By applying the Favre filter to equations A.20, we obtain:

$$\begin{cases} \dfrac{\partial \widetilde{\rho}}{\partial t} + \dfrac{\partial \widetilde{\rho} \cdot \widetilde{u_j}}{\partial x_j} = 0, & \text{(A.24a)} \\ \dfrac{\partial \widetilde{\rho} \cdot \widetilde{u_i}}{\partial t} + \dfrac{\partial \widetilde{\rho} \cdot \widetilde{u_i u_j}}{\partial x_j} = -\dfrac{\partial \overline{p_d}}{\partial x_i} + \dfrac{\partial}{\partial x_j} \overline{\left(\rho \nu \dfrac{\partial u_i}{\partial x_j} \right)} + \widetilde{\rho} g_i, & \text{(A.24b)} \\ \dfrac{\partial \overline{u_j}}{\partial x_j} = -\overline{\dfrac{1}{c'_p} \dfrac{Dc'_p}{Dt}} + \overline{\dfrac{1}{c'_p \rho_0 T_0} \left[\dfrac{\partial}{\partial x_i} \left(\rho c'_p \kappa \dfrac{dT}{dx_i} \right) + S \right]}. & \text{(A.24c)} \end{cases}$$

We define ρ' the fluctuations of ρ at a fixed point, so $\rho(t) = \overline{\rho}(t) + \rho'(t)$. We then obtain: $\widetilde{u} = \overline{u} + \frac{1}{\overline{\rho}} \overline{\rho' u}$. Moreover, by defining $u_i = \widetilde{u_i} + u'_i$, we have:

$$\overline{\frac{1}{c'_p} \frac{Dc'_p}{Dt}} = \overline{\frac{T}{c'_p} \frac{Dc'_p}{DT}} \times \frac{\partial \widetilde{u}_j}{\partial x_j} + \overline{\frac{T}{c'_p} \frac{Dc'_p}{DT} \times \frac{\partial u'_j}{\partial x_j}} \tag{A.25}$$

The set of equations A.24 can then be rewritten as:

$$\begin{cases}
\dfrac{\partial \widetilde{\rho}}{\partial t} + \dfrac{\partial \widetilde{\rho} \cdot \widetilde{u_j}}{\partial x_j} = 0, & \text{(A.26a)} \\[2ex]
\dfrac{\partial \widetilde{\rho} \cdot \widetilde{u_i}}{\partial t} + \dfrac{\partial \widetilde{\rho} \cdot \widetilde{u_i} \cdot \widetilde{u_j}}{\partial x_j} = -\dfrac{\partial \overline{p_d}}{\partial x_i} + \dfrac{\partial}{\partial x_j} \overline{\left(\rho \nu \dfrac{\partial u_i}{\partial x_j} \right)} + \widetilde{\rho} g_i - \dfrac{\partial \widetilde{\rho} \cdot R_{ij}}{\partial x_j}, & \text{(A.26b)} \\[2ex]
\left(1 + \overline{\dfrac{T}{c'_p} \dfrac{c'_p}{DT}} \right) \dfrac{\partial \widetilde{u_j}}{\partial x_j} = -\dfrac{\partial M_j}{\partial x_j} - \overline{\dfrac{1}{c'_p} \dfrac{Dc'_p}{Dt} \times \dfrac{\partial u'_j}{\partial x_j}} & \\
\qquad + \overline{\dfrac{1}{c'_p \rho_0 T_0} \left[\dfrac{\partial}{\partial x_i} \left(\rho c'_p \kappa \dfrac{dT}{dx_i} \right) + S \right]}. & \text{(A.26c)}
\end{cases}$$

with

$$R_{ij} = \widetilde{u'_i u'_j} \quad ; \quad M_j = \frac{1}{\widetilde{\rho}} \overline{\rho' u'_j} \tag{A.27}$$

The diffuse terms of the equations A.26b and A.26c could be simplified as:

$$\begin{cases}
\overline{\left(\rho \nu(T) \dfrac{\partial u_i}{\partial x_j} \right)} \approx \widetilde{\rho} \cdot \nu(\overline{T}) \dfrac{\partial \widetilde{u_i}}{\partial x_j}, & \text{(A.28a)} \\[2ex]
\overline{\dfrac{1}{c'_p \rho_0 T_0} \left[\dfrac{\partial}{\partial x_i} \left(\rho c'_p \kappa(T) \dfrac{\partial T}{\partial x_i} \right) + S \right]} = \dfrac{1}{c'_p \rho_0 T_0} \left[\dfrac{\partial}{\partial x_i} \left(\widetilde{\rho} \overline{c'_p} \kappa(\overline{T}) \dfrac{\partial \widetilde{T}}{\partial x_i} \right) + S \right] & \text{(A.28b)}
\end{cases}$$

In fact, by developing the diffusive term of Eq. (A.26b) with the relationship $u_i = \widetilde{u_i} + u'_i$, it becomes:

$$\overline{\left(\rho \nu(T) \frac{\partial u_i}{\partial x_j} \right)} = \widetilde{\rho} \nu(\overline{T}) \frac{\partial \widetilde{u_i}}{\partial x_j} + \widetilde{\rho} [\widetilde{\nu(T)} - \nu(\overline{T})] \frac{\partial \widetilde{u_i}}{\partial x_j} + \overline{\rho \nu \frac{\partial u'_i}{\partial x_j}} \tag{A.29}$$

In the right-hand side, the second and third terms are small compared with the first one. The same approach is used for the terms in Eq. (A.26c).

The term representing the variation of specific heat in the left hand side of Eq. (A.26c) is often represented in the form (see (Carlotti, 2013)):

$$\overline{\frac{T}{c'_p(T)} \frac{Dc'_p}{DT}(T)} \approx \frac{T}{c'_p(\overline{T})} \frac{Dc'_p}{DT}(\overline{T}) \tag{A.30}$$

By taking these simplifications into account, the set of equations (A.26) can be rewritten:

$$\begin{cases} \dfrac{\partial \widetilde{\rho}}{\partial t} + \dfrac{\partial \widetilde{\rho} \cdot \widetilde{u_j}}{\partial x_j} = 0, & \text{(A.31a)} \\ \dfrac{\partial \widetilde{\rho} \cdot \widetilde{u_i}}{\partial t} + \dfrac{\partial \widetilde{\rho} \cdot \widetilde{u_i} \widetilde{u_j}}{\partial x_j} = -\dfrac{\partial \overline{p_d}}{\partial x_i} + \dfrac{\partial}{\partial x_j}\left(\widetilde{\rho} \nu(\overline{T}) \dfrac{\partial \widetilde{u_i}}{\partial x_j} \right) + \widetilde{\rho} g_i - \dfrac{\partial \widetilde{\rho} \cdot R_{ij}}{\partial x_j}, & \text{(A.31b)} \\ \left(1 + \dfrac{T}{c'_p \overline{T}} \dfrac{D c'_p}{DT}(\overline{T}) \right) \dfrac{\partial \widetilde{u_j}}{\partial x_j} = -\dfrac{\partial M_j}{\partial x_j} & \\ \quad + \dfrac{1}{c'_p(\overline{T}) \rho_0 T_0} \left[\dfrac{\partial}{\partial x_i} \left(\widetilde{\rho} c'_p(\overline{T}) \kappa(\overline{T}) \dfrac{\partial (\overline{T})}{\partial x_i} \right) + S \right]. & \text{(A.31c)} \end{cases}$$

Only the following two terms are unknown and require a closure assumptions:

$$R_{ij} = \widetilde{u'_i u'_j} \quad ; \quad M_j = \frac{1}{\widetilde{\rho}} \overline{\rho' u'_j}$$

Closure of the equations

In order to close the system of equations A.31, we must make an hypothesis, known as ‘Boussinesq assumption’, and introduce a turbulent viscosity ν_t. The terms R_{ij} and M_j can then be written:

$$-R_{ij} = \nu_t \left(\frac{\partial \overline{u_i}}{\partial x_j} + \frac{\partial \overline{u_j}}{\partial x_i} - \frac{2}{3} \frac{\partial \overline{u_k}}{\partial x_k} \delta_{ij} \right) \quad \text{and} \quad M_j = -\frac{1}{T_0} D_s \frac{\partial \overline{T}}{\partial x_j} \tag{A.32}$$

with

$$D_s = \frac{\nu_t}{Pr_t} \tag{A.33}$$

where Pr_t is the turbulent Prandtl number. The FDS code sets a default value at 0.5, but it can be changed by the user.

Among all of the turbulent viscosity models, we focus here on the four subgrid models implemented in FDS6: Smagorinsky constant, Smagorinsky dynamic, Deardorff and Vreman.

Constant Coefficient Smagorinsky Model In the Smagorinsky model the eddy viscosity ν_t is expressed as:

$$\begin{cases} \nu_t = (C_s L_f)^2 |S|, & \text{(A.34a)} \\ |S| = \left(2 S_{ij} S_{ij} - \frac{2}{3} \left(\frac{\partial \overline{u_i}}{\partial x_i} \right)^2 \right)^{1/2}, & \text{(A.34b)} \\ S_{ij} = \frac{1}{2} \left(\frac{\partial \overline{u_i}}{\partial x_j} + \frac{\partial \overline{u_j}}{\partial x_i} \right). & \text{(A.34c)} \end{cases}$$

where C_s is the empirical Smagorinsky constant (generally assumed to equal to 0.2) and $L_f = (\delta x \delta y \delta z)^{1/3}$ the scale of the filter (proportional to the mesh size).

Dynamic Smagorinsky Model Differently from the constant coefficient Smagorinsky model, the coefficient C_s of equations (A.34) is not assumed to be a constant, and is computed from the flow conditions at each time step, by two successive filters. The first is the grid filter, the second is the test filter. The test filter width is assumed to be larger than the grid filter width.

Deardorff's Model The principle of the Deardorff's model consists in modeling the turbulent viscosity ν_t by the subgrid kinetic energy, E_{ksgs}:

$$\nu_t = C_D L_f \sqrt{E_{ksgs}} \tag{A.35}$$

where C_D is a model constant.

The subgrid kinetic energy can be calculated by different methods. FDS6 models it as:

$$E_{ksgs} = \frac{1}{2} \left((\overline{u} - \hat{u})^2 + (\overline{v} - \hat{v})^2 + (\overline{w} - \hat{w})^2 \right) \tag{A.36}$$

where $\overline{u}$ is the average value of u at the grid cell center and $\hat{u}$ is the weighted average of u over the adjacent cells. Their respective equations are:

$$\begin{cases} \overline{u}_{ijk} = \frac{u_{ijk} + u_{i-1,jk}}{2}, & \text{(A.37a)} \\ \hat{u}_{ijk} = \frac{\overline{u}_{ijk}}{2} + \frac{\overline{u}_{i-1,jk} + \overline{u}_{i+1,jk}}{4} & \text{(A.37b)} \end{cases}$$

The terms $\overline{v}$, $\hat{v}$, $\overline{w}$ and $\hat{w}$ are defined similarly. The model constant is generally set to 0.1.

Vreman's Model The Vreman's model (Vreman (2004)) is conceived in order to have a zero turbulent viscosity ($\nu_t = 0$) when the norm of the velocity gradient zero ($\psi_{ij}\psi_{ij} = 0$). In this model, the turbulent viscosity is modeled by:

$$\nu_t = C_V \sqrt{\frac{\Phi_\beta}{\psi_{ij}\psi_{ij}}} \tag{A.38}$$

with

$$\begin{cases} \Phi_\beta = \beta_{11}\beta_{22} - \beta_{12}^2 + \beta_{11}\beta_{33} - \beta_{13}^2 + \beta_{22}\beta_{33} - \beta_{23}^2, & \text{(A.39a)} \\ \beta_{ij} = \Delta_m^2 \psi_{mi}\psi_{mj}, & \text{(A.39b)} \\ \psi_{ij} = \dfrac{\partial u_j}{\partial x_i}. & \text{(A.39c)} \end{cases}$$

The Vreman constant, C_V, is dependent on the Smagorinsky model by the following relation: $C_V \approx 2.5C_S^2$. However, during the validation phase of FDS, the developers found that a Smagorinsky constant equal to 0.17 gave better results. The Vreman constant is thus fixed by default to $C_V = 0.07$ (but it can also be modified by the user).

A.1.4 Simulation software: Fire Dynamics Simulator

The numerical tool that was chosen to simulate the plumes during this thesis is the three-dimensional code Fire Dynamics Simulator (FDS). This part presents a general presentation of the software, describes the different physical models, focusing on the case of fire plumes.

General presentation of the software

FDS is a Computational Fluid Dynamic (CFD) software, suitable for low-Mach number flows, with a focus on the heat transfer and smoke from fires. It is supplied with a three-dimensional visualization software called Smokeview and with *fds2ascii* which allows a post-processing of the simulated data. FDS, Smokeview and *fds2ascii* are developed by the National Institute of Standards and Technology (NIST) in the United States and VTT Center in Finland. Several other collaborators around the world are involved in the improvement of the code. To date, FDS 6.5.3 is the latest version available to the public.

FDS solves the Navier-Stokes equations presented in the previous sections in DNS or LES, with a discretization of these equations by finite differences. It uses a scheme of explicit predictor-corrector, second-order accuracy in time and space, and solve the Poisson equation by Fast Fourier Transformation - (FFT).

Different physical models

The FDS code uses many turbulence models, the combustion or the thermal exchanges. This part presents the models of subgrid and heat exchanges.

Subgrid Models As explained in the previous section, to close the system of equations A.31, one needs to model the turbulent viscosity ν_t. For this, FDS offers four subgrid models: Smagorinsky constant, Smagarinsky dynamic, Deardoff and Vreman. These models have already been presented in section A.1.3.

The other diffusive parameters, the thermal conductivity (λ_{kt}) and the diffusivity of the materials (κ) are related to the turbulent viscosity by:

$$\lambda_{kt} = \frac{\rho \nu_t c_p}{Pr_t} \quad ; \quad (\rho \kappa)_t = \frac{\rho \nu_t}{Sc_t} \tag{A.40}$$

where the turbulent Prandtl number Pr_t and the turbulent Schmidt number Sc_t are considered as constant for a given scenario. By default, these numbers are equal to $Pr_t = 0.5$ and $Sc_t = 0.5$. Both can be modified by the user.

Heat exchanges Models This sub-section presents the different ways of modeling thermal conduction within solids, as well as heat exchanges at the walls.

The conduction within solids FDS assumes that the solids consist of several layers. Each layer is made up of several materials which can undergo different thermal degradation reactions. These reactions form products of chemical reactions such as water vapor and/or combustion products. FDS uses a model for the conduction of heat in solids, which is unidirectional (1D) and perpendicular to the solid surfaces:

$$\rho_s c_{p_s} \frac{\partial T_s}{\partial t} = \frac{\partial}{\partial x} \lambda_{k_s} \frac{\partial T_s}{\partial x} + \dot{q}_s''' \tag{A.41}$$

where ρ_s is the density of the solid, c_{p_s} the specific heat of the solid and λ_{k_s} the thermal conductivity of the solid. The term $\dot{q}_s'''$ is composed of chemical reactions and absorption due to radiation:

$$\dot{q}_s''' = \dot{q}_{s,c}''' + \dot{q}_{s,r}''' \tag{A.42}$$

The term $\dot{q}_{s,c}'''$, corresponds essentially to the production rate (loss) of heat obtained by the pyrolysis model of different types of liquid and solid fuels. The second term, $\dot{q}_{s,r}'''$, corresponds to the sum of the radiations received and emitted by the solid.

The fluid-solid exchanges By default, FDS calculates the convective heat flux, $\dot{q}''_{s,c}$, from the following equation:

$$\dot{q}''_{s,c} = k(T_g - T_w) \tag{A.43}$$

Where T_g is the temperature of the gases outside the boundary layer, T_w the wall temperature (the wall surface of the heat exchange side) and k the heat transfer coefficient.

The aim of the thermal exchanges models is to calculate the value of the heat transfer coefficient k, used in Eq. (A.43). FDS computes this coefficient in three different ways. The first one, implemented by default in FDS, consists in taking the maximum value between the terms of natural convection and forced convection:

$$k = max\left[C|T_g - T_w|^{1/3}, \frac{\lambda_k}{\hat{L}} Nu\right] \tag{A.44}$$

where C is an empirical coefficient for natural convection, $\hat{L}$ is a characteristic length of the solid, λ_k is the thermal conductivity of the gas and Nu is the Nusselt number. The parameter C is equal to 1.52 for horizontal surfaces and 1.31 for vertical or cylindrical surfaces. The Nusselt number depends on the geometry and the characteristics of the flow:

$$\begin{cases} Nu = C_1 + C_2 Re^n Pr^m, & \text{(A.45a)} \\ Re = \dfrac{\rho|\mathbf{u}|L}{\mu}, & \text{(A.45b)} \\ Pr \approx 0.7 & \text{(A.45c)} \end{cases}$$

For plane and cylindrical surfaces, the default values are: $C_1 = 0$, $C_2 = 0.037$, $n = 0.8$, $m = 0.33$ and $L = 1$m. For spherical surfaces, the values are equal to $C_1 = 2$, $C_2 = 0.6$, $n = 0.5$, $m = 0.33$ and $L = D$ where D is the diameter of the sphere. All these constants can be modified by the user.

The second way is to use the log law to model the exchanges close to the walls. This model is defined as:

$$\begin{cases} k = \dfrac{\dot{q}''_w}{T_g - T_w} = \dfrac{\rho_w c_p u_\tau}{T^+}, & \text{(A.46a)} \\ T^+ = \dfrac{T_g - T_w}{T_\tau}, & \text{(A.46b)} \\ T_\tau = \dfrac{\dot{q}''_w}{\rho_w c_p u_\tau} & \text{(A.46c)} \end{cases}$$

In this model, T_g corresponds to the temperature of the gas at the first mesh outside the wall, T_w and ρ_w are the temperature and the density at the wall, $\dot{q}''_w$ is the heat flux at the wall and

T_τ and u_τ are the temperature and velocity scales, respectively. The velocity u_τ is related to the wall slip ($\tau = -\rho u_\tau^2$). This model thus considers that the heat diffuses in an identical way as momentum.

The third and last method consists in imposing the value of the heat transfer coefficient, k, on the basis of values given in tables (see for example Bergman et al. (2011)).

It is also possible to impose directly the value of the heat flux, $\dot{q}''_w$, instead of calculating it by Eq. (A.43). In this case, two different approaches are possible. The first is to define the net heat flux. The code will then calculate the temperature of the surface, so that the sum of the convective and radiative heat fluxes equals the net heat flux. The second method consists in separately specifying the convective heat flux and the radiative heat flux.

FDS can also impose adiabatic conditions on surfaces. In this case, this is equivalent to define a net heat flux equal to 0 and an emissivity of the material equal to 1.

Combustion Combustion is introduced into the governing equations via the source terms, $\dot{q}'''$ in the energy transport equation. For most applications, FDS uses a combustion model based on the mixing-limited, infinitely fast reaction of lumped species. Lumped species are reacting scalar quantities that represent a mixture of species. The reaction of fuel and oxygen is not necessarily instantaneous and complete, and there are several optional schemes that are designed to predict the extent of combustion in under-ventilated spaces. For an infinitely-fast reaction, reactant species in a given grid cell are converted to product species at a rate determined by a characteristic mixing time, τ_{mix}. The heat release rate per unit volume is defined by summing the lumped species mass production rates times their respective heats of formation:

$$\dot{q}''' = -\sum_{\alpha} \dot{m}'''_{\alpha} \Delta h_{f,\alpha} \tag{A.47}$$

The characteristic mixing time, τ_{mix}, dependents on three physical processes: diffusion, subgrid-scale (SGS) advection, and buoyant acceleration. Take the fastest between the three of these processes as its characteristic time scale.

Radiation Radiation is introduced into the governing equations via the source terms, $\dot{q}'''_r$ in the energy transport equation:

$$\dot{q}'''_r = -\nabla \cdot \dot{q}''_r(\mathrm{x}) = \kappa(\mathrm{x})[U(\mathrm{x}) - 4\pi I_b(\mathrm{x})] \quad ; \quad U(\mathrm{x}) = \int_{4\pi} I(\mathrm{x}, s')ds' \tag{A.48}$$

where $\kappa(\mathrm{x})$ is the absorption coefficient, $I_b(\mathrm{x})$ is the source term, and $I(\mathrm{x},s)$ is the solution of the radiation transport equation (RTE) for a non-scattering gray gas:

$$s \cdot \nabla I(\mathrm{x},s) = \kappa(\mathrm{x})[I_b(\mathrm{x}) - I(\mathrm{x},s)] \tag{A.49}$$

The radiation equation is solved using a technique similar to a finite volume method for convective transport. Using about 100 discrete angles, the finite volume solver requires about 20% of the total CPU time of a calculation,

References

Arya, S. and Jr. Lape, J. (1990). A comparative studyof the different criteria for the physical modelling of buoyant plume rise in a neutral atmosphere. *Atmos. Environ.*, 24:289–295.

Atkinson, G. T. and Wu, Y. (1996). Smoke control in sloping tunnels. *Fire Saf. J.*, 27(4):335–341.

Barnett, S. J. (1993). A vertical buoyant jet with high momentum in a long ventilated tunnel. *J. Fluid Mech.*, 252:279–300.

Bergman, T., Lavine, A., Incropera, F., and Dewitt, D. (2011). Introduction to heat transfer. *John Wiley & Sons, 6th Edition*.

Bettis, R., Jagger, S., and Wu, Y. (1993). Interim validation of tunnel fire consequence modes, summary of phase 2 tests. Technical report, HSL Project Report.

Burridge, H., Parker, D., Kruger, E., Partridge, J., and Linden, P. (2017). Conditional sampling of a high Péclet number turbulent plume and the implications for entrainment. *J. Fluid Mech.*, 823:26–56.

Carlotti, P. (2013). Éléments de mécanique des fluides pour la modélisation des incendies. *Habilitation à diriger les recherches, École Centrale de Lyon et Université Claude Bernard Lyon I.*

Chow, W. K., Gao, Y., Zhao, J. H., Dang, J. F., Chow, C. L., and Miao, L. (2015). Smoke movement in tilted tunnel fires with longitudinal ventilation. *Fire Saf. J.*, 75:14–22.

Craske, J., Salizzoni, P., and van Reeuwijk, M. (2017). The turbulent prandtl number in a pure plume is 3/5. *J. Fluid Mech.*, 822:774–790.

Craske, J. and van Reeuwijk, M. (2015). Energy dispersion in turbulent jets. part 1: Direct simulation of steady and unsteady jets. *J. Fluid Mech.*, 763:500–537.

Danziger, N. and Kennedy, W. (1982). Longitudinal ventilation analysis fot the glenwood canyon tunnels. *4th International Symposium Aerodynamics & Ventilation of Vehicule Tunnels*, pages 169–186.

Devenish, B. J., Rooney, G. G., Webster, H. N., and Thomson, D. J. (2010). The entrainment rate for buoyant plumes in a crossflow. *Bound-Lay Meteorol*, 134:411–439.

Ezzamel, A., Salizzoni, P., and Hunt, G. R. (2015). Dynamical variability of axisymmetric buoyant plumes. *J. Fluid Mech.*, 765:576–611.

Grant, G., Jagger, S., , and Lea, C. (1998). Fires in tunnels. *Proc. Roy. Soc. London A*, 356(2873-2906).

Hong, W.-H. (2004). The Progress And Controlling Situation Of Daegu Subway Fire Disaster. *Fire Saf. Sci.*, 6:s–5–1.

Hu, L. H., Tang, W., Chen, L. F., and Yi, L. (2013). A non-dimensional global correlation of maximum gas temperature beneath ceiling with different blockage–fire distance in a longitudinal ventilated tunnel. *Appl. Therm. Eng.*, 56(1):77–82.

Hunt, G. R. and Kaye, N. B. (2005). Lazy plumes. *J. Fluid Mech.*, 533:329–338.

Hunt, J. C. R. (1991). Industrial and environmental fluid mechanics. *Annu. Rev. Fluid Mech.*, 23:1–41.

Hwang, C. C. and Edwards, J. C. (2005). The critical ventilation velocity in tunnel fires-a computer simulation. *Fire Saf. J.*, 40(3):213–244.

Ingason, H., Li, Y. Z., and Lonnermark, A. (2015). *Tunnel Fire Dynamics*. Springer New York, New York, NY.

Jirka, G. H. and Harleman, D. R. F. (1979). Stability and mixing of a vertical plane buoyant jet in confined depth. *J. Fluid Mech.*, 94(02):275–304.

Kaye, N. B. and Hunt, G. R. (2007). Overturning in a filling box. *J. Fluid Mech.*, 576:297–323.

Ko, G., Kim, S., and Ryou, H. (2010). An experimental study on the effect of slope on the critical velocity in tunnel fires. *J Fire Sci.*, 28:27–47.

Le Clanche, J., Salizzoni, P., Creyssels, M., Mehaddi, R., Candelier, F., and Vauquelin, O. (2014). Aerodynamics of buoyant releases within a longitudinally ventilated tunnel. *Exp. Therm Fluid Sci.*, 57:121–127.

Lee, Y.-P. and Tsai, K.-C. (2012). Effect of vehicular blockage on critical ventilation velocity and tunnel fire behavior in longitudinally ventilated tunnels. *Fire Saf. J.*, 53:35–42.

Leitner, A. (2001). The fire catastrophe in the Tauern Tunnel: experience and conclusions for the Austrian guidelines. *Tunnel. Underg. Space Technol.*, 16(3):217–223.

Li, L., Cheng, X., Cui, Y., Li, S., and Zhang, H. (2012). Effect of blockage ratio on critical velocity in tunnel fires. *J Fire Sci.*, 30:413–427.

Li, Y., Shing, V. C. W., and Chen, Z. (2003). Fine bubble modelling of smoke flows. *Fire Saf. J.*, 38(3):285–298.

Li, Y. Z., Lei, B., and Ingason, H. (2010). Study of critical velocity and backlayering length in longitudinally ventilated tunnel fires. *Fire Saf. J.*, 45(6–8):361–370.

Marro, M., Salizzoni, P., Cierco, F., Korsakissok, I., Danzi, E., and Soulhac, L. (2014). Plume rise and spread in buoyant releases from elevated sources in the lower atmosphere. *Environ Fluid Mech.*, 55:50–57.

McGrattan, K., Hostokka, S., McDermott, R., Floyd, J., Weinschenk, C., and Overholt, K. (2008). *Fire Dynamics Simulator (Version 5) User's Guide*. NIST Special Publication 1019 (Fifth Edition).

Megret, O. and Vauquelin, O. (2000). A model to evaluate tunnel fire characteristics. *Fire Saf. J.*, 34:393–401.

Merci, B. (2008). One-dimensional analysis of the global chimney effect in the case of fire in an inclined tunnel. *Fire Saf. J.*, 43(5):376–389.

Michaux, G. and Vauquelin, O. (2008). Solutions for turbulent buoyant plumes rising from circular sources. *Phys. Fluids*, 20:066601.

Morton, B. R., Taylor, G. I., and Turner, J. S. (1956). Turbulent gravitational convection from maintained and instantaneous sources. *Proc. Roy. Soc. London A*, 234:1–23.

Oka, Y. and Atkinson, G. T. (1995). Control of smoke flow in tunnel fires. *Fire Saf. J.*, 25(4):305–322.

Pope, S. (2000). Turbulent flows. *Cambridge University Press*.

Ricou, F. P. and Spalding, D. B. (1961). Measurements of entrainment by axisymmetrical turbulent jets. *J. Fluid Mech.*, 11:21–32.

Rojas Alva, W. U., Jomaas, G., and Dederichs, A. S. (2017). The influence of vehicular obstacles on longitudinal ventilation control in tunnel fires. *Fire Saf. J.*, 87:25–36.

Rooney, G. G. and Linden, P. F. (1996). Similarity considerations for non-boussinesq plumes in an unstratified environment. *J. Fluid Mech.*, 318:237–250.

Salizzoni, P., Creyssels, M., Jiang, L., Mos, A., Mehaddi, R., and Vauquelin, O. (2017). Influence of source conditions and heat losses on the upwind back-layering flow in a longitudinally ventilated tunnel. *Int. J. Heat Mass Transfer. (in press)*.

Tang, W., Hu, L. H., and Chen, L. F. (2013). Effect of blockage-fire distance on buoyancy driven back-layering length and critical velocity in a tunnel: An experimental investigation and global correlations. *Appl. Therm. Eng.*, 60(1–2):7–14.

Thomas, P. H. (1968). *The movement of smoke in horizontal passages against an air flow*. Fire Research Note, No. 723, Fire Research Station, Watford, UK.

Van Den Bremer, T. S. and Hunt, G. R. (2010). Universal solutions for Boussinesq and non-Boussinesq plumes. *J. Fluid Mech.*, 644:165–192.

van den Bremer, T. S. and Hunt, G. R. (2014). Two-dimensional planar plumes and fountains. *J. Fluid Mech.*, 750:210–244.

Van Maele, K. and Merci, B. (2008). Application of RANS and LES field simulations to predict the critical ventilation velocity in longitudinally ventilated horizontal tunnels. *Fire Saf. J.*, 43(8):598–609.

van Reeuwijk, M., Salizzoni, P., Hunt, G., and Craske, J. (2016). Turbulent transport and entrainment in jets and plumes: A dns study. *Phys. Rev. Fluids*, 1:074301.

Vauquelin, O. (2005). Parametrical study of the back flow occurrence in case of a buoyant release into a rectangular channel. *Exp. Therm Fluid Sci.*, 29(6):725–731.

Vauquelin, O. (2008). Experimental simulations of fire-induced smoke control in tunnels using an 'air-helium reduced scale model': Principle, limitations, results and future. *Tunnel. Underg. Space Technol.*, 23:171–178.

Vreman, A. W. (2004). An eddy-viscosity subgrid-scale model for turbulent shear flow: Algebraic theory and applications. *Phys. Fluids*, 16(10):3670–3681.

Vuilleumier, F., Weatherill, A., and Crausaz, B. (2002). Safety aspects of railway and road tunnel: example of the Lötschberg railway tunnel and Mont-Blanc road tunnel. *Tunnel. Underg. Space Technol.*, 17(2):153–158.

Weng, M. C., Lu, X. L., Liu, F., and Du, C. X. (2016). Study on the critical velocity in a sloping tunnel fire under longitudinal ventilation. *Appl. Therm. Eng.*, 94:422–434.

Weng, M. C., Lu, X. L., Liu, F., Shi, X. P., and Yu, L. X. (2015). Prediction of backlayering length and critical velocity in metro tunnel fires. *Tunnel. Underg. Space Technol.*, 47:64–72.

Wu, Y. and Bakar, M. Z. A. (2000). Control of smoke flow in tunnel fires using longitudinal ventilation systems - a study of the critical velocity. *Fire Saf. J.*, 35(4):363–390.

Yi, L., Xu, Q. Q., Xu, Z. S., and Wu, D. X. (2014). An experimental study on critical velocity in sloping tunnel with longitudinal ventilation under fire. *Tunnel. Underg. Space Technol.*, 43:198–203.

Zhang, S., Cheng, X., Yao, Y., Zhu, K., Li, K., Lu, S., Zhang, R., and Zhang, H. (2016). An experimental investigation on blockage effect of metro train on the smoke back-layering in subway tunnel fires. *Appl. Therm. Eng.*, 99:214–223.